NOTE TO USERS

DISSERTATION

STUDIES OF THE POLARIMETRIC COVARIANCE MATRIX FOR METEOROLOGICAL APPLICATIONS

Submitted by

Yanting Wang

Department of Electrical and Computer Engineering

In partial fulfillment of the requirements

for the Degree of Doctor of Philosophy

Colorado State University

Fort Collins, Colorado

Fall 2004

COLORADO STATE UNIVERSITY

November 4, 2004

WE HEREBY RECOMMEND THAT THE DISSERTATION PREPARED UNDER OUR SUPERVISION BY YANTING WANG ENTITLED STUDIES OF THE POLARIMETRIC COVARIANCE MATRIX FOR METEOROLOGICAL APPLICATIONS BE ACCEPTED AS FULFILLING IN PART REQUIREMENTS FOR THE DEGREE OF DOCTOR OF PHILOSOPHY.

Committee on Graduate Work

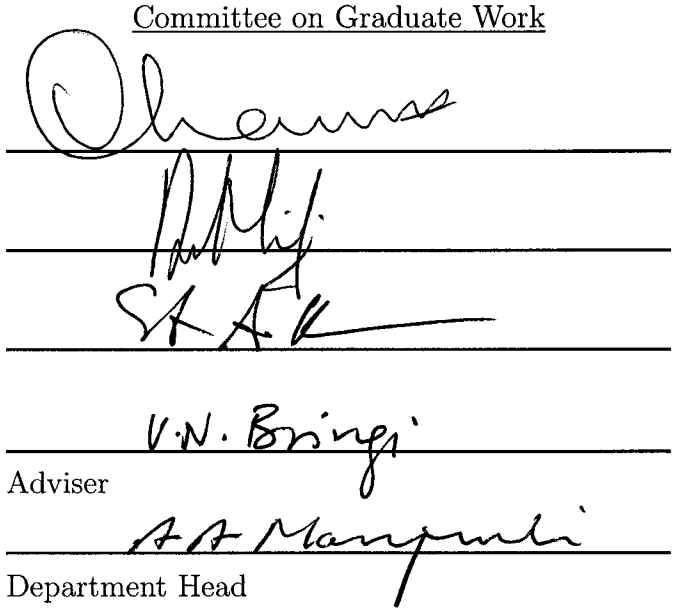

Adviser

Department Head

ABSTRACT OF DISSERTATION

STUDIES OF THE POLARIMETRIC COVARIANCE MATRIX FOR METEOROLOGICAL APPLICATIONS

Multi-parameter polarimetric radar has shown great utility in meteorology by improving measurement accuracy and microphysical understanding. This work concentrates on studies of the full polarimetric covariance matrix to retrieve the moment estimations over the shape distribution and orientation distribution of the precipitation medium.

The antenna-induced polarimetric errors that result from inter-channel contamination and sidelobe leakage are first examined. Antenna patterns are used to convolve the distributed medium with large gradients and a methodology to detect such polarimetric errors is developed. The methodology is illustrated with volume simulation of a synthetic storm and then is applied to real cases from the project of Thunderstorm Electrification and Precipitation Study (STEPS). The detection is evaluated by comparing the results between two coordinated research radars – CSU-CHILL and NCAR S-Pol. The evaluation of antenna peformance is also given within this context.

In the second part, the full polarimetric covariance matrix is studied along with polarization basis transformation. The effect of backscattering canting, the effect of propagation, and the integrated antenna polarization errors on the covariance matrix are analyzed. Considering backscattering canting, a new method to

estimate the orientation factors, i.e., the mean canting angle and its dispersion, is proposed based directly on the covariance matrix in the linear basis. The new method is compared with other approaches, such as that based on circular covariance matrix and that based on polarization optimization. The distortion due to propagation, especially due to non-diagonal propagation, is studied with simulation. Concerning the integrated antenna polarization errors, a novel approach is proposed to estimate the non-orthogonal error matrix.

In the last part, the proposed approaches are applied to a variety of real cases. For the purpose of orientation estimation, the full covariance matrix must be calibrated carefully on both power terms and phase terms. A modified phase filtering process is designed to obtain robust filtering over the "weak" cross-polar channels so that the phase offsets could be accurately estimated. The integrated antenna polarization errors are then estimated and corrected. Different types of precipitation are analyzed with the estimated orientation factors, the derived circular radar variables, and the conventional linear radar variables. It is shown that the linear depolarization ratio suffers ambiguity on presenting orientation information compared to the estimated orientation dispersion. The mean canting angle is very close to zero for most precipitation targets except the aligned crystals which can be usually observed at the top of electrified storms. The near zero mean canting angle also justifies the hybrid operation mode planned for the WSR-88D radars.

Yanting Wang
Department of Electrical and Computer Engineering
Colorado State University
Fort Collins, Colorado 80523
Fall 2004

ACKNOWLEDGEMENTS

I am obligated to thank all the people who made this work possible upon the completion of this dissertation.

I would like to express my profound gratitude to my adviser Dr. V.N. Bringi for his inspiring guidance, unceasing encouragement and support throughout the course of my graduate studies. I am also deeply grateful to Dr. V. Chandrasekar for the rewarding discussion with him over a wide range of research topics and his invaluable advice. I also want to express my sincere thanks to Dr. Steven A. Rutledge and Dr. Derek L. Lile for their time and effort to review and comment on this dissertation.

I highly appreciate the beneficial discussion with Dr. Gwo-Jong Huang, Dr. Wan-yu Li and Gang Xu, the help from Dr. John Hubbert, and all kinds of assistant from other fellows working in the Radar and Communication Lab at Colorado State University.

Special appreciation also goes to the CSU-CHILL radar staff: David Brunkow and Patrick Kennedy, for their timely help and arrangement on the radar data that are used in this work.

Last but not least, I am always deeply grateful to my wife Kaitlyn and my family for their understanding and encouragement.

This research was supported by the National Science Foundation.

DEDICATION

To my parents: Baocheng and Meitang.

TABLE OF CONTENTS

LIST OF FIGURES

LIST OF TABLES

Chapter 1

INTRODUCTION

1.1 Review of Polarimetric Radar Meteorology

Since the use of radar was found to detect storms in early 1940's, radar meteorology has been developed as an active field in atmospheric study [1], [2]. Radar provides a powerful tool for meteorologists with its capability of high resolution scan in both time and space. The power of radar echoes is used to determine the intensity of precipitation; and the Doppler frequency shift can be used to estimate the motion of hydrometeor particles.

Such two parameters are not sufficient to describe the precipitation characteristics since hydrometeor target by itself is a three dimensional non-spherical particle. Polarimetric radar takes advantage of a pair of independent polarization states, which define a polarization plane, to obtain the projected signatures of the precipitation targets on the polarization plane [3], [4]. As a result, multiple parameters about the remote targets are available, such as those related to particle shape [5] and orientation [6].

Dual-polarization radar usually works on a pair of orthogonal polarization states, e.g., linear horizontal/vertical (H/V) polarization, right-hand/left-hand circular (RHC/LHC) polarization, or more generally a pair of orthogonal elliptical polarization. On transmission, the dual-polarization radar could alternately change the polarization state pulse by pulse between this orthogonal pair. On reception, it

should be able to measure the echoes in both polarization states. The precipitation media, as random scatters, can be described by its shape distribution, orientation distribution as well as its size distribution (DSD). Under the alternate transmission mode, a 3×3 full covariance matrix can be constructed which carries the moments of those distributions [7], [8]. It is of great interest to retrieve the related physical parameters from the covariance matrix.

The hydrometeor particles have been shown to possess equilibrium shape with "mirror" reflection symmetry [9], [10]. Also it is usually true at least for rain that the symmetry axis aligns nearly vertical during falling. Therefore, the reflectivities in co-polar channels provide a credible measure of the drop size, and the differential reflectivity gives an estimation of the degree of oblateness. This kind of measurement and retrieval has been well studied partly because only "strong" co-polar returns are required.

However the hydrometeor particles may also undergo oscillations and non-zero canting [11] [12] [13], which would bias more or less the measurement. Therefore, the knowledge on the corresponding orientation distribution would be useful to fine tune for quantitative applications such as rainfall estimation and also possibly to improve the classification by providing more insight into the microphysical characteristics. The orientation distribution affects more dramatically the cross-polar power and the co-to-cross correlation coefficients [14]. The retrieval of orientation factors, such as the mean canting angle and canting dispersion, requires measurement of the "weak" cross-polar signals [15]. It is only recently that the full covariance matrix has been utilized where the cross-polar terms play a role as important as the co-polar terms.

Polarimetric measurements demand accurate knowledge of the polarization states. However, some factors will distort the polarization states throughout the

transmission/reception chains. One of the primary factors is the antenna performance. The antenna subsystem can only provide limited cross-polarization isolation that is vital to accurately measure the "weak" cross-polar signals. Moreover, because of the distributed nature of hydrometeor targets, the non-diminishing sidelobes of antenna patterns can lead to large contamination from nearby strong storm cells when larger gradients in reflectivity exist across the antenna beam. Some other physical factors, such as propagation distortion, may also change the polarization state of radar echoes and as a result will mislead the physical retrieval and interpretation. Such artifacts must be detected and sorted out or corrected.

1.2 Polarimetric Model for Linear Dual-polarization Radar

This study is based on data from Colorado State University-University of Chicago-Illinois State Water Survey (CSU-CHILL) dual-polarization radar. The CSU-CHILL radar works on the linear H/V polarization basis and is able to measure the full covariance matrix in alternate mode [16]. In the linear H/V basis, the incident electromagnetic field $\mathbf{E}_i$ and the corresponding backscattering electromagnetic field $\mathbf{E}_s$ can be written as,

$$\mathbf{E^i} = E_h^i \hat{h} + E_v^i \hat{v} \quad . \tag{1.1a}$$

$$\mathbf{E^s} = E_h^s \hat{h} + E_v^i \hat{v} \tag{1.1b}$$

These two fields are related to each other in backscattering system alignment (BSA) through the Sinclair matrix [17] as,

$$\begin{bmatrix} E_h^s \\ E_v^s \end{bmatrix} = \begin{bmatrix} S_{hh} & S_{hv} \\ S_{vh} & S_{vv} \end{bmatrix} \begin{bmatrix} E_h^i \\ E_v^i \end{bmatrix} \tag{1.2}$$

The 2-by-2 Sinclair matrix, which depicts the scattering properties of targets, is called backscattering matrix ($\mathbf{S}$) hereafter.

By reciprocity, $S_{hv} = S_{vh}$; therefore a "feature" vector [7]

$$\Omega = \left[\begin{array}{ccc} S_{hh} & \sqrt{2}S_{hv} & S_{vv} \end{array} \right] \tag{1.3}$$

can be defined to characterize the scattering matrix without losing any information. To study the randomly distributed medium, we can employ the second order moments of the "feature" vector Ω and obtain the covariance matrix,

$$\Sigma = \left[\begin{array}{ccc} \langle |S_{hh}|^2 \rangle & \sqrt{2}\langle S_{hh}S_{hv}^* \rangle & \langle S_{hh}S_{vv}^* \rangle \\ \sqrt{2}\langle S_{hh}^* S_{hv} \rangle & 2\langle |S_{hv}|^2 \rangle & \sqrt{2}\langle S_{vv}^* S_{hv} \rangle \\ \langle S_{hh}^* S_{vv} \rangle & \sqrt{2}\langle S_{hh}^* S_{hv} \rangle & \langle |S_{vv}|^2 \rangle \end{array} \right] \tag{1.4}$$

If a radar is able to transmit a pair of electric fields with independent polarization states, the whole backscattering matrix can be determined and the full covariance matrix can be constructed. The CSU-CHILL radar operates in the "full polarimetric" mode by alternately transmitting H-polarized and V-polarized fields.

The covariance matrix contains three independent real variables along its diagonal corresponding to powers and three independent complex variables off diagonal corresponding to correlations. The radar variables in the linear H/V basis are defined on this covariance matrix as following [18]:

(1) Radar reflectivity factor:

$$Z_h = 10 \log_{10} \langle |S_{hh}|^2 \rangle \tag{1.5}$$

(2) Radar differential reflectivity factor:

$$Z_{DR} = 10 \log_{10} \frac{\langle |S_{hh}|^2 \rangle}{\langle |S_{vv}|^2 \rangle} \tag{1.6}$$

(3) Linear depolarization ratio:

$$LDR_{vh} = 10 \log_{10} \frac{\langle |S_{hv}|^2 \rangle}{\langle |S_{hh}|^2 \rangle} \tag{1.7}$$

(4) Co-polar correlation coefficient:

$$\rho_{co} e^{j\delta_{co}} = \frac{\langle S_{hh}S_{vv}^* \rangle}{\sqrt{\langle |S_{hh}|^2 \rangle \langle |S_{vv}|^2 \rangle}} \tag{1.8}$$

(5) Co-to-cross correlation coefficients:

$$\rho_{xh} = \frac{|\langle S_{hh} S_{hv}^* \rangle|}{\sqrt{\langle |S_{hh}|^2 \rangle \langle |S_{hv}|^2 \rangle}} \tag{1.9a}$$

$$\rho_{xv} = \frac{|\langle S_{vv} S_{hv}^* \rangle|}{\sqrt{\langle |S_{vv}|^2 \rangle \langle |S_{hv}|^2 \rangle}} \tag{1.9b}$$

The radar reflectivity factor and depolarization ration in V polarization, Z_v and LDR_{hv}, can be simply derived from the variables above.

The waves may undergo propagation distortion through the precipitation medium between the antenna and the resolution volume. The propagation effects can also result in change of polarization states, which is denoted by the propagation matrix

$$\mathbf{P} = \begin{bmatrix} P_{hh} & P_{hv} \\ P_{vh} & P_{vv} \end{bmatrix} \tag{1.10}$$

When the waves propagate in eigen-polarization, the propagation matrix is diagonal and the only distortion in such case includes attenuation in the power terms and phase shift in the correlations. The attenuation is generally negligible in S-band while the phase shift could be significant along a long propagation path. As a result, we have another radar variable defined as,

(6) Differential propagation phase shift (two-way):

$$\Phi_{dp} = \arg \langle P_{hh}^{2*} P_{vv}^2 \rangle \tag{1.11}$$

In operation, the antenna along with its polarization network will, to a small extent, change the polarization states both at transmission and reception since, in practice, the polarization isolation can never be perfect. We can incorporate these effects into the gain matrix,

$$\mathbf{G} = \begin{bmatrix} g_h & e_v \\ e_h & g_v \end{bmatrix} \tag{1.12}$$

where components e_h and e_v represent the cross polarization contamination.

Therefore, the radar measured voltage matrix is governed by such a system (with the spherical wave factor dropped):

$$\begin{bmatrix} V_{hh} & V_{hv} \\ V_{vh} & V_{vv} \end{bmatrix} = (\mathbf{G^T P^T S P G}) \cdot \mathbf{C} + \mathbf{N} \tag{1.13}$$

where $\mathbf{C}$ stands for the calibration matrix and $\mathbf{N}$ represents additive noise. The radar variables are derived from the covariance matrix of the above voltage matrix. To restore the intrinsic covariance matrix, we need to correct for noise, calibrate the measurements, and correct the linear transformation incurred by antenna polarization errors and propagation.

1.3 Objectives

This work will explore the full covariance matrix under the linear H/V polarization basis for microphysical retrieval. In particular, effort will be directed to analyze the antenna-induced polarimetric errors when strong reflectivity gradients exist across beam, and to retrieve the moment estimation over orientation distribution.

Before using the full covariance matrix, the radar measurement should first be properly calibrated. However, it is impossible to correct the data under the scenario of inhomogeneous medium where spatial convolution governs the remote sensing process. The abnormal data in this case is mainly attributed to the sidelobes in antenna patterns. Methods to detect the error-prone locations will be developed in next chapter. A model of polarimetric radar measurement will be created for distributed precipitation targets. Based on that, a simulation approach will be implemented and detection methodology will be proposed for errors in Z_{DR}, K_{dp} and LDR. The proposed methodology will be applied to radar data from the Severe Thunderstorm Electrification and Precipitation Study (STEPS) project, where two research radars (CSU-CHILL and NCAR S-Pol) were deployed at different locations and coordinated in scanning, for validation.

Assuming the "intrinsic" covariance matrix known, this study will be directed to retrieve the orientation factors, including both mean and dispersion of canting angle. A general representation will be formulated for basis transformation of the covariance matrix. The covariance matrix constructed in linear polarization basis can be transformed to arbitrary orthogonal bases via unitary transformation. Therefore, the covariance matrix in circular polarization basis can be simply obtained using basis transformation where the orientation factors and shape factors are separable. An algorithm to estimate the orientation factors will then be derived by directly solving the covariance matrix in the linear basis. Both methods will be compared to the method involving polarization optimization.

The effect of propagation and antenna polarization errors then will be analyzed. Simulations will be conducted to show their impact on the covariance elements especially on the cross-polar terms in order to find guidelines for discriminating such factors. Non-orthogonal propagation and antenna polarization errors will distort the radiated polarization state to general elliptical polarization instead of the ideal linear polarization and the resultant polarization basis is no longer orthogonal. A novel optimization approach is developed for such nonorthogonal basis transformation so that the integrated antenna polarization error matrix can be estimated.

Finally, the developed algorithms will be applied to case studies. From the accurately constructed covariance matrix, the antenna polarization errors will be estimated and then corrected for; a commonly used approach will be applied to correct the propagation effect; and lastly the "intrinsic" backscattering covariance matrix is obtained and orientation factors along with shape factors are estimated. The use of these retrieved parameters will also be studied by analyzing radar data from different types of precipitation.

Chapter 2

ANTENNA INDUCED POLARIMETRIC ERRORS

It is well known that the antenna performance is of prime importance in radar remote sensing. Ideally, accurate dual polarization measurement requires well-matched co-polar patterns, low sidelobe level and small cross-polar contamination.

For point targets, the ideal antenna can be expressed by the 2×2 identity matrix. In practice, the gain imbalance between two orthogonal channels and the limited polarization isolation will distort measurement of the intrinsic scattering matrix. Such errors can be adjusted for by the calibration procedure. Considering distributed targets, however, the antenna patterns are also required to have narrow beam shape. In general, the intrinsic scattering matrix is convolved with the antenna patterns, resulting in spatial errors on radar measurements.

For the CSU-CHILL radar, the co-polar patterns are fairly narrow (3dB-beamwidth around 1^o) and the sidelobe level is at -30 dB or better. Besides, the cross-polar coupling is maintained as low as -35 dB. This performance seems to be sufficient for measurement in homogeneous precipitation. However, large gradients of reflectivity (e.g. > 40 dB/km) often exist in severe storms, and the antenna-induced polarimetric errors may become significant. Therefore, such spatial distortion is also called "gradient induced" polarimetric errors.

When gradients are fairly small, the point target calibration technique is also justified for distributed targets [19]. Otherwise, the beam-filling effect should be

taken into account. Previous work has been done on analyzing the beam-filling effect on Z_h, Z_{DR} and K_{dp} [20], [21], [22]. In this chapter, a systematic procedure is developed for detecting antenna-induced polarimetric errors in the presence of sharp gradients of precipitation echoes. Synthetic storm simulation is used to illustrate the methodology to mask error-prone regions in the Z_{DR}, LDR and K_{dp} fields. Data from a severe storm event from both the CSU-CHILL radar and NCAR S-Pol radar are used to demonstrate and validate the methodology.

2.1 System function of dual-polarized radar

To study the polarimetric errors induced by antenna patterns $\mathbf{G}$, the precipitation related part $\mathbf{P^T SP}$ of (1.13) will be regarded as the "intrinsic scattering" matrix. The angular dependency should be addressed in such a way that the voltage presented at the radar receiver is written as a convolution:

$$\mathbf{V}(\theta,\phi,r) = \iint \mathbf{G}^T(\theta'-\theta,\phi'-\phi)\mathbf{S}(\theta',\phi',r)\mathbf{G}(\theta'-\theta,\phi'-\phi)d\Omega' \tag{2.1}$$

where θ and ϕ denote the off-axis angles in elevation and azimuth respectively, and the integration is over a solid angle on the spherical surface whose radius is the range r. This is the system equation for dual-polarization weather radar.

More insight will be gained using the concept of feature vector by expanding (2.1) as follows,

$$V_{hh} = g_h^2 * S_{hh} + 2g_he_h * S_{vh} + e_h^2 * S_{vv} \tag{2.2a}$$

$$V_{vh} = g_he_v * S_{hh} + (g_hg_v + e_he_v) * S_{vh} + g_ve_h * S_{vv} \tag{2.2b}$$

$$V_{vv} = g_v^2 * S_{vv} + 2g_ve_v * S_{vh} + e_v^2 * S_{hh} \tag{2.2c}$$

where angles θ and ϕ are implicit. The system equation would be clearer in the frequency domain:

$$(\mathcal{F}\vec{\Omega}_V)(f_1,f_2) = (\mathcal{F}\tilde{\mathbf{G}})(f_1,f_2)\cdot(\mathcal{F}\vec{\Omega}_S)(f_1,f_2) \tag{2.3}$$

where $\mathcal{F}$ is the Fourier operator and

$$\tilde{\mathbf{G}} = \begin{bmatrix} g_h^2 & \sqrt{2}g_h e_h & e_h^2 \\ \sqrt{2}g_h e_v & g_h g_v + e_h e_v & \sqrt{2}g_v e_h \\ e_v^2 & \sqrt{2}g_v e_v & g_v^2 \end{bmatrix} \tag{2.4}$$

The statistics to construct the covariance matrix is taken over time dimension. To study the property of covariance matrix contaminated with antenna errors, we simply assume a pair of generalized variables

$$V_1 = h_1 * S_1 \tag{2.5a}$$

$$V_2 = h_2 * S_2 \tag{2.5b}$$

Then the second order statistics can be written as

$$\begin{aligned} \langle V_1 V_2^* \rangle(\mathbf{x}) &= \langle \iint h_1(\mathbf{x} - \mathbf{x_1'}) S_1(\mathbf{x_1'}) d\mathbf{x_1'} \cdot \iint h_2^*(\mathbf{x} - \mathbf{x_2'}) S_2^*(\mathbf{x_2'}) d\mathbf{x_2'} \rangle \\ &= \iiiint h_1(\mathbf{x} - \mathbf{x_1'}) h_2^*(\mathbf{x} - \mathbf{x_2'}) \langle S_1(\mathbf{x_1'}) S_2^*(\mathbf{x_2'}) \rangle d\mathbf{x_1'} d\mathbf{x_2'} \end{aligned} \tag{2.6}$$

Because the resolution volume contains numerous scatterers with random phase, the incoherent summation is just zero if $\mathbf{x_1'} \neq \mathbf{x_2'}$. Hence,

$$\langle V_1 V_2^* \rangle(\mathbf{x}) = \iint h_1 h_2^*(\mathbf{x} - \mathbf{x_1'}) \langle S_1 S_2^* \rangle(\mathbf{x_1'}) d\mathbf{x_1'} \tag{2.7}$$

Applying this property to the covariance matrix, we have

$$(\mathcal{F}\vec{\Sigma}_V)(f_1, f_2) = (\mathcal{F}(\tilde{\mathbf{G}} \otimes \tilde{\mathbf{G}}^H))(f_1, f_2)(\mathcal{F}\vec{\Sigma}_S)(f_1, f_2) \tag{2.8}$$

where the Kronecker product is used.

Therefore, in absence of noise, the "intrinsic" backscatter matrix can be recovered if the antenna patterns are known precisely. However, in practice such inversion is not possible due to the existence of noise, the scanning process, and the low spatial sampling. Then it is of much importance to study the impact of antenna patterns on the measurement for the purpose of error detection.

2.2 Antenna Patterns and Antenna Induced Polarimetric Errors

Fig.2.1 shows the antenna patterns of CSU-CHILL in selected planes (azimuth plane and slant 45^o plane) measured at the manufacturer's test range. In the azimuth plane, the cross-polar patterns are much lower than the co-polar patterns. In the slant 45^o plane, the peaks of cross-polar patterns are raised by up to 15 dB compared to the azimuth plane but are displaced away from foresight. Such difference between the two planes is attributed to the structure of feed support struts on slant 45^o and 135^o planes. The close-in co-polar sidelobes also experience a significant increase on the 45^o plane. Overall the cross-polar magnitudes are much lower than the co-polar ones. Another important point is that the co-polar patterns are well-matched with each other only within the mainlobe.

It is straightforward to derive all the elements of the covariance matrix as a function of antenna patterns by either taking second order moments over (2.2) or computing the Kronecker product in (2.4), but the results are complex with many minor terms. To clarify the connection between antenna patterns and polarimetric errors, only the primary factors will be discussed here. We assume that:

(1) the antenna is well designed, which means $e_h \ll g_h$ and $e_v \ll g_v$;

(2) the scattering medium exhibits "mirror" reflection symmetry with zero mean canting angle, which implies $\langle S_{hh}S_{vh}^* \rangle = \langle S_{vv}S_{vh}^* \rangle = 0$;

(3) low depolarization, i.e., $\langle |S_{vh}|^2 \rangle \ll \langle |S_{hh}|^2 \rangle$, $\langle |S_{hv}|^2 \rangle \ll \langle |S_{vv}|^2 \rangle$.

Then by approximating to the first order of polarization errors for the co-polar measurement and to the third order for the cross-polar measurement, the covari-

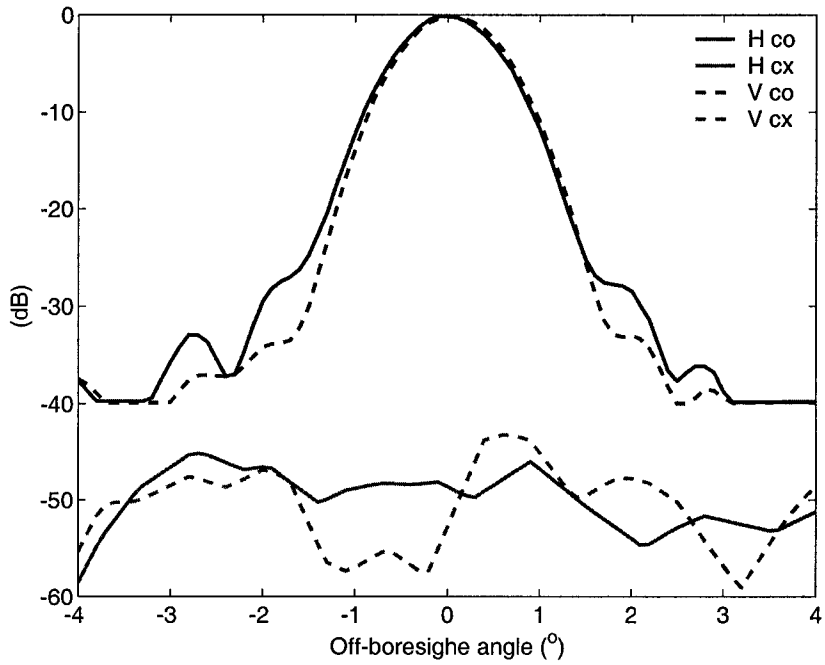

(a) Azimuth Plane

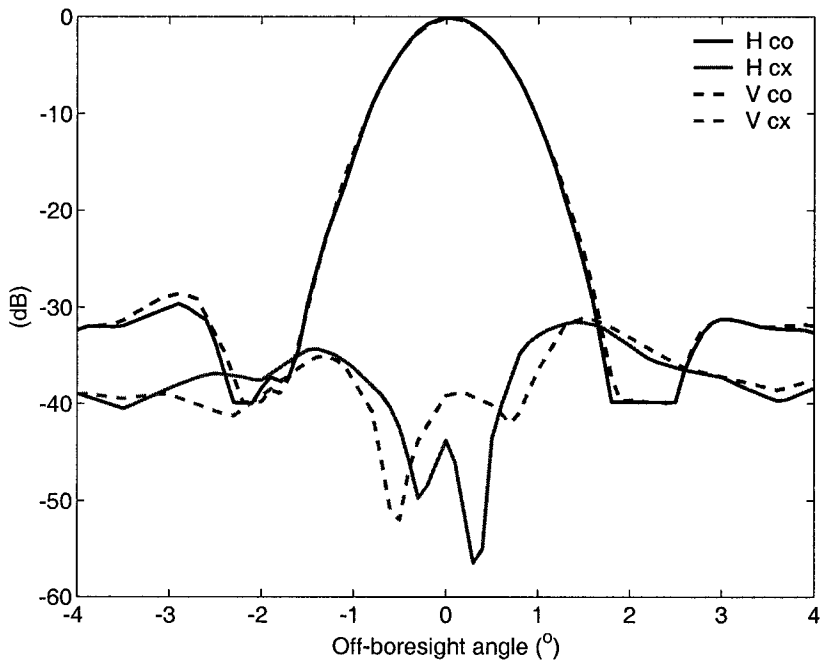

(b) Slant 45° Plane

Figure 2.1: The antenna patterns of the CSU-CHILL radar in selected planes

ance variables can be simplified as follows,

$$\langle |V_{hh}|^2 \rangle = |g_h|^4 * \langle |S_{hh}|^2 \rangle \tag{2.9}$$

$$\langle |V_{vv}|^2 \rangle = |g_v|^4 * \langle |S_{vv}|^2 \rangle \tag{2.10}$$

$$\langle |V_{vh}|^2 \rangle = |g_h e_v|^2 * \langle |S_{hh}|^2 \rangle + |g_v e_h|^2 * \langle |S_{vv}|^2 \rangle + 2\Re\{g_h g_v^* e_h^* e_v * \langle S_{hh} S_{vv}^* \rangle\}$$
$$+ |g_h g_v|^2 * \langle |S_{vh}|^2 \rangle + 2\Re\{g_h g_v e_h^* e_v^* * \langle |S_{vh}|^2 \rangle\} \tag{2.11}$$

$$\langle V_{hh} V_{vv}^* \rangle = g_h^2 g_v^{*2} * \langle S_{hh} S_{vv}^* \rangle \tag{2.12}$$

For reflectivity factors Z_h and Z_v, their intrinsic profiles will be smoothed and broadened due to the finite width of the antenna patterns [23]. The measurement is not very contaminated unless the antenna points to very low reflectivity region and the sidelobes fall into nearby high reflectivity regions. The co-polar patterns have excellent fall-off feature with angle and we can deduce that the reflectivity factors Z_h and Z_v would be close to their intrinsic values.

However, the mismatch in co-polar patterns should be taken into account for evaluating Z_{DR} [24] [25], which can be expressed in linear scale as

$$z_{dr} = \frac{\iint |g_h|^4 \langle |S_{hh}|^2 \rangle d\Omega'}{\iint |g_v|^4 \langle |S_{vv}|^2 \rangle d\Omega'} \tag{2.13}$$

The value of z_{dr} may get biased by two factors: mismatch between co-polar patterns and beam-smoothing, especially by sidelobes. Usually the co-polar patterns are matched very well in the mainlobe except for a constant gain inequality between H and V ports, but apparent mismatch will very likely exist in the sidelobes. Therefore, once the sidelobes are pointed at high reflectivity regions, the polarimetric error on Z_{DR} may go up to a noticeable level.

Large Φ_{dp} may be accumulated along the propagation path. If sharp gradients in Φ_{dp} exist, the estimation of Φ_{dp} will also get biased due to beam-smoothing, and the correlation coefficient

$$\rho_{co} = \frac{|\iint g_h^2 g_v^{*2} \langle S_{hh} S_{vv}^* \rangle d\Omega'|}{\sqrt{\iint |g_h|^4 \langle |S_{hh}|^2 \rangle d\Omega' \cdot \iint |g_v|^4 \langle |S_{vv}|^2 \rangle d\Omega'}} \tag{2.14}$$

will drop below its intrinsic value due to the reduced coherency. Especially, the antenna patterns have uniform distributed random phase errors in sidelobe regions, so ρ_{co} will get much lowered when the power returned from sidelobe regions dominates, which again means that large reflectivity gradients across the beam will result in apparent errors. Correspondingly, K_{dp} will exhibit pairwise positive and negative biases, as shown in [22].

The antenna cross-polar coupling would lead to contamination of the cross-polar power and, as a result, bias LDR. In the mainlobe, excellent polarization isolation is maintained as shown in Fig.2.1. However, in the sidelobes, the polarization isolation deteriorates dramatically such that the cross-polar coupling terms as shown in the top line of (2.11) will contribute to most of the cross-polar power. Therefore, instead of the beam-smoothing effect as shown in the bottom line of (2.11), we will primarily study the bias of LDR that is defined as:

$$\Delta l_{dr} = \frac{\iint |g_h e_v|^2 \langle |S_{hh}|^2 \rangle d\Omega' + \iint |g_v e_h|^2 \langle |S_{vv}|^2 \rangle d\Omega' + 2\Re \iint g_h g_v^* e_h^* e_v \langle S_{hh} S_{vv}^* \rangle d\Omega'}{\iint |g_h|^4 \langle |S_{hh}|^2 \rangle d\Omega'} \tag{2.15}$$

This bias could be applied to adjust the measured LDR. When the medium is homogeneous, this bias would be close to the system limit of LDR.

2.3 Simulation and Detection Methodology

When strong reflectivity gradients occur across the beam, we believe that some radar observables are prone to polarimetric errors. It is of much interest to detect the error-prone locations and find the magnitude of such errors. As analyzed in the previous section, the induced errors result from the convolution between the antenna patterns and the non-uniform reflectivity field, therefore the gradient in precipitation echo itself is not sufficient to locate the errors. A forward convolution is, thus, needed to study the error structures.

The convolution is taken over the spherical surface with the range as radius. Within small off-axis angles, for example only 4 degrees in this study, such spherical convolution can be approximated by a 2-D convolution on the plane (θ, ϕ). To implement such 2-D convolution, 2-D raster antenna patterns are necessary. For the CSU-CHILL radar, only on-axis patterns are available on the four test planes, so we need to construct its 2-D antenna patterns by interpolation. In angular domain the interpolation is implemented by Fourier Transform to get 0.1^o spaced ϕ-patterns. Then the patterns are interpolated into full regular grid on (θ_i, ϕ_j), as shown in Fig.2.2.

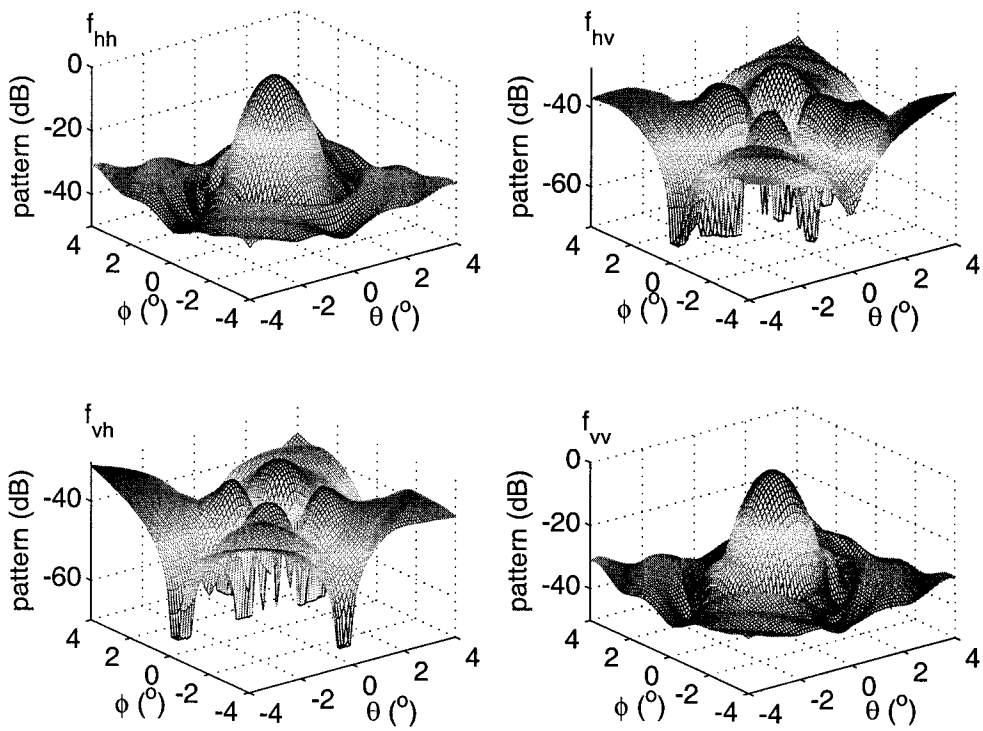

Figure 2.2: The interpolated antenna patterns for the CSU-CHILL radar

We do not have exact knowledge about the "intrinsic" profiles of the polarimetric varaibles. As in [25], the measurement is first taken as "intrinsic", which means double convolution with same patterns imposed on the targets. We hypothesize that the double convolution is sufficient to derive the error structure since

the co-polar antenna patterns are Gaussian shaped with narrow widths such that the co-polar measurement would undergo only small extra biases by double convolution. Therefore, it is appropriate to assume that the measured reflectivity is approximately equal to its intrinsic value. As for the cross-polar measurement, we can find that the dominant errors also come from gradients in Z_{hh} and Z_{vv} when the intrinsic LDR is small (and in which case we are actually interested in the cross-polar errors).

The phase patterns are also required for the detection of error structures of Φ_{dp} and ρ_{co} as indicated by (2.14). Note that it is difficult to measure the phase patterns [26]. Therefore, uniformly distributed random phase is introduced beyond the mainlobe in preparing the co-polar antenna patterns.

To illustrate the polarization errors induced by the antenna, a synthetic storm cell is simulated with simple spherical symmetric structure. The synthetic storm core is assumed to be located at 80 km east and 30 km north of the CSU-CHILL radar and 5 km in altitude. One cut through the synthetic storm core is shown in Fig.2.3.

Previous work on the polarimetric error of Z_{DR} separates the co-polar antenna patterns to well-matched part and mismatched part [25]. When the mismatch is fairly low, good approximation was obtained as

$$\Delta Z_{DR} = 10 \log \left[1 + \frac{C_h}{\bar{Z}_h} \iint (f_h^2 - f_v^2) \bar{Z}_h d\Omega' \right] \tag{2.16}$$

by assuming measured Z_h as its intrinsic value and $Z_h = Z_v$. However, considering inhomogeneous Z_{DR}, the antenna patterns in sidelobes cannot be neglected. We use ρ_{co} as a bridge to analyze Z_{DR} error caused by sidelobes. Because of random phase present in the sidelobes, ρ_{co} after convolution will drop significantly when the sidelobes fall into high reflectivity regions. Therefore, the decrease of ρ_{co} can be used as an indicator for such Z_{DR} error. Regarding use of ρ_{co}, we assume

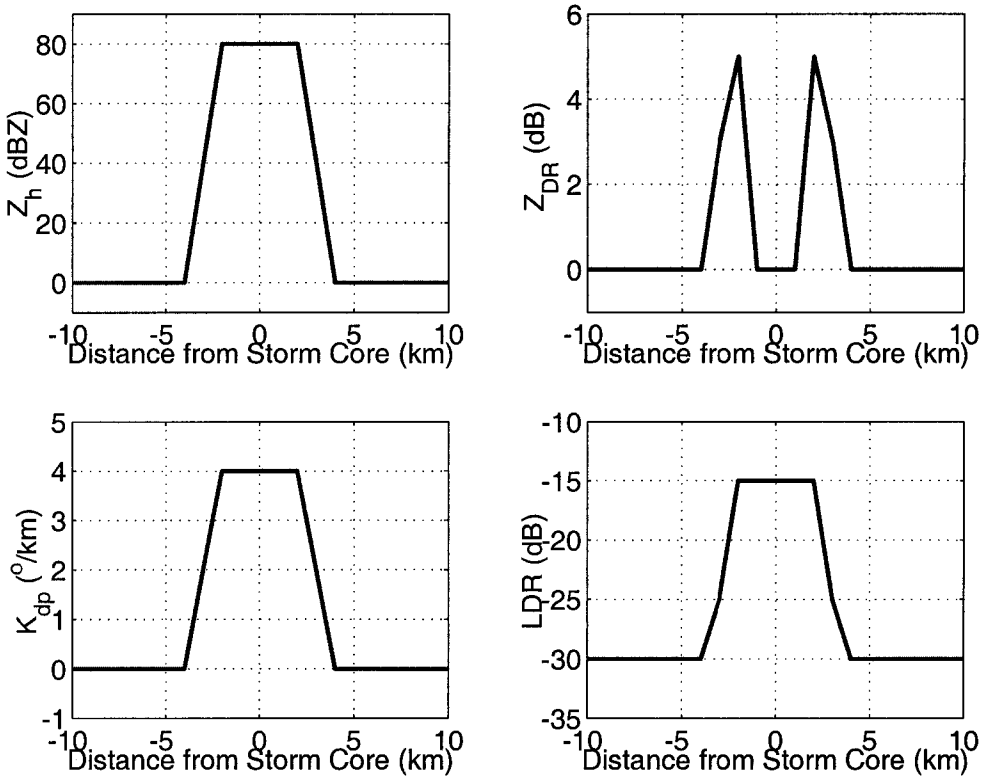

Figure 2.3: The axial profiles of intrinsic Z_h, Z_{DR}, K_{dp}, and LDR for the synthetic storm. The relative distance is shown along X-axis.

its intrinsic value to be 1. If simulated ρ_{co} is less than 0.99 after convolution, we assume that the measured Z_{DR} may be contaminated with errors. From the antenna patterns of CSU-CHILL as shown in Fig.2.1, mismatch may also exist in the mainlobe. Such Z_{DR} errors can be detected by observing the simulated Z_{DR} with zero input. Regarding the errors due to mismatch, the decision will be based on apparent non-zero values in the simulated Z_{DR}, e.g., $|Z_{DR}| > 0.6$ dB in this simulation. Then, Z_{DR} in these locations will be marked as "bad". Fig.2.4 shows a CAPPI plot of the "measured" Z_{DR}, the "simulated" Z_{DR}, the "simulated" ρ_{co}, and the masked Z_{DR} at the height of 5 km. From this figure, we learn that the Z_{DR} errors in practice may be larger than that analyzed without gradients [27], and most regions with error can be detected even though some residual error still exists (see the white 'masked' region in the figure).

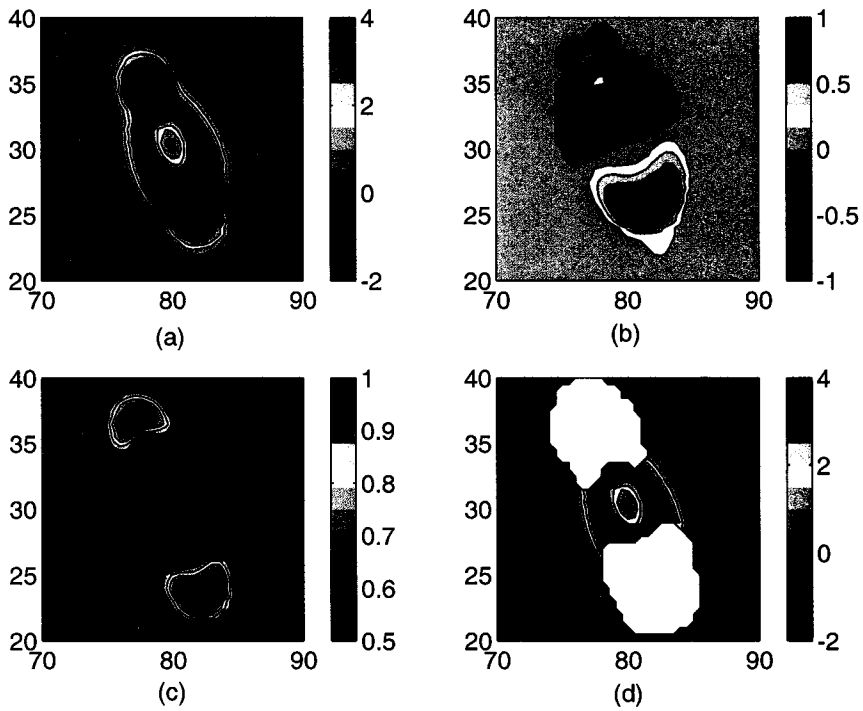

Figure 2.4: Detection of Z_{DR} errors for the synthetic storm by the CSU-CHILL radar. The illustrated CAPPI plots are taken at the 5 km height: (a) radar 'measured' Z_{DR}; (b) simulated Z_{DR} (assuming its intrinsic value 0); (c) simulated ρ_{co} (assuming its intrinsic value 1); (d) 'masked' Z_{DR}. The X-axis refers to the distance east to CSU-CHILL radar in km and Y-axis to the north.

After convolution, negative K_{dp} could be observed even though its intrinsic profile is non-negative as indicated by the input K_{dp} profile in Fig.2.3. The measured Φ_{dp} is so sensitive to the fluctuation of the intrinsic Φ_{dp} that we cannot detect its error structure based on the difference on the "simulated" data. Instead, we force the measured Φ_{dp} to increase monotonically and take that as its input profile. After convolution, negative values of the simulated K_{dp} are detected and these locations are prone to polarimetric errors for Φ_{dp} and K_{dp}. Note that usually negative K_{dp} is only expected in the upper parts of a thunderstorm due to vertically oriented ice crystals, and very infrequently below the melting level (i.e., rain or hail). The "measured" K_{dp} and estimated K_{dp} are given in the CAPPI plot as shown in Fig.2.5. We acknowledge that not all of the errors could be masked and

the positive K_{dp} error cannot be detected by this method, but it is helpful to sort out most of the erroneous negative K_{dp} area.

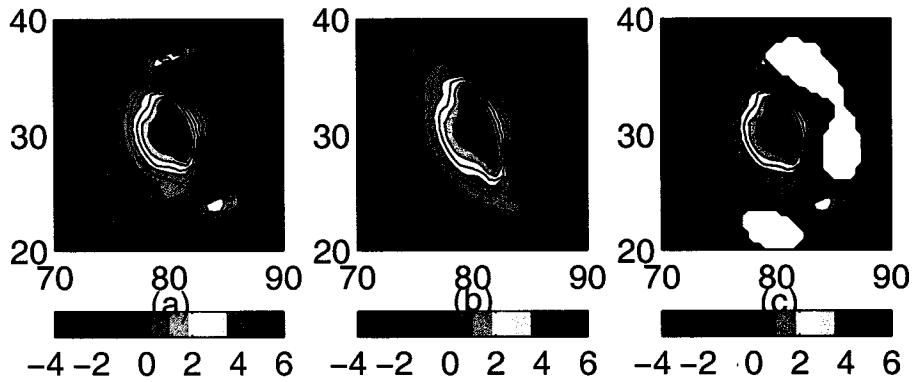

Figure 2.5: Detection of K_{dp} errors for the synthetic storm by the CSU-CHILL radar. Same as Fig.2.4 except that: (a) 'measured' K_{dp}; (b) simulated K_{dp} (forcing its input profile monotonously increasing); (c) 'masked' K_{dp}.

For LDR, our objective is to estimate the system bias as indicated by (2.15). Since the phase information of the cross-polar patterns are unavailable, we drop off the phase terms and use $|g_h g_v e_h e_v|$ directly (which makes the estimated bias a little larger). By taking the propagation effects into account, the co-polar correlation is equivalent to

$$\langle S_{hh} S_{vv}^* \rangle = |S_{hh} S_{vv}| e^{-j\Phi_{dp}} \tag{2.17}$$

The convolution based on (2.15) gives the estimate of LDR bias and this estimate is used to adjust the "measured" LDR. We know that the LDR upper bound for the CSU-CHILL radar is close to -34 dB assuming no gradients across the beam; thus, we will cast doubt over that region where the estimated bias exceeds -31 dB and mark the value at that location as "bad" data. Fig.2.6 shows the relative CAPPI plots. Nearly all the extreme LDR errors are marked out, as indicated by the white "masked" region in the last panel.

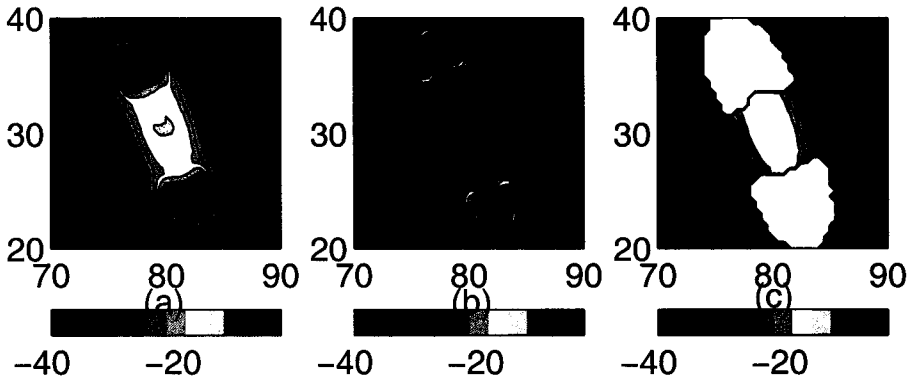

Figure 2.6: Detection of LDR errors for the synthetic storm by the CSU-CHILL radar. Same as Fig.2.4 except that: (a) 'measured' LDR; (b) estimated LDR bias; (c) 'masked' LDR.

To illustrate the spatial dependency of the antenna-induced polarimetric errors, we next run the same simulation using another radar (NCAR S-Pol) that was "deployed" at a different location, as configured in the STEPS project.

Radar Facility	Latitude (deg:min:sec)	Longitude (deg:min:sec)	Altitude (km)	Relative Distance (km)
CSU-CHILL	39:14:4.578	-102:-16:-40.438	1.285	(0,0)
NCAR-SPOL	39:45:40.109	-102:-5:-36.469	1.103	(14.031E,58.941N)

Table 2.1: Locations of the radars deployed in the STEPS project

The NCAR S-Pol antenna patterns come with 2-D raster measurement as shown in Fig.2.7 (i.e., no need for interpolation). The simulation results and the estimation of polarimetric errors, as done for the simulation with CSU-CHILL, are presented on Figs.2.8-2.10. The error structures are closely dependent on the scan geometry compared to the results for CSU-CHILL. When detecting the LDR bias for NCAR S-Pol, the threshold was set to -27 dB since its system upper bound is known to be close -30 dB. Moreover, for comparison, it is good to get the measured LDR adjusted using the estimated bias even though such adjustment will not exactly recover the polarimetric error on LDR.

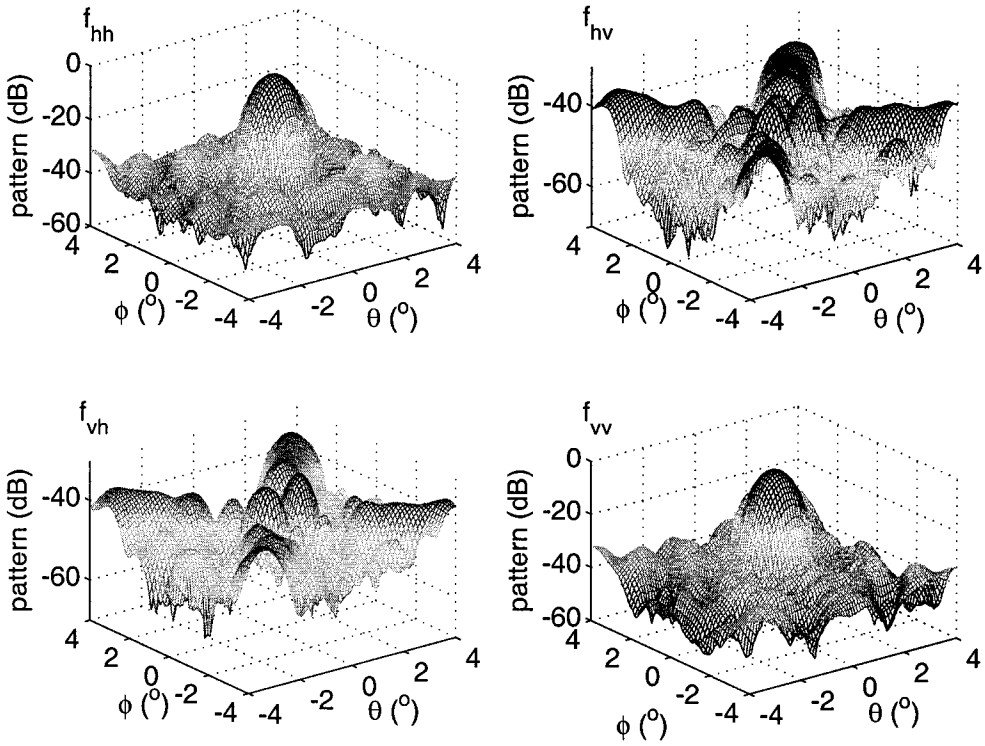

Figure 2.7: The measured antenna patterns for the NCAR S-Pol radar

The methodology developed above is based on a number of assumptions since unknown factors exist in the model, but as demonstrated by simulation the regions of large error can be detected using such an approach. The performance evaluation is listed in Table 2.2. The detection of K_{dp} error is low since the antenna-induced error on K_{dp} exists in pairwise with negative and positive biases but this method can only deal with the negative one. Note also that the performance depends on the selected thresholds, for which histograms could be utilized as a guideline.

2.4 Case Study

In this section, the methodology proposed above will be applied to a case from the STEPS project. On June 22, 2000, a severe storm developed from west of the CSU-CHILL radar and later moved northeast toward the NCAR S-Pol radar. Up to 1-inch hail was reported. Fig.2.11 shows a PPI scan of this storm at 23:23 UTC

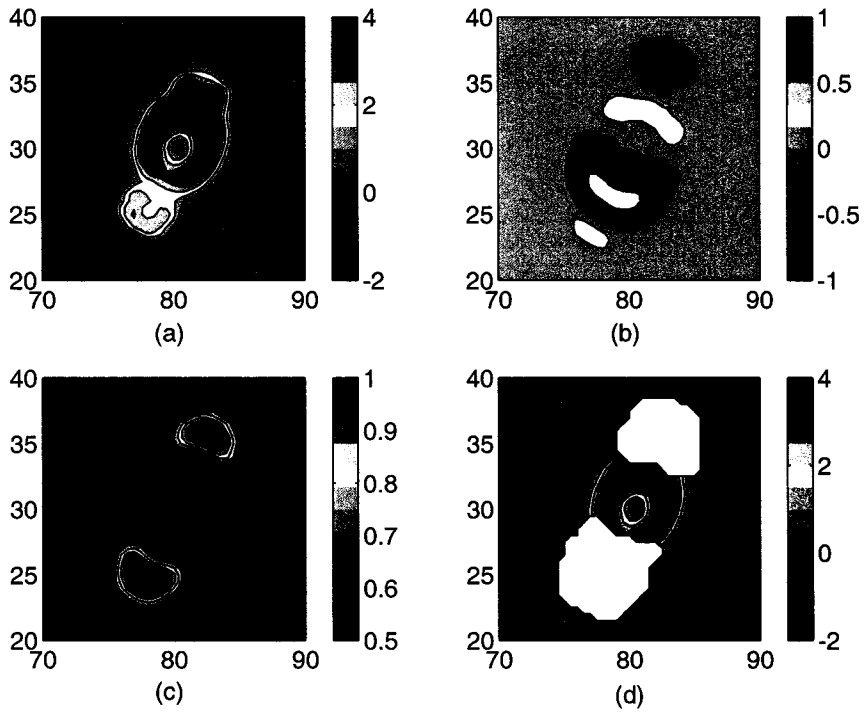

Figure 2.8: Detection of Z_{DR} errors for the synthetic storm by the NCAR S-Pol radar. Same as Fig.2.4 except that: (a) radar 'measured' Z_{DR}; (b) simulated Z_{DR}; (c) simulated ρ_{co}; (d) 'masked' Z_{DR}.

with its location relative to the three coordinated radars in the STEPS project. Large gradients are obvious in this storm. The storm is located somewhat closer to NCAR S-Pol but the different observation angles for CSU-CHILL and NCAR S-Pol are sufficient to show the dependence of the antenna-induced polarimetric errors on scan geometry.

To make the radar measurement closer to the intrinsic values, attenuation-correction is first conducted on the data set for both Z_h and Z_{DR}. In addition, K_{dp} was retrieved by linear fitting over raw Φ_{dp} and negative K_{dp} was forced to 0. Then the new smoothed Φ_{dp} was reconstructed from the pruned K_{dp} profile and was applied as input to the 2-D convolution. Besides, we assume ρ_{co} is 1 and intrinsic LDR is 0 ($-\infty$ dB) as input.

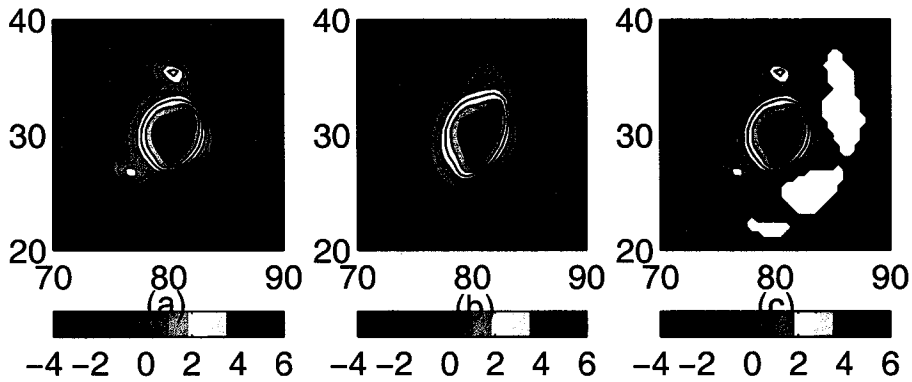

Figure 2.9: Detection of K_{dp} errors for the synthetic storm by the NCAR S-Pol radar. Same as Fig.2.4 except that: (a) 'measured' K_{dp}; (b) simulated K_{dp}; (c) 'masked' K_{dp}.

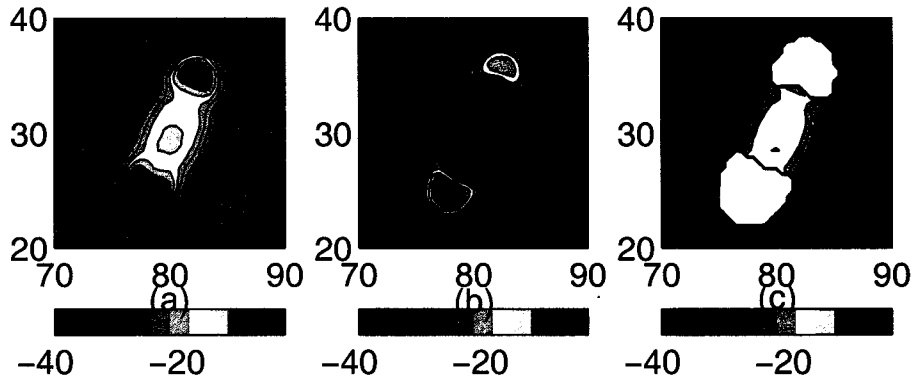

Figure 2.10: Detection of LDR errors for the synthetic storm by the NCAR S-Pol radar. Same as Fig.2.4 except that: (a) 'measured' LDR; (b) estimated LDR bias; (c) 'masked' LDR.

Before labelling the antenna-induced polarimetric errors, the related histograms were investigated to help establish the thresholds on simulated ρ_{co}, Z_{DR}, and LDR bias as listed in Table 2.3.

Fig.2.12 shows the radar measurement by CSU-CHILL for this storm and the corresponding simulated variables with CAPPI plots on the height (AGL) of 2.5 km. Panel (a) refers to the CAPPI plot of Z_h where the dash line presents the scanning direction through the storm core from the view of the CSU-CHILL radar. On the right side of the storm core, the reflectivity drops from 65 dB to

Error detection		Z_{DR}	K_{dp}	LDR
Criteria for error samples		$\lvert\Delta Z_{DR}\rvert > 0.6$dB	$\lvert\Delta K_{dp}\rvert > 0.6^o$/km	$\Delta LDR > 3$dB*
				$\Delta LDR > 4$dB**
Detection Thresholds		$\rho_{co}^{sim} < 0.99$	$K_{dp}^{sim} < 0$	$LDR^{sim} > -31$dB*
		$\lvert Z_{DR}^{sim}\rvert > 0.6$dB		$LDR^{sim} > -27$dB**
CHILL	Error samples	7644	11080	10400
	Detection rate	6451 (83.92%)	2060 (18.59%)	8922 (85.79%)
	False rate	3063 (40.07%)	1859 (16.77%)	1086 (10.44%)
S-Pol	Error samples	5633	5616	7724
	Detection rate	4430 (78.64%)	1045 (18.60%)	6129 (79.35%)
	False rate	2724 (48.36%)	2317 (41.25%)	354 (4.58%)

* for CHILL;
** for S-Pol.

Table 2.2: The performance of the developed error detection scheme

Radar Facility	Threshold $\lvert Z_{DR}\rvert$	Threshold on LDR Bias	Threshold on ρ_{co}
CSU-CHILL	0.3 dB	0.995	-32 dB
NCAR S-Pol	0.2 dB	0.995	-29 dB

Table 2.3: Thresholds on simulated radar variables (Z_{DR}, ρ_{co} and LDR bias) for detection of the antenna-induced polarimetric errors

below 50 dB at (-38 km, 70 km), and such gradient appears across the radar beam direction. Panel (b) shows that the Z_{DR} is very low around the storm core and large Z_{DR} exists in some surrounding spots. Panels (d) and (e) refer to the CAPPI plots of measured and simulated ρ_{co}, respectively. Note that overall, these two signatures do not resemble each other. In the lower left and upper left part of the measured ρ_{co}, its value is as low as 0.9, while the simulated ρ_{co} shows large values for most of these locations. The low measured value could be attributed to mixed type precipitation or poor signal quality. In general, the surrounding low reflectivity areas have low correlation coefficients in both measured CAPPI plot and simulated plot. So is that for the location around (-38 km, 70 km), which means the existence of gradient related polarimetric errors on the measured Z_{DR}. The simulated Z_{DR} panel could provide additional information to detect the errors that result mainly from mismatched patterns. On the area more than 50 km west

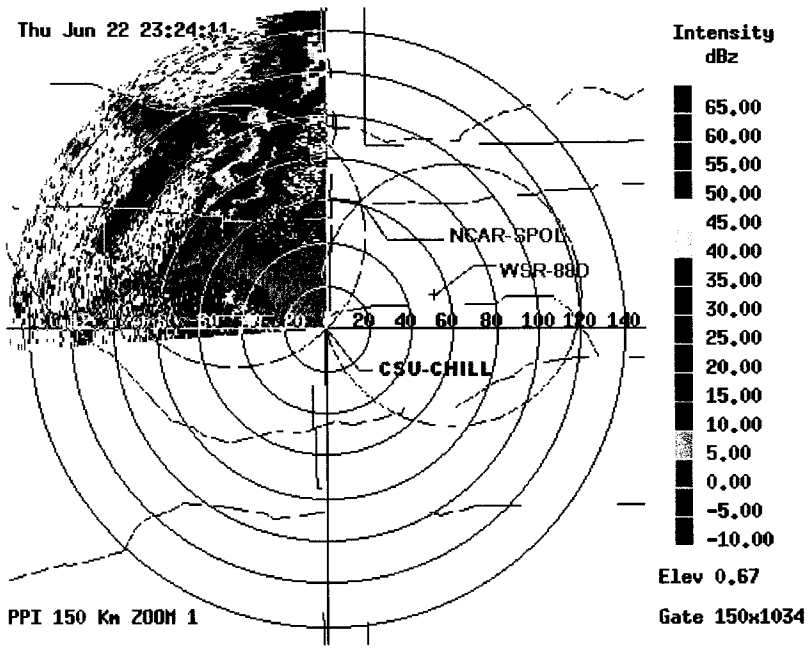

Figure 2.11: A PPI scan of the severe storm on June 22, 2000 in low elevation angle with the locations of three coordinated radars labelled.

and from 60 km to 70 km north of CSU-CHILL, the simulated Z_{DR} shows apparent non-zero values. The corresponding measured Z_{DR} is very large, which is probably caused by mismatched co-polar patterns. Those areas finally get marked out as shown in panel (f).

Similarly, Fig.2.13 illustrates the detection scheme applied for NCAR S-Pol. From panel (a), the gradient in reflectivity across the radar beam for NCAR S-Pol is not as dramatic as that in CSU-CHILL at the location around (-38 km, 70 km). Instead, sharp gradients may exist across the beam south of (-45 km, 70 km). The simulated Z_{DR} as shown in panel (c) does not have significant bias from zero, which might be due to the co-polar patterns of the NCAR S-Pol radar being better matched as compared to the CSU-CHILL radar, or that the mismatch of S-Pol patterns are distributed more uniformly since the CSU-CHILL patterns are interpolated over only 4 planes. Again, the measured ρ_{co} and simulated ρ_{co} show different signatures: the measured ρ_{co} has high correlation over most of storm cell,

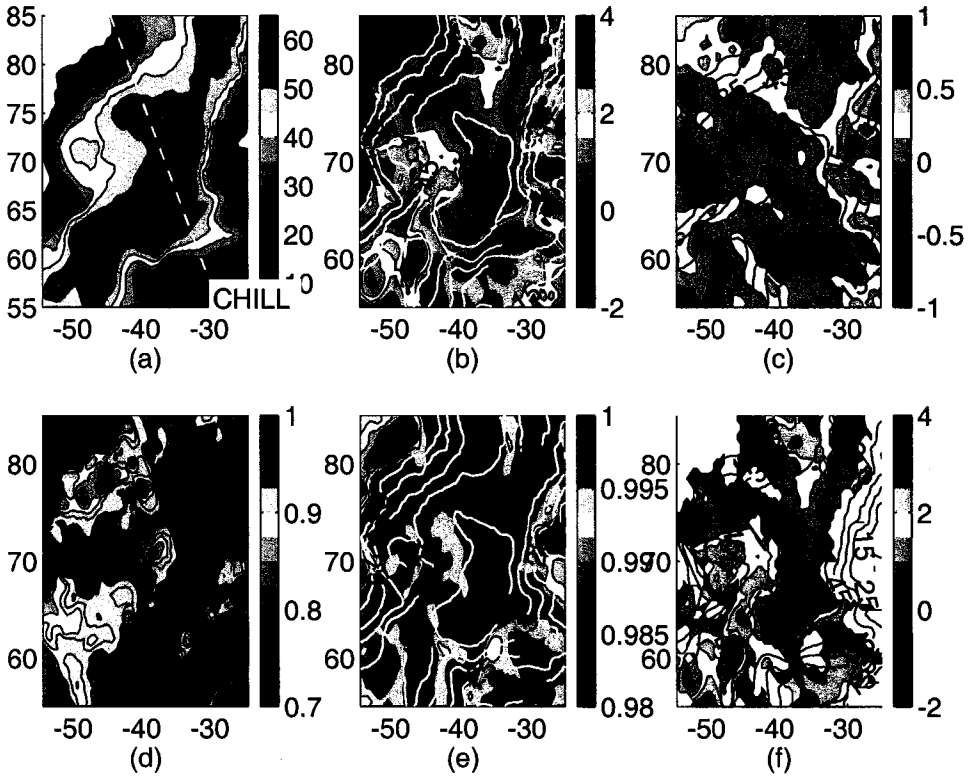

Figure 2.12: Composite CAPPI plots at 2.5 km AGL to illustrate the detection scheme for CSU-CHILL measured Z_{DR}: (a) radar measured Z_h (dBZ) with beam direction through the storm core; (b) radar measured Z_{DR} (dB); (c) simulated Z_{DR} (dB) assuming its intrinsic value zero; (d) radar measured ρ_{co}; (e) simulated ρ_{co} assuming its intrinsic value 1; (f) radar measured Z_{DR} (dB) with error prone locations marked (as white). The X-axis refers to distance (km) on east from CSU-CHILL and Y-axis to that on north.

while the simulated one has low correlation over storm edges, e.g., the area at south of (-45 km, 70 km). The CAPPI plot of the measured Z_{DR} in panel (f) with error-prone locations marked out is consistent with our observation on other panels. Note that the marked area does not coincide with the continuous measured Z_{DR}. It is a common problem at using crispy set defined by thresholds. By comparing the marked results over CHILL and S-Pol, regardless of the discontinuities, we are still able to obtain direction dependent error-prone locations, e.g., S-Pol has good view on the location around (-38 km, 70 km) while CHILL has good view on the locations at south of (-45 km, 70 km) and around (-36 km, 82 km).

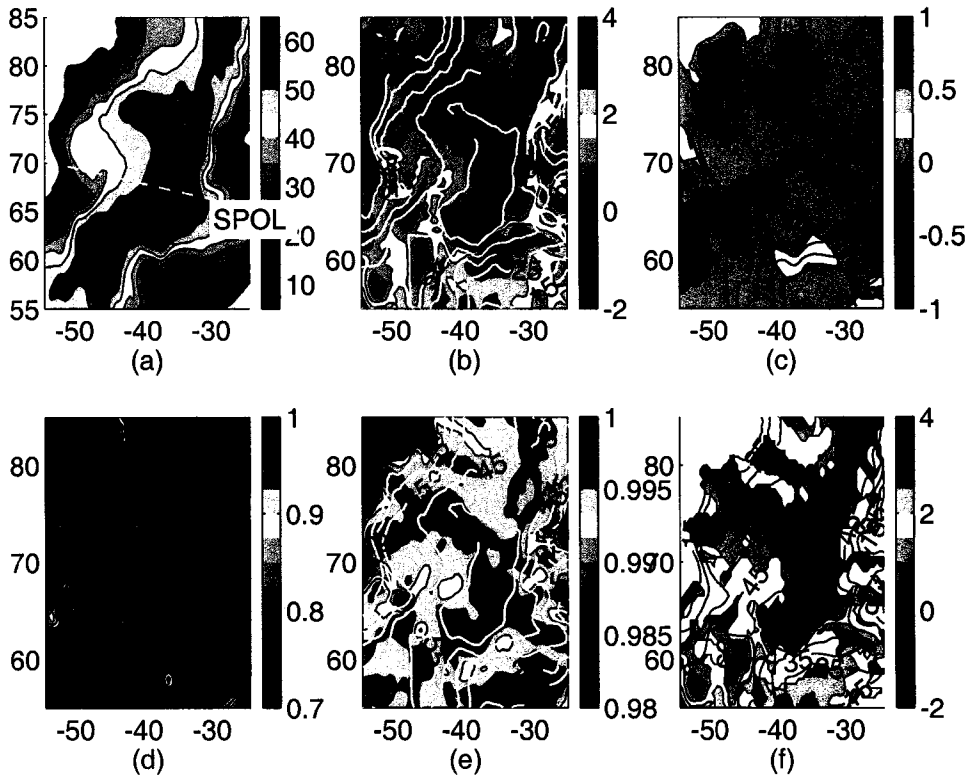

Figure 2.13: Composite CAPPI plots at 2.5 km AGL to illustrate the detection scheme for NCAR S-Pol measured Z_{DR}: all the panels are arranged in the same manner as the previous figure.

In Fig.2.14, panels (a) and (d) show the CAPPI plots of measured K_{dp} by CSU-CHILL and NCAR S-Pol, respectively. Large area of negative K_{dp} is obvious in both plots. Besides, compared to the measurement by S-Pol, CHILL gives high reading for K_{dp} at some spots neighboring the deep negative region, e.g., around (-38 km, 71 km) and (-42.5 km, 84 km), which likely is also caused by the antenna induced errors according to previous analysis. The simulated K_{dp}, assuming its intrinsic value is monotonically increasing, is shown in panels (b) and (e) for both radars, respectively. Apparently, most of the areas with negative values in measurement are still contaminated with negative values in simulation. The marking scheme is simple: marking out all the locations with negative values in the simulated K_{dp}. Panels (c) and (f) illustrate the final marked results for both

radars. Most of the radar measured negative K_{dp} is detected for both radars which is located behind the storm core. Such marking is also significant in the sense of correcting microphysical interpretation since some marked areas come with high reflectivity. The intriguing feature is that the regions with positive errors cannot be detected with this scheme. With this fact in mind, we cast doubt over the significant positive K_{dp} on the surrounding areas close to the detected negative K_{dp} errors, e.g., at location (-50 km, 70 km) for S-Pol and at locations (-38 km, 71 km), (-39 km, 76 km), (-42.5 km, 84 km) for CHILL.

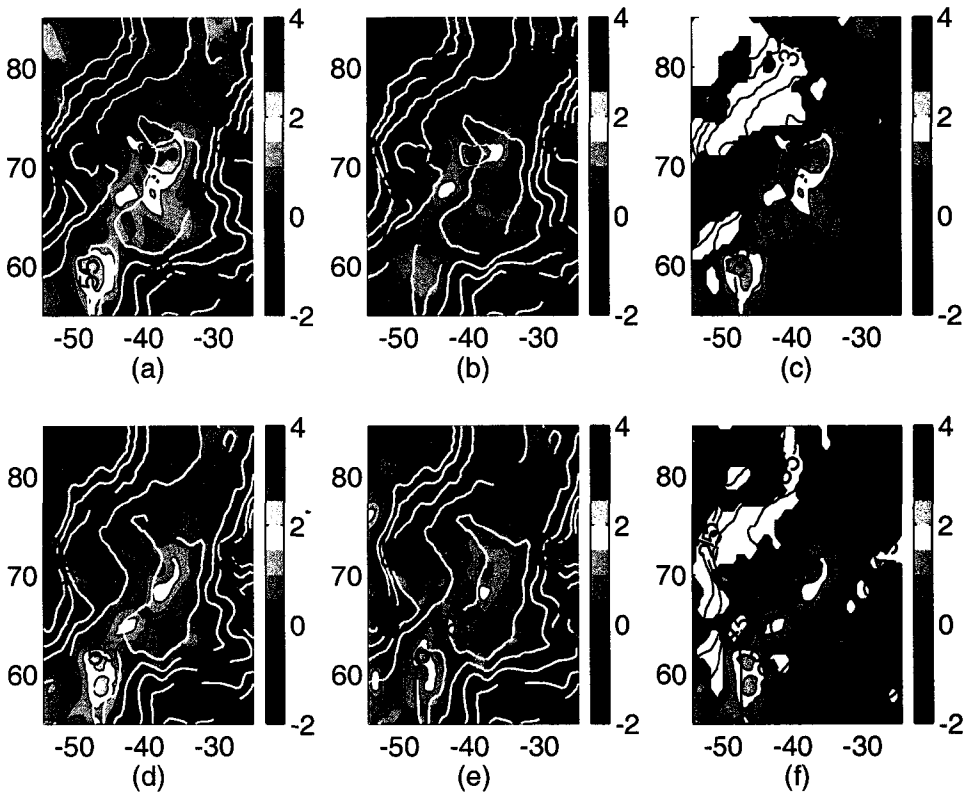

Figure 2.14: Composite CAPPI plots at 2.5 km AGL to illustrate the detection scheme for measured K_{dp}: (a) radar measured K_{dp} (deg/km) by CHILL; (b) simulated K_{dp} (deg/km) for CHILL assuming its intrinsic value monotonously increasing; (c) radar measured K_{dp} (deg/km) by CHILL with error prone locations marked out; (d) (e) (f) are same to (a) (b) (c) except for NCAR S-Pol.

The detection scheme for LDR bias is illustrated in Fig.2.15. Similarly, the top panels refer to the CAPPI plots for CSU-CHILL while the bottom panels for NCAR S-Pol. Panels (a) and (d) show the radar measured LDR by CHILL and S-Pol, respectively. The whitened region on the S-Pol plot was labelled as invalid data on tape probably due to signal quality issues. Panels (b) and (e) give the simulated LDR bias using patterns of CHILL and S-Pol. Apparently, CHILL's cross-polar patterns outperforms S-Pol's. The simulated LDR for CHILL is equal to or less than the system upper bound in most of the storm cell. After taking the simulated LDR bias out from the radar measurement, the marked CAPPI plots of LDR are shown in panels (c) and (f). Most of the storm edges are marked out as error-prone locations for LDR, which would be handled with SNR threshold anyway. However, the bias adjustment does drive the LDR measurement by both radars towards consistency.

Certainly, the antenna induced polarimetric errors do not seem very outstanding compared to the simulation. Also, partly because of timing and discontinuities, it seems impossible to merge the two data sets obtained by CHILL and S-Pol. However, the marking scheme can present reasonable detection which is geometry dependent. After discarding these data with errors, we can assume the measurement is less affected by gradients, and point polarization calibration could be implemented.

It should be pointed out that both Z_h and Z_v are expanded during the convolution process in radar measurement and such expansion will result in the detected errors probably aligned away off the actual errors. Also, Φ_{dp} gets smoothed and that results in less occurrence of negative K_{dp} error.

2.5 Evaluation of Antenna Performance

Even though the antenna-induced polarimetric errors can be modelled as discussed above, and the specific regions suffering such errors can be determined by

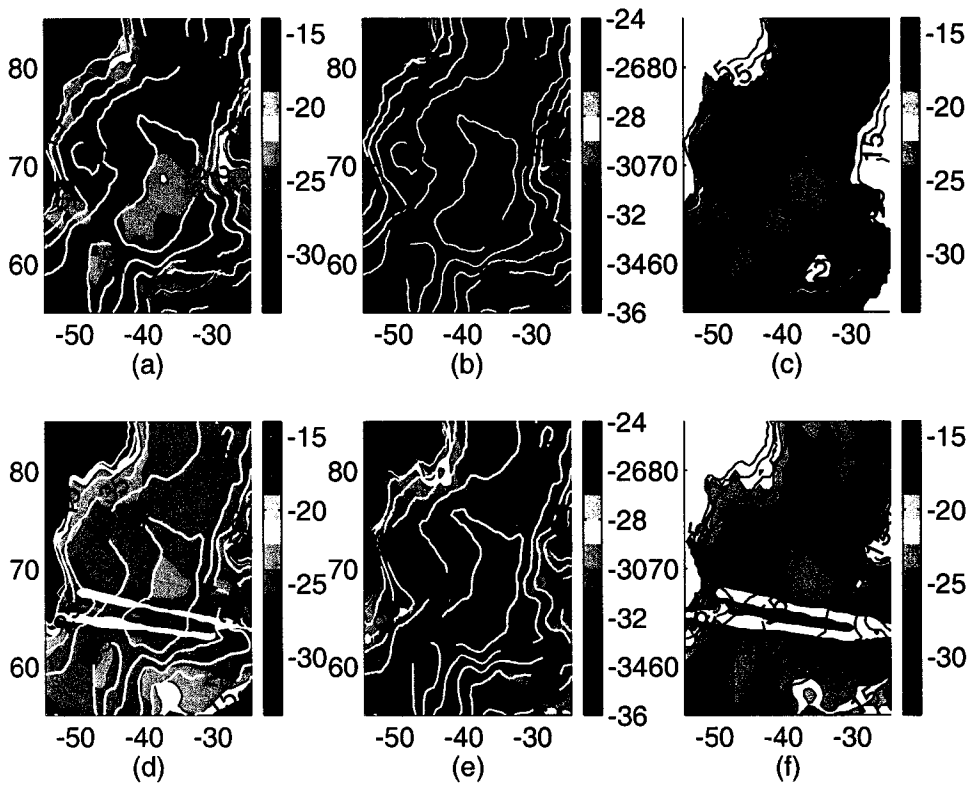

Figure 2.15: Composite CAPPI plots at 2.5 km AGL to illustrate the detection scheme for measured LDR: (a) radar measured LDR (dB) by CHILL; (b) simulated LDR bias (dB) for CHILL; (c) radar measured LDR (dB) by CHILL with estimated bias adjusted and error prone locations marked out; (d) (e) (f) are same to (a) (b) (c) except for NCAR S-Pol.

the given methodology using the measured reflectivity, there is no way to "correct" for these errors. Given the estimated LDR bias, the measured LDR can only be partially corrected. In addition, it is also near gradients, e.g., near the updraft/downdraft interface in severe storms, that are often of most interest microphysically and kinematically. Therefore, the essential way to improve polarimetric data quality is to improve the antenna performance.

The antenna performance can be evaluated via a variety of parameters such as antenna gain, beamwidth, sidelobe level and polarimetric related considerations such as mismatch, cross-polar level, etc. The antenna gain specifies the power gain achieved in boresight relative to an isotropic radiator and the beamwidth specifies

the angular resolution of an antenna. Besides, the sidelobe performance and cross-polar performance are also vital for an antenna to achieve high quality polarimetric measurements apart from the antenna gain and beamwidth.

For applications in radar meteorology where large gradients are very possible in reflectivity, low sidelobe envelope of the antenna co-polar patterns are highly desirable because the co-polar patterns play an important role in radar variables such as Z_{DR}, K_{dp}, LDR and co-to-cross polar correlation coefficients. High sidelobe level would result in "ghost" image on related signatures, which picks up the values from neighboring regions coincident with sidelobes for the current steered location. It is also worth to note that for Z_{DR} its error may come from mismatch of co-polar patterns which could be controlled in design for mainlobe but not for sidelobes. For LDR it is less well appreciated that errors would come from strong spatial gradients of reflectivity. A detailed examination of the sidelobe level can be done through comparing the co-polar patterns to the log-curve specified envelope, which is defined by function:

$$f(\theta) = f_1 + k \cdot \log_{10} \theta \tag{2.18}$$

where θ represents the off-axis angle in degree. Overall evaluation for sidelobe could be obtained by the Peak Sidelobe Level (PSL), which is defined for H-port as

$$PSL_h = 10 \log_{10} \frac{\max_{\theta \in SL} |g_h(\theta)|^2}{|g_h(0)|^2} \tag{2.19}$$

where 'SL' stands for sidelobe, and the Integrated Sidelobe Level (ISL) for H-port as

$$ISL_h = 10 \log_{10} \frac{\int_{\theta \in SL} |g_h(\theta)|^2 d\theta}{\int_{\theta \in ML} |g_h(\theta)|^2 d\theta} \tag{2.20}$$

where ML stands for mainlobe. Without losing generality, hereafter only parameters for H polarization state will be presented.

To obtain high quality cross-polar radar variables, we want to diminish the cross-polar contamination, which means that the cross-polar patterns should be as low as possible relative to the co-polar patterns at least in the mainlobe. The Integrated Cross-polar Level (ICL) for H-port

$$ICL_h = 10\log_{10}\frac{\int |e_h(\theta)|^2 d\theta}{\int |g_h(\theta)|^2 d\theta} \tag{2.21}$$

gives an overall merit of the inter-channel isolation of the antenna. However, it is not enough to fully characterize such merit because as indicated by (2.11) the cross-polar variables are contaminated with leakage from strong co-polar echoes through the cross product terms between co-polar and cross-polar antenna patterns. The additional evaluation parameters for LDR include the (two-way) integrated cross-polar ratio (ICPR2) over every ϕ-plane

$$ICPR2_h = 10\log_{10}\frac{\int |g_h(\theta)e_v(\theta)|^2 d\theta}{\int |g_h(\theta)|^4 d\theta} \tag{2.22}$$

and the system upper bound of LDR integrated over the full beam

$$LDR_h^{ub} = 10\log_{10}\frac{\iint (|g_h e_v| + |g_v e_h| + 2\sqrt{|g_h g_v e_h e_v|}) d\Omega}{\iint |g_h|^4 d\Omega} \tag{2.23}$$

Similarly, the co-to-cross polar correlation coefficients ρ_{xh} and ρ_{xv} are affected by cross-polar patterns with functional relation that can be derived from (2.2) and the system upper bound can be written as:

$$\rho_{xh}^{ub} = 10\log_{10}\frac{\iint |g_h|^2 (\sqrt{|g_h e_v|} + \sqrt{|g_v e_h|}) d\Omega}{\iint |g_h|^4 d\Omega} \tag{2.24}$$

To improve the antenna sidelobe performance in all planes antenna designs such of offset or dial-offset reflectors should be considered. Dual-offset geometry design avoids aperture blockage but allows for both exceptional sidelobe and cross-polar performance in all planes [28]. With a grant from NSF, the CSU-CHILL facility will undergo a major upgrade by replacing the current prime-focus reflector antenna with a 9-meter dual-offset Gregorian antenna. The designed antenna

patterns on selected planes are shown in Fig.2.16. A very strict sidelobe envelope specification were enforced to the design of new antenna. To compare the designed patterns with those of the current CSU-CHILL antenna, the current patterns are re-plotted in Fig.2.17 with the specified sidelobe envelope. A rough examination of the patterns shows that big improvements would be achieved with the new antenna design: the new antenna will meet the stringent envelope on all planes while the current antenna exceeds such specification. Table 2.4 lists the performance evaluations for the new antenna and the current antenna side-by-side.

Antenna Version		Current		New	
Polarization Port		H	V	H	V
Gain (dB)		43	43	45.8	45.8
3dB Beamwidth (^{o})	0^o-plane	1.002	1.010	0.968	0.968
	45^o-plane	1.004	1.006	0.968	0.968
	90^o-plane	1.010	1.006	0.968	0.966
PSL* (dB)	0^o-plane	-32.77	-37.95	-34.64	-35.07
	45^o-plane	-29.54	-28.44	-36.13	-35.73
	90^o-plane	-32.93	-36.86	-37.08	-37.02
ISL* (dB)	0^o-plane	-26.04	-29.11	-31.75	-31.78
	45^o-plane	-23.77	-23.59	-33.16	-33.18
	90^o-plane	-28.49	-25.55	-32.90	-31.97
ICL (dB)	0^o-plane	-40.32	-40.18	<-45	<-45
	45^o-plane	-28.11	-27.61	-40.30	-37.75
	90^o-plane	-40.70	-42.09	-39.02	-35.91
ICPR2 (dB)	0^o-plane	-46.89	-46.50	<-45	<-45
	45^o-plane	-40.62	-38.84	-42.30	-45.34
	90^o-plane	-48.84	-46.55	-39.54	-42.80
ISL* (dB)		-16.73	-16.48	-23.32	-23.30
LDR^{ub} (dB)		-33.87	-33.87	-34.47	-34.47
ρ_{cx}^{ub} (dB)		-18.60	-18.54	-18.09	-18.09

*: the mainlobe is defined as 30dB beamwidth.

Table 2.4: The performance evaluation for the current CSU-CHILL antenna and the new designed CSU-CHILL antenna

The sidelobe level for the new designed antenna will be lower than -35 dB on all planes compared to -28 dB for the current antenna on the worst plane; the cross-polar patterns are uniformly lower than co-polar patterns and better

overall isolation would be obtained; excellent performance will be maintained in all planes. Note that the ICPR2 and LDR upper bound do not get much improved despite better isolation, which is due to the peak of the cross-polar pattern comes closer to boresight. The generated patterns for the new antenna design could also be applied to the synthetic storm to further examine its performance under high gradient scenario, and it is found all polarimetric errors are dramatically reduced.

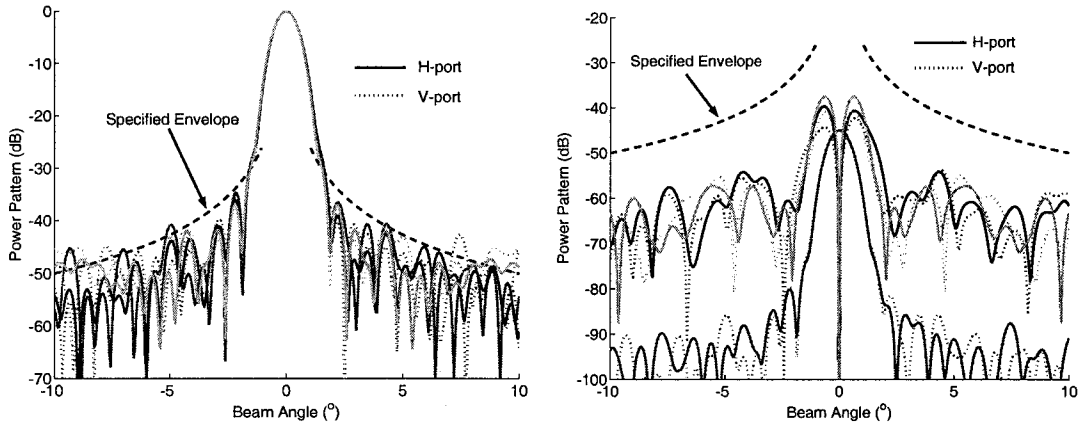

(a) co-polar (b) cross-polar

Figure 2.16: The co-polar and cross-polar patterns of the new designed CSU-CHILL antenna with the specified envelope: the patterns on 0°, 45° and 90° planes are plotted; random surface errors are applied when generating those patterns.

2.6 Summary

The antenna performance is of great importance for achieving high quality polarimetric measurements. A well-designed antenna should be able to maintain both high inter-channel isolation and low sidelobe level. High reflectivity gradients will usually be experienced in many types of storm events. For such cases, the sidelobe level would be even more critical and significant antenna-induced polarimetric errors might exist if the sidelobes are relatively large. These errors need to be detected and sorted out before any implications can be drawn from the measurements. Due to the convolution effect, analysis of only the reflectivity gradients

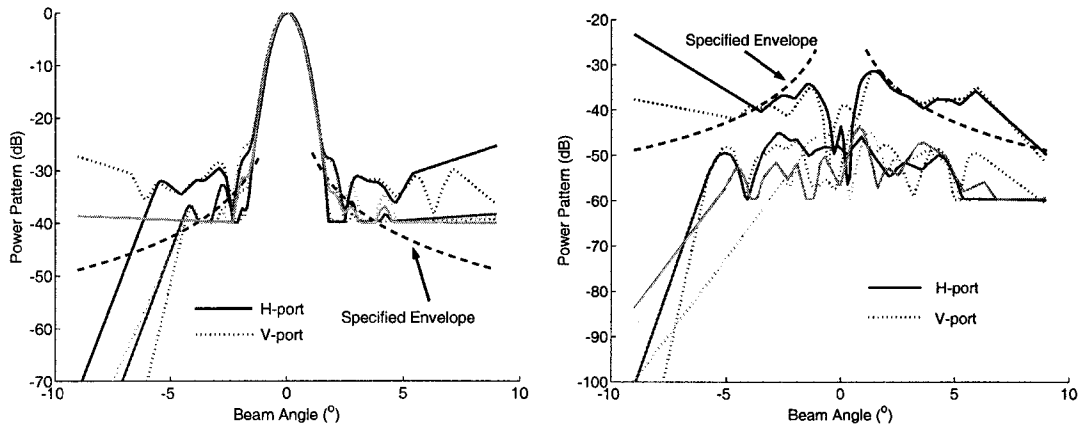

(a) co-polar (b) cross-polar

Figure 2.17: The co-polar and cross-polar patterns of the current CSU-CHILL antenna with the specified envelope: the patterns on 0°, 45° and 90° planes are plotted; those patterns are obtained at test range.

will not locate such polarimetric errors. A 2-D convolution was implemented to this end.

The synthetic storm simulation demonstrates a possible procedure for detection of antenna-induced polarimetric errors in the presence of large gradients. The full 2-D antenna patterns (both co-polar and cross-polar) must be known, and we further introduce random phase outside the mainlobe to more realistically simulate ρ_{co} and Φ_{dp} errors. We have used measured data from a severe, convective storm to illustrate the detection of antenna-induced errors in Z_{DR}, K_{dp} and LDR. Gradients above 20 dB across the beam can be found in reflectivity and apparent polarimetric errors have been detected and marked. The results for two radars deployed on different sites also demonstrate the spatial dependence of the errors, which further validates the detection scheme. Such masking will be useful for improving data quality without "correcting" the data, especially when such data are used for rain rate estimation and hydrometeor classification.

Procedures for "correcting" the polarimetric data when the precipitation is homogenous can be found in [19], [27], [29], and in the later sections of this work

(chapter 4). However, considering the antenna-induced errors, correction is infeasible since the only way to reconstruct is through exact deconvolution. Even the estimation of error structure is very complicated as shown in this work.

To improve the data quality and to utilize the full covariance matrix, well-designed antennas especially with excellent sidelobe and cross-polar performance are needed. Dual-offset geometry design can make possible excellent performance on all planes. The performance of the new 9-m dual-offset Gregorian antenna under design for the CSU-CHILL radar was evaluated and great improvement is shown compared to the current antenna.

Chapter 3

STUDY ON POLARIMETRIC COVARIANCE MATRIX

The radar remote sensing for meteorology explores the underlying relation between the radar measurement and the precipitation properties. The covariance matrix has been shown to be a fundamental measure of the precipitation properties. The dual-polarization precipitation radar creates a two-dimensional complex vector space by polarimetry. The system model then can be regarded as a linear mapping on the polarization plane. The representation of the linear map undergoes unitary transformation when the vector basis changes from one orthogonal basis to another orthogonal basis.

It is well known that the radar measurement in circular polarization basis gives separate information on shape and orientation distribution [4], [6]. It is straightforward to retrieve the orientation factors from the covariance matrix in circular polarization basis and, further, the shape factors can be retrieved. Unitary transformation will be employed to obtain the circular covariance matrix from that constructed in linear polarization basis.

Since unitary transformation does not introduce any distortion to a linear mapping and all its properties are kept, it is possible to derive an algorithm to retrieve the orientation and shape factors directly from the constructed covariance matrix in linear polarization basis. The angular expectation on the canting angle will be explored to find such solution. It was also shown that the orientation factors

could be obtained from maximum and minimum LDR under real rotation of the linear polarization basis [6]. The theory of polarization optimization for random incoherent medium will be re-developed and compared with the other methods. All the algorithms will be evaluated in the whole complex transformation space.

The propagation can introduce distortion on both relative power and phase between two orthogonal channels, and even introduce depolarization along the propagation path. Such distortion will bias the estimation of the orientation factors. The effect of propagation will be studied using simulation. Non-diagonal propagation matrix is caused by non-zero canting along the path and it is infeasible to correct such propagation effect because there is no way to separate the depolarization caused by propagation from that caused by backscattering. It is generally assumed that the measurement only suffers diagonal propagation to correct the propagation effect, especially the differential phase shift in S-band.

Non-perfect antenna also introduces distortion. Antenna polarization errors can be represented by an integrated error matrix which is usually non-orthogonal. Such non-orthogonal matrix transforms the polarization basis to a pair of non-orthogonal elliptical polarization basis. Its effect on the covariance matrix will be studied and a method to estimate the antenna error matrix will be developed. The estimated error matrix can be applied back to correct for the induced distortion.

When mixed type precipitation occurs, the covariance matrix is summation of every component contributed by individual precipitation type. The contribution is generally not separable. For the mixture, the estimated orientation factors deserve particular scrutiny. The properties of mixed type precipitation will be studied last.

3.1 Polarization State of Plane Waves

A general expression for a plane wave propagating along the direction $\hat{k}$ is given as:

$$\begin{aligned}\mathbf{E}(\vec{r},t) &= (E_h\hat{h} + E_v\hat{v})e^{j\omega t}e^{-jk_0\hat{k}\cdot\vec{r}} \\ &= (|E_h|e^{j\theta_h}\hat{h} + |E_v|e^{j\theta_v}\hat{v})e^{j\omega t}\end{aligned} \tag{3.1}$$

where the unit vectors $\hat{h}$ and $\hat{v}$ are defined on the polarization plane in such a way that $\hat{v}\times\hat{h} = \hat{k}$ and $\hat{v}\cdot\hat{h} = 0$. To study the electric field at an arbitrary range r on the polarization plane $(\hat{v},\hat{h})$, we can write the above analytical expression as a two-channel real signal:

$$\mathbf{E}(t) = |E_h|\cos(\omega t + \theta_h)\hat{h} + |E_v|\cos(\omega t + \theta_v)\hat{v} \tag{3.2}$$

Its two orthogonal components are:

$$E_h(t) = |E_h|\cos(\omega t + \theta_h) \tag{3.3a}$$

$$E_v(t) = |E_v|\cos(\omega t + \theta_v) \tag{3.3b}$$

3.1.1 Linear polarization

When $\theta_v - \theta_h = 0, \pi$, based on (3.3) we have the relation:

$$E_v(t) = \pm\frac{|E_v|}{|E_h|}E_h(t) \tag{3.4}$$

which describes a linear trace on the polarization plane, whose orientation is defined by the ratio $|E_v|/|E_h|$ and whose initial position is commanded by the phase θ_h, as shown in Fig.3.1(a). Note that the electric field is also linearly polarized if either $E_h = 0$ or $E_v = 0$. The unit vectors $\hat{h}$ and $\hat{v}$ fall into such situation. Given any other linear polarization, it is easy to find its orthogonal polarization with phase lag shifted by another π.

3.1.2 Circular polarization

When $|E_h| = |E_v|$ and $\theta_v - \theta_h = \pm\pi/2$, we have the relation as

$$E_h^2(t) + E_v^2(t) = |E_h|^2 + |E_v|^2 \tag{3.5}$$

which describes a circular trace on the polarization plane. If the phase difference between v-component and h-component is $\pi/2$, $E_v(t)$ leads the cycle and the trace evolves in clockwise direction, looking along the propagation direction, as illustrated in Fig.3.1(b); otherwise, it evolves in counter-clockwise. In accordance to IEEE convention, we call the clockwise situation as right hand circular polarization (RHC) while the counter-clockwise situation as left hand circular polarization (LHC) [18]. Again, the phase θ_h commands the initial position on the trace. Without losing generality, we can set the initial phase to zero. Then,

$$E_{RHC} = E_0\hat{e}_R = E_0\frac{(\hat{h} + j\hat{v})}{\sqrt{2}}e^{j\omega t}e^{-jk_0\hat{k}\cdot\vec{r}} \tag{3.6a}$$

$$E_{LHC} = E_0\hat{e}_L = E_0\frac{(\hat{h} - j\hat{v})}{\sqrt{2}}e^{j\omega t}e^{-jk_0\hat{k}\cdot\vec{r}} \tag{3.6b}$$

It is easy to show $\hat{e}_L$ and $\hat{e}_R$ are orthogonal and relate to the linear polarization basis by

$$\begin{bmatrix} \hat{e}_R \\ \hat{e}_L \end{bmatrix} = \frac{1}{\sqrt{2}}\begin{bmatrix} 1 & j \\ 1 & -j \end{bmatrix}\begin{bmatrix} \hat{h} \\ \hat{v} \end{bmatrix} \tag{3.7}$$

3.1.3 Elliptic polarization

In all other cases, the trace of the electric field can be fully described by a family of ellipses as shown next. Starting from (3.3), we can expand the two-channel real signal as

$$\frac{E_h(t)}{|E_h|} = \cos(\omega t)\cos(\theta_h) - \sin(\omega t)\sin(\theta_h) \tag{3.8a}$$

$$\frac{E_v(t)}{|E_v|} = \cos(\omega t)\cos(\theta_v) - \sin(\omega t)\sin(\theta_v) \tag{3.8b}$$

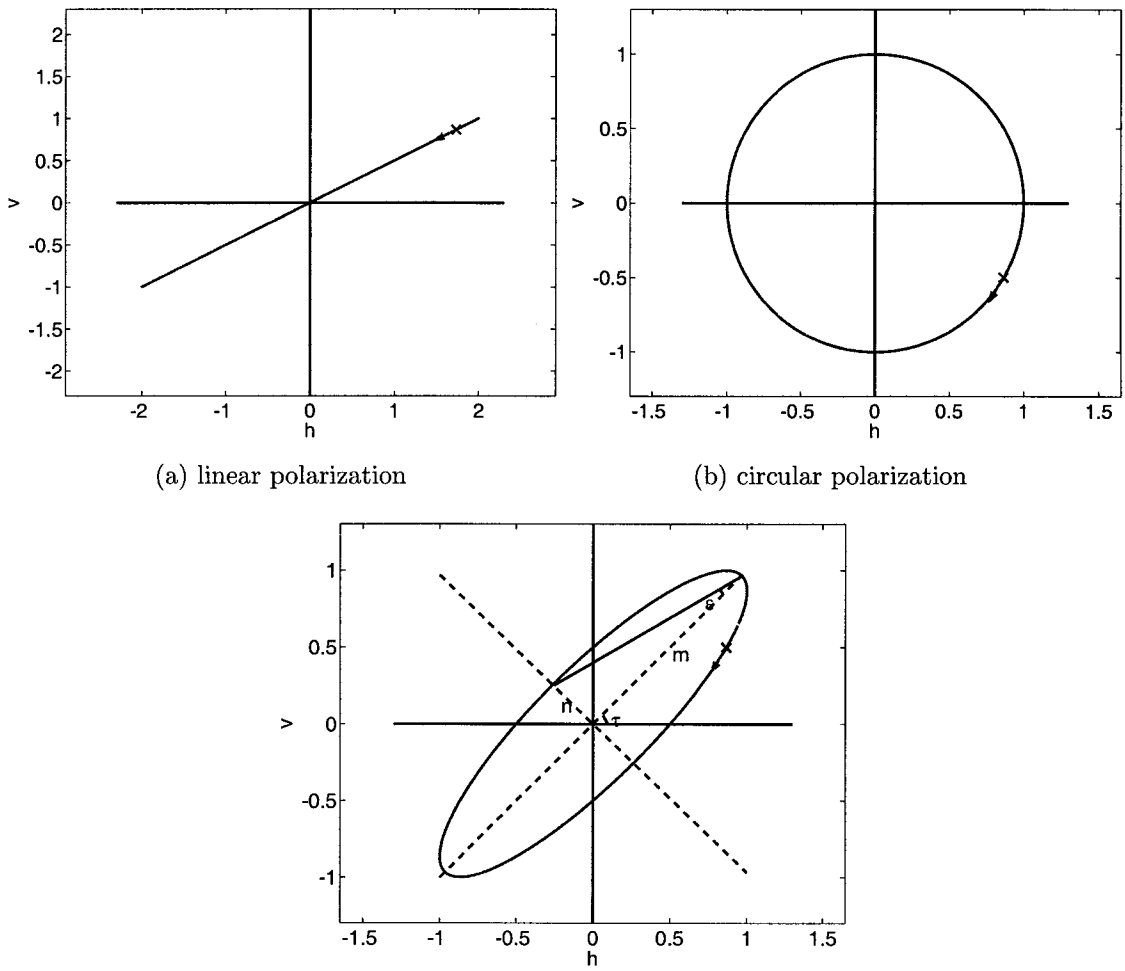

(a) linear polarization

(b) circular polarization

(c) elliptical polarization

Figure 3.1: The geometry of polarization traces on $(\hat{v}, \hat{h})$ plane: (a) E_h=$2e^{j30^o}$, E_v=e^{j30^o}; (b) E_h=e^{j30^o}, E_v=e^{j120^o}; (c) E_h=e^{j30^o}, E_v=e^{j60^o}. The marks '×' indicate the initial positions and the arrows show the evolving senses.

With simple arithmetic manipulation, the above equations can be combined into a general ellipse equation,

$$\frac{E_h^2(t)}{|E_h|^2} - 2\frac{E_h(t)E_v(t)}{|E_h||E_v|}\cos\delta + \frac{E_v^2(t)}{|E_v|^2} = \sin^2\delta,\ \delta = \theta_v - \theta_h \tag{3.9}$$

Again, the phase lag between v and h components (δ) decides the rotate sense of this ellipse trace. When $\delta > 0$, the trace evolves in clockwise; otherwise, it evolves in counter-clockwise. The initial position however depends on the both amplitudes and phases. Fig.3.1(c) illustrates the polarization ellipse for a plane wave with $|E_h| = |E_v|$, $\theta_h = 30^o$ and $\theta_v = 60^o$. Its characteristic parameters include the ellipticity angle ϵ, the tilt angle τ, and the positive semi-axes m and n (see the figure for their definitions).

In the transformed coordinate (ξ,η) rotated by τ, the polarization ellipse satisfies a normal equation

$$\frac{E_\xi^2(t)}{m^2} + \frac{E_\eta^2(t)}{n^2} = 1 \tag{3.10}$$

Comparing this normal equation with the general equation (3.9), we can derive the relationships between the geometry parameters and the electric parameters as follows [30]. The tilt angle τ satisfies

$$\tan 2\tau = \frac{2|E_h||E_v|}{|E_h|^2 - |E_v|^2}\cos\delta \quad -\frac{\pi}{2} < \tau < \frac{\pi}{2} \quad \text{if } |E_h| \neq |E_v| \tag{3.11a}$$

$$\tau = \pm\frac{\pi}{4} \quad \text{if } |E_h| = |E_v| \tag{3.11b}$$

The ellipticity angle ϵ is obtained from

$$\sin 2\epsilon = \frac{2|E_h||E_v|}{|E_h|^2 + |E_v|^2}\sin\delta \quad -\frac{\pi}{4} < \epsilon < \frac{\pi}{4} \tag{3.12}$$

When ϵ is known, it is straightforward to get the semi-axes as

$$m = \sqrt{|E_h|^2 + |E_v|^2}\cos\epsilon \tag{3.13a}$$

$$n = \sqrt{|E_h|^2 + |E_v|^2}\sin\epsilon \tag{3.13b}$$

Note that the sign of ϵ is same as that of δ (see (3.12)) and hence it corresponds to the rotation sense. For clockwise rotation, δ is positive and so is ϵ. Such wave is called right-hand elliptically polarized in consistent with the definition of circular polarization. Vice versa for the left hand elliptically polarized wave.

3.1.4 Complex Polarization Ratio

The analytical components E_h and E_v given in (3.1) fully determine the trace of the electric field on the polarization plane, i.e., its polarization state. For mathematical analysis, it would be convenient to define the complex polarization ration as,

$$\chi = \frac{E_v}{E_h} = \frac{|E_v|}{|E_h|} e^{j(\theta_v - \theta_h)} = \tan\alpha e^{j\delta} \tag{3.14}$$

Then the relations stated in (3.11) and (3.12) can be reformulated as:

$$\tan 2\tau = \tan 2\alpha \cos\delta = \frac{2\Re(\chi)}{1-|\chi|^2} \tag{3.15}$$

$$\sin 2\epsilon = \sin 2\alpha \sin\delta = \frac{2\Im(\chi)}{1+|\chi|^2} \tag{3.16}$$

and the complex polarization ratio can be written as

$$\chi = \frac{\tan\tau + j\tan\epsilon}{1 - j\tan\tau\tan\epsilon} \tag{3.17}$$

The unit vectors for the general polarization ellipse can also be expressed in term of $\hat{h}$ and $\hat{v}$. Applying the complex polarization ratio, we have

$$\begin{aligned} \mathbf{E} = E_0 e^{j\theta_h}\hat{e}_1 &= E_0 e^{j\theta_h}\left(\frac{|E_h|}{\sqrt{|E_h|^2+|E_v|^2}}\hat{h} + \frac{|E_v|e^{j\delta}}{\sqrt{|E_h|^2+|E_v|^2}}\hat{v}\right) \\ &= E_0 e^{j\theta_h}\frac{1}{\sqrt{1+|\chi|^2}}(\hat{h}+\chi\hat{v}) \end{aligned} \tag{3.18}$$

A pair of unit vectors $\hat{e}_1$ and $\hat{e}_2$, respectively corresponding to χ_1 and χ_2, are

$$\begin{bmatrix} \hat{e}_1 \\ \hat{e}_2 \end{bmatrix} = \begin{bmatrix} \frac{1}{\sqrt{1+|\chi_1|^2}} & \frac{\chi_1}{\sqrt{1+|\chi_1|^2}} \\ \frac{1}{\sqrt{1+|\chi_2|^2}} & \frac{\chi_2}{\sqrt{1+|\chi_2|^2}} \end{bmatrix} \begin{bmatrix} \hat{h} \\ \hat{v} \end{bmatrix} \tag{3.19}$$

Unlike the circular polarized unit vectors, $\hat{e}_1$ and $\hat{e}_2$ may not be orthogonal. To meet orthogonality, $\hat{e}_1 \cdot \hat{e}_2 = 0$, it can be shown that the sufficient and necessary condition is

$$\chi_1 \chi_2^* = -1 \tag{3.20}$$

The complex polarization ratio χ is able to depict all the polarization states (see Table 3.1), therefore as we will see, provides convenience in the analysis hereafter.

Polarization State	Polarization Ratio	Tilt Angle	Elliptic Angle
Linear	real	$[-90^o, 90^o]$	0^o
Circular	$\pm j$	-	$\pm 45^o$
Elliptic	complex	$[-90^o, 90^o]$	$(-45^o, 45^o), \neq 0$

Table 3.1: Summary of Polarization State

3.2 Basis Transformation

In the previous section, the polarization state of a plane wave was introduced using its real signal representation. A general description of the polarization state is the polarization ellipse, and the parameters of the ellipse can be expressed by the complex polarization ratio and vice versa. In this section, the general transformation between these different polarization states will be formulated.

Considering phases, it would be convenient to express the polarization plane as a complex vector space $\mathbb{C}^2$. Both the incident electric field and the scattered electric field are complex vectors in this space, i.e., $\mathbf{E_i}, \mathbf{E_s} \in \mathbb{C}^2$, while the role of scattering matrix $\mathbf{S}$ is building a linear map such that $\mathbf{E_s} = \mathbf{S}\mathbf{E_i}$. The representation of the vectors and the map $\mathbf{S}$ is dependent on the basis utilized for the space. In the previous analysis it is implied that the linear polarization basis is defined by unit vectors $\hat{h}$ and $\hat{v}$.

In the general case, supposing the incident field is represented on basis B while the scattering field on basis B', we can describe the same underlying map of

backscattering by

$$\mathbf{S}_{B,B'} = \mathbf{T}\mathbf{S}_L\mathbf{Q} \text{ where } \mathbf{T} = \mathbf{Rep}_{L,B'}, \mathbf{Q} = \mathbf{Rep}_{B,L} \tag{3.21}$$

where the matrix $\mathbf{Rep}_{B,L}$ stands for the identity transformation from basis B to L, and $\mathbf{S}_L$ represents the scattering matrix in the linear H/V basis. The diagram in Fig.3.2 sketches this relation. Note that when the same basis is used for both incident and scattering fields, $\mathbf{Q} = \mathbf{T}^{-1}$. Furthermore, if $\mathbf{T}$ is a unitary matrix, the vector length and the relative angle between vectors will be preserved.

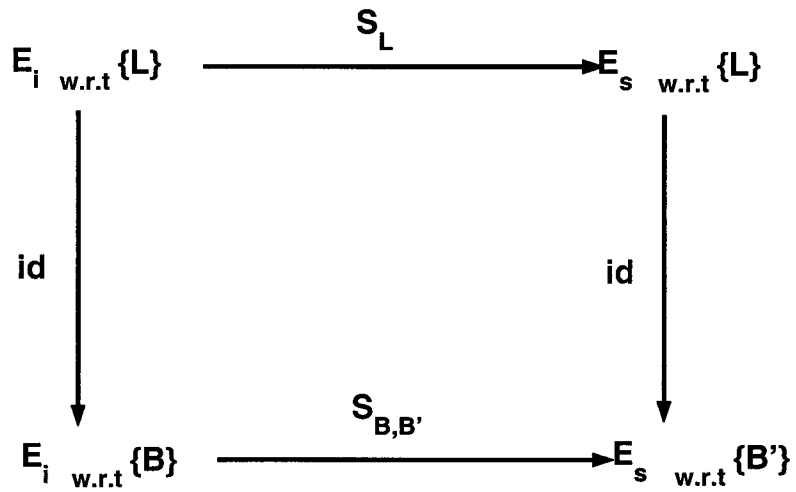

Figure 3.2: The diagram of basis transformation on a linear map

The circular polarization basis is another popular implementation in radar polarimetry. Its orthogonal basis is composed of RHC polarized unit vector $\hat{e}_r$ and LHC polarized one $\hat{e}_l$, as given in (3.7). It is straightforward to get the identity transformation from circular basis to linear basis as

$$\mathbf{Rep}_{C,L} = \frac{1}{\sqrt{2}} \begin{bmatrix} 1 & 1 \\ j & -j \end{bmatrix} \tag{3.22}$$

where subscript C denotes the circular polarization basis. It is easy to prove this matrix describes a unitary basis transformation. In backscattering convention, we

can get the circular scatter matrix based on (3.21) as

$$\begin{aligned}\mathbf{S}_C &= \begin{bmatrix} 0 & 1 \\ 1 & 0 \end{bmatrix} \mathbf{Rep}_{C,L}^{-1} \mathbf{S}_L \mathbf{Rep}_{C,L} \\ &= \mathbf{Rep}_{C,L}^{T} \mathbf{S}_L \mathbf{Rep}_{C,L} \end{aligned} \tag{3.23}$$

It is apparent that $\mathbf{S}_C$ is still a symmetric matrix and the concept of feature vector is applicable. After expanding $\mathbf{S}_C$ and extracting the feature vector, we have such relations

$$\mathbf{\Omega}_C = \mathbf{T}\mathbf{\Omega}_L \tag{3.24}$$

$$\mathbf{\Sigma}_C = \mathbf{T}\mathbf{\Sigma}_L\mathbf{T}^H \tag{3.25}$$

with the covariance transformation matrix being

$$\mathbf{T} = \frac{1}{2}\begin{bmatrix} 1 & j\sqrt{2} & -1 \\ \sqrt{2} & 0 & \sqrt{2} \\ 1 & -j\sqrt{2} & -1 \end{bmatrix}$$

It is also convenient to derive the transform from linear to general elliptic basis. Let $\chi_1 = \chi$, then, with (3.20) in mind, the pair of orthogonal elliptic unit vectors becomes

$$\begin{bmatrix} \hat{e}_1 \\ \hat{e}_2 \end{bmatrix} = \frac{1}{\sqrt{1+\chi\chi^*}} \begin{bmatrix} 1 & \chi \\ |\chi| & -\chi/|\chi| \end{bmatrix} \begin{bmatrix} \hat{h} \\ \hat{v} \end{bmatrix} \tag{3.26}$$

As expected, the matrix in (3.26) also describes a unitary transformation. The identity transformation matrix from elliptic basis to the linear H/V basis is

$$\mathbf{Rep}_{E,L} = \frac{1}{\sqrt{1+\chi\chi^*}} \begin{bmatrix} 1 & |\chi| \\ \chi & -\chi/|\chi| \end{bmatrix} \tag{3.27}$$

Substituting $\chi = j$ into the above unitary transformation will result in the circular transformation as represented by (3.22).

Before proceeding to the covariance matrix analysis, a few words are necessary concerning the absolute phase. An arbitrary phase shift δ could be applied to

the other channel, e.g. to the second column of $\mathbf{Rep}_{E,L}$, without affecting the orthogonality. The determinant of this transformation is

$$|\mathbf{Rep}_{E,L}| = -\chi e^{j\delta}/|\chi| \tag{3.28}$$

which implies that the correlations will experience such extra phase shift besides that caused by the phase of χ. Such ambiguity must be held in mind later.

Again, to obtain the transformed representation on scattering matrix, the convention about the rotation sense must be taken into account. In BSA convention, for the same polarization ellipse, the rotation sense is reversed for backscattering fields. Consulting the diagram in Fig.3.1(c), we notice that the reverse means $\tau_r = \tau_i$, $\epsilon_r = -\epsilon_i$, therefore we can write

$$\chi_r = \chi_i^* \tag{3.29}$$

and

$$\mathbf{Rep}'_{E,L} = \mathbf{Rep}^*_{E,L} \tag{3.30}$$

The new representation of the backscattering matrix in the elliptic basis becomes

$$\mathbf{S}_E = (\mathbf{Rep}'_{E,L})^{-1}\mathbf{S}_L\mathbf{Rep}_{E,L} = \mathbf{Rep}^T_{E,L}\mathbf{S}_L\mathbf{Rep}_{E,L} \tag{3.31}$$

Note the accordance between the result above and the bilinear voltage formula (see [18] for development of the bilinear voltage formula). Similarly, the covariance transformation matrix in the elliptic basis can be obtained as

$$\mathbf{T} = \frac{1}{1+\chi\chi^*}\begin{bmatrix} 1 & \sqrt{2}\chi & \chi^2 \\ \sqrt{2}|\chi| & \chi|\chi| - \chi/|\chi| & -\sqrt{2}\chi^2/|\chi| \\ |\chi|^2 & -\sqrt{2}\chi & \chi^2/|\chi|^2 \end{bmatrix} \tag{3.32}$$

which could be also shown to be a unitary transform matrix.

3.3 Effect of Canting Angle

During falling in steady air flow, a raindrop takes its equilibrium shape as an oblate spheroid which possesses a symmetric axis [9], as illustrated in Fig.3.3. In the absence of wind shear and turbulence, the symmetric axes of raindrops are expected to be vertical. Otherwise, the symmetric axes can be described by the orientation angle (θ_b, ϕ_b) in the physical coordinate (X, Y, Z). From the viewpoint of polarization, however, the angles relative to the polarization plane are more meaningful. Instead, we define the angle between the incidence direction and the symmetry axis of particle as ψ and the angle between vertical polarization and the projection of symmetry axis on the polarization plane as canting angle β.

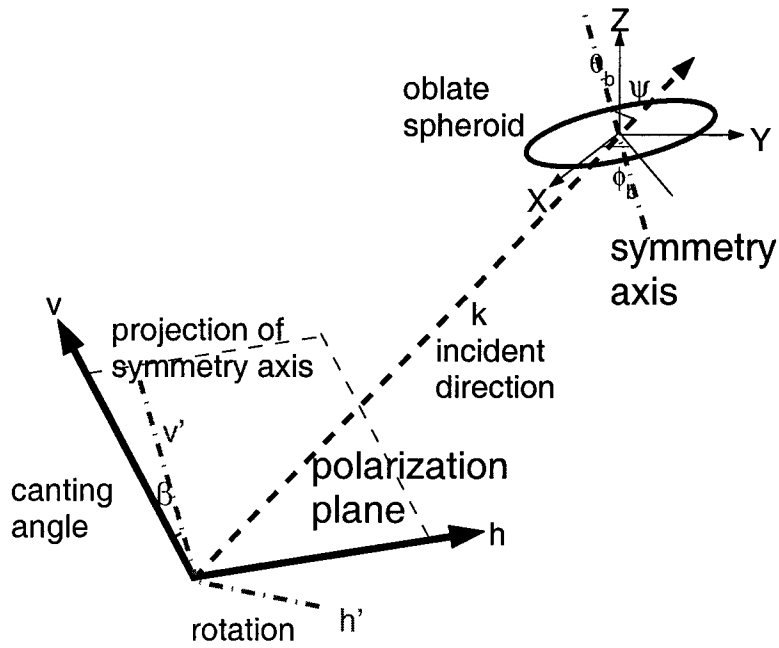

Figure 3.3: The geometry between an oblate spheroid scatter and the incident plane wave

With so defined β and ψ, the backscattering matrix can be written as [18]:

$$\mathbf{S} = \mathbf{R}(\beta) \begin{bmatrix} S_{11}(\psi) & 0 \\ 0 & S_{22}(\psi) \end{bmatrix} \mathbf{R}(-\beta) \tag{3.33}$$

where the characteristic variables S_{11} and S_{22} will be referred as variables in the "principal" plane hereafter. The rotation matrix, defined as

$$\mathbf{R}(\beta) = \begin{bmatrix} \cos\beta & \sin\beta \\ -\sin\beta & \cos\beta \end{bmatrix} \tag{3.34}$$

is a unitary matrix: $\mathbf{R}(-\beta) = \mathbf{R}^{-1} = \mathbf{R}^T$. Therefore, the canting angle acts the role of rotating the polarization basis from the principal plane by β (see (h', v') in Fig.3.3). For deterministic targets, the scattering matrix is diagonal when $\beta = 0$. In practice, however, the random nature of precipitation medium needs to be considered. Applying (3.34) to the scattering matrix, we can obtain the covariance transform matrix

$$\mathbf{T}(\beta) = \begin{bmatrix} \cos^2\beta & \sqrt{2}\sin\beta\cos\beta & \sin^2\beta \\ -\sqrt{2}\sin\beta\cos\beta & \cos^2\beta - \sin^2\beta & \sqrt{2}\sin\beta\cos\beta \\ \sin^2\beta & -\sqrt{2}\sin\beta\cos\beta & \cos^2\beta \end{bmatrix} \tag{3.35}$$

By straightforward but tedious algebra, we can obtain all the elements of the covariance matrix under the linear H/V polarization basis as:

$$Z_{hh} = \langle |S_{11}|^2 \cos^4\beta + |S_{22}|^2 \sin^4\beta + 2\Re(S_{11}S_{22}^*)\cos^2\beta\sin^2\beta \rangle \tag{3.36a}$$

$$Z_{vv} = \langle |S_{11}|^2 \sin^4\beta + |S_{22}|^2 \cos^4\beta + 2\Re(S_{11}S_{22}^*)\cos^2\beta\sin^2\beta \rangle \tag{3.36b}$$

$$Z_{vh} = \langle (|S_{11}|^2 + |S_{22}|^2 - 2\Re(S_{11}S_{22}^*))\sin^2\beta\cos^2\beta \rangle \tag{3.36c}$$

$$R_{hv} = \langle |S_{11}|^2 \sin^2\beta\cos^2\beta + |S_{22}|^2 \sin^2\beta\cos^2\beta + S_{11}^*S_{22}\sin^4\beta + S_{11}S_{22}^*\cos^4\beta \rangle \tag{3.36d}$$

$$R_{xh} = \langle (|S_{22}|^2 - S_{11}^*S_{22})\sin^3\beta\cos\beta + (S_{11}S_{22}^* - |S_{11}|^2)\sin\beta\cos^3\beta \rangle \tag{3.36e}$$

$$R_{xv} = \langle (S_{11}S_{22}^* - |S_{11}|^2)\sin^3\beta\cos\beta + (|S_{22}|^2 - S_{11}^*S_{22})\sin\beta\cos^3\beta \rangle \tag{3.36f}$$

It is of great interest to estimate the principal variables $\langle |S_{11}|^2 \rangle$, $\langle |S_{22}|^2 \rangle$, and $\langle S_{11}S_{22}^* \rangle$ since they directly reflect the shape and size information of hydrometeor particles. Apparently (3.36) tells that we need to separate out the information on orientation from that on "intrinsic" values in the principal plane.

In order to make the problem tangible, fundamental assumptions will be made here and used throughout this work:

1. The orientation distribution is independent of the shape distribution and size distribution (DSD);

2. The angle ψ and β can be treated separately;

3. The precipitation medium exhibits "mirror" reflection symmetry about a plane.

As a result, the terms on β can be taken out and the pdf of β is symmetric. If $\beta_0 = \langle\beta\rangle$ and $\beta' = \beta - \beta_0$, the expectation over the angular terms follows

$$\langle \sin n\beta \rangle = \langle \cos n\beta' \rangle \sin n\beta_0 \tag{3.37a}$$

$$\langle \cos n\beta \rangle = \langle \cos n\beta' \rangle \cos n\beta_0 \tag{3.37b}$$

Then the effect of canting angle on covariance can be studied by two stages: the dispersion with zero mean, and the rotation by mean canting angle β_0. A quick review of (3.36) indicates: (1) The cross-polar power has its minima when $\beta_0 = 0$ and at the same time the co-to-cross correlations are zero; (2) The cross-polar power has its maxima when $\beta_0 = 45^o$ and at the same time co-polar powers are equal.

A simulation will vividly illustrate the effect of mean canting angle on the polarimetric covariance. The simulated covariance matrix in the linear H/V basis is

$$\Sigma_0 = \begin{bmatrix} 1 & 0 & 0.618e^{-j5^o} \\ 0 & 0.0036 & 0 \\ 0.618e^{j5^o} & 0 & 0.412 \end{bmatrix} \tag{3.38}$$

which corresponds to rain with the assumed model:

- Drop Size Distribution

  Exponential: $N(D) = N_0 \exp(-3.67D/D_0)$

  $N_0 = 8000mm^{-1}m^{-3}$

  $D_0 = 2.5mm$

- Orientation Distribution

  Fisher: $f(\theta_b, \phi_b) = \frac{\kappa \sin\theta_b}{4\pi \sinh(\kappa)} \exp\{\kappa[\cos\bar{\theta}_b \cos\theta_b + \sin\bar{\theta}_b \sin\theta_b \cos(\phi - \bar{\phi})]\}$

  $\bar{\theta}_b = \bar{\phi}_b = 0^o$

  $\kappa = 100$

- Incidence Direction

  Horizontal Incidence: $\theta_i = 90^o$

The mean canting angle, which increases from 0^o up to 90^o, is applied to the intrinsic covariance matrix according to (3.33) and (3.35). Fig.3.4 illustrates the strong functional effect of β_0 on all the available radar variables. Especially, with β_0 increasing, Z_{DR} can change its sign; the cross-polar variables LDR, ρ_{xh} and ρ_{xv} can substantially increase as depolarization aggravates. In practice β_0 is likely to be between -10^o and 10^o, which may still make ρ_{xh} and ρ_{xv} to increase by more than 0.6.

Also, we can transform the covariance matrix under the linear basis to that under circular basis using (3.25). The covariance matrix in circular basis due to the effect of canting angle turns out to be

$$\mathbf{T}_C(\beta) = \begin{bmatrix} e^{-j2\beta} & j\sqrt{2}e^{-j2\beta} & -e^{-j2\beta} \\ \sqrt{2} & 0 & \sqrt{2} \\ e^{j2\beta} & -j\sqrt{2}e^{j2\beta} & -e^{j2\beta} \end{bmatrix} \tag{3.39}$$

which means that the canting angle introduces only phase shifts to the covariances. Referring to (3.37),

$$\langle e^{jn\beta} \rangle = \langle \cos n\beta \rangle e^{jn\beta_0} \tag{3.40}$$

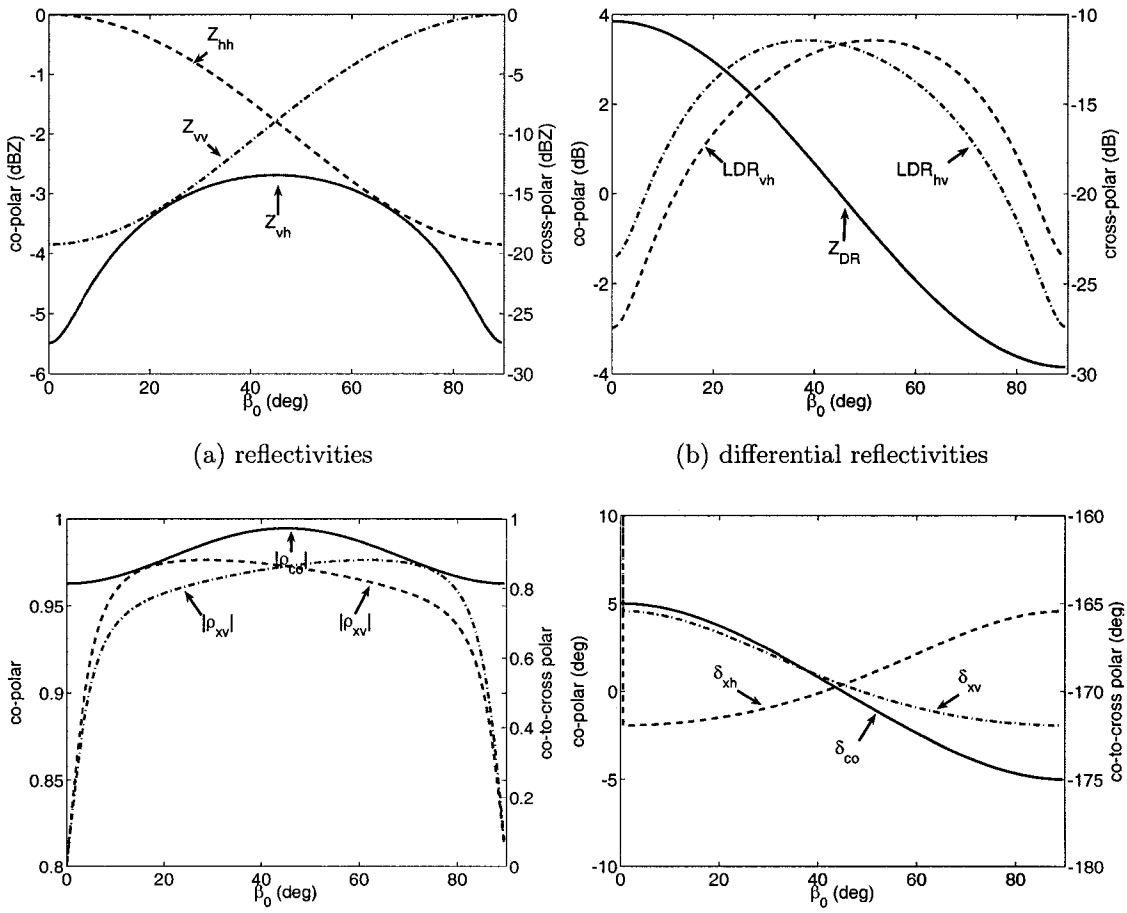

(a) reflectivities

(b) differential reflectivities

(c) correlation coefficients

(d) correlation phases

Figure 3.4: The radar variables in the linear H/V polarization basis under non-zero mean canting angle based on simulation

Then the covariance elements in the circular polarization basis can be written as follows:

$$Z_{rr} = Z_{ll} = \frac{1}{4}\langle|S_{11} - S_{22}|^2\rangle \tag{3.41a}$$

$$Z_{rl} = \frac{1}{4}\langle|S_{11} + S_{22}|^2\rangle \tag{3.41b}$$

$$R_{rl} = \frac{1}{4}\langle|S_{11} - S_{22}|^2 \cos 4\beta'\rangle e^{-j4\beta_0} \tag{3.41c}$$

$$R_{xr} = \frac{1}{4}\langle(S_{11} - S_{22})(S_{11} + S_{22})^* \cos 2\beta'\rangle e^{-j2\beta_0} \tag{3.41d}$$

$$R_{xl} = \frac{1}{4}\langle(S_{11} - S_{22})(S_{11} + S_{22})^* \cos 2\beta'\rangle e^{j2\beta_0} \tag{3.41e}$$

It is clear from (3.41) that only the correlation phases undergo proportional changes with the mean canting angle. We can take advantage of circular basis to extract the terms on canting angle.

3.3.1 Moment Estimation of Canting Angle in Circular Basis

In the circular polarization basis, the mean canting angle can be derived from the co-to-cross correlations R_{xr} and R_{xl} as

$$-4\beta_0 = \arg(R_{xr}) - \arg(R_{xl}) \tag{3.42}$$

or be retrieved directly from the co-polar correlation R_{rl}. Note that the co-polar channels in circular basis are "weak" and hence the estimation from co-to-cross correlations is generally preferred.

Hendry and McCormick [6] defined another orientation factor as

$$\rho_4 = \langle\cos 4\beta'\rangle = \frac{|R_{rl}|}{\sqrt{\langle|S_{rr}|^2\rangle\langle|S_{ll}|^2\rangle}} \tag{3.43}$$

which is a measure of the dispersion of the canting angle and inversely related to its standard deviation σ_β. For perfect alignment, ρ_4 equals to 1; for totally random orientation, it goes to 0. Assume the canting angle is Gaussian distributed variable, ρ_4 then asymptotically approaches a function [31]

$$\rho_4 = e^{-8\sigma_\beta^2} \tag{3.44}$$

by which we can obtain the standard deviation of canting angle from ρ_4.

Other radar variables defined in circular basis include the circular depolarization ratio

$$CDR = \frac{Z_{rr}}{Z_{rl}} = \frac{< |S_{11} - S_{22}|^2 >}{< |S_{11} + S_{22}|^2 >} \tag{3.45}$$

and the "apparent degree of orientation"

$$ORTT = \frac{|R_{xr}|}{\sqrt{Z_{rr} Z_{rl}}} = \frac{|\langle (S_{11} - S_{22})(S_{11} + S_{22})^* \rangle|}{\langle |S_{11} + S_{22}|^2 \rangle} \rho_2 \tag{3.46}$$

Note that CDR is only related to the shape distribution while $ORTT$ is a product of shape terms and a orientation term ρ_2 (defined as $\langle \cos(2\beta') \rangle$).

3.3.2 Moment Estimation of Canting Angle in Linear Basis

Basis transformation does not change the properties of a linear map on the vector space but only affects its representation. Since the estimate of the orientation factors could be obtained from the transformed circular polarimetric covariance matrix, it would be also possible to be obtained from the measurement in the linear basis directly.

Checking the linear polarimetric covariance elements listed in (3.36), we find those six independent equations to involve two real variables $\langle |S_{11}|^2 \rangle$, $\langle |S_{12}|^2 \rangle$, one complex correlation $\langle S_{11} S_{22}^* \rangle$, and different ordered moments of the canting angle β.

With the relations in (3.37), we have

$$R_{xh} + R_{xv} = \frac{\rho_2 \sin 2\beta_0}{2} (\langle |S_{22}|^2 - |S_{11}|^2 \rangle + j2I) \tag{3.47a}$$

$$R_{xh} - R_{xv} = -\frac{\rho_4 \sin 4\beta_0}{4} (\langle |S_{22}|^2 + |S_{11}|^2 \rangle - 2R) \tag{3.47b}$$

$$R_{hv} - Z_{hv} = R + jI\rho_2 \cos 2\beta_0 \tag{3.47c}$$

$$\text{where } R + jI = \langle S_{11} S_{22}^* \rangle,\ \rho_2 = \langle \cos 2\beta' \rangle$$

An important observation could be made: the imaginary part of the co-to-cross correlation R_{xh} and R_{xv} should be equal if the scattering medium exhibits mirror reflection symmetry and the covariance matrix only undergoes rotation by the mean canting angle.

Furthermore, the differential reflectivity between co-polar channels can be written as

$$Z_{hh} - Z_{vv} = -\rho_2 \cos 2\beta_0 \langle |S_{22}|^2 - |S_{11}|^2 \rangle \tag{3.48}$$

and the cross-polar reflectivity as

$$Z_{vh} = \frac{1 - \rho_4 \cos 4\beta_0}{8} (\langle |S_{11}|^2 + |S_{22}|^2 \rangle - 2R) \tag{3.49}$$

The total power is invariant under this unitary transformation:

$$tr = \langle |S_{22}|^2 + |S_{11}|^2 \rangle \tag{3.50}$$

All the unknowns can be solved through (3.47) to (3.50). The mean canting angle can be obtained by

$$\tan 2\beta_0 = -\frac{2\Re(R_{xh} + R_{xv})}{Z_{hh} - Z_{vv}} \tag{3.51}$$

or

$$\tan 2\beta_0 = \frac{\Im(R_{xh} + R_{xv})}{\Im(R_{hv} - Z_{hv})} \tag{3.52}$$

Note that (3.51) is immune to Doppler effect since it does not relate to the co-polar correlation while (3.52) would be generally immune to noise since only imaginary parts are used for the estimation. In the following work, the estimation by (3.51) is preferable than that by (3.52). When both the denominator and numerator of (3.51) are zero, two situations may exist: spherical particles ($\langle |S_{11}|^2 \rangle = \langle |S_{22}|^2 \rangle$) or isotropic orientation ($\rho_2 = 0$). The mean canting angle is undefined for both cases

and hence assumed to be 0. As for ρ_4, it will be assigned 1 for the former case when LDR is very small. A general estimate of ρ_4 is available from

$$\frac{1-\rho_4\cos 4\beta_0}{8} = \frac{Z_{vh}}{Z_{hh}+Z_{vv}+4Z_{vh}-2\Re(R_{hv})} \tag{3.53}$$

or

$$\frac{1-\rho_4\cos 4\beta_0}{2\rho_4\sin 4\beta_0} = -\frac{Z_{vh}}{R_{xh}-R_{xv}} \tag{3.54}$$

Once ρ_4 is estimated, ρ_2 can be computed from ρ_4 based on $\rho_4 = \rho_2^4$ for narrow Gaussian distributions [6]. After the orientation factors β_0 and ρ_2 are determined, by substituting them back to (3.48) and combining (3.50), the principal variables $\langle|S_{11}|^2\rangle$ and $\langle|S_{22}|^2$ can be retrieved. And finally, the whole covariance matrix is solved with the principal correlation $\langle S_{11}S_{22}^*\rangle$ also available.

The relation between minimum and maximum cross-polar power that connects through a linear basis rotation by 45^o also yields an estimate of ρ_4 as: [6]

$$\frac{1+\rho_4}{1-\rho_4} = \frac{\max Z_{vh}}{\min Z_{vh}} \tag{3.55}$$

Based on such relation, a ρ_4 method was proposed by Huang [32] to estimate the dispersion of canting angle with β_0 assumed to be zero. The estimate of ρ_4 was derived as,

$$\rho_4 = \frac{Z_{hh}+Z_{vv}-4Z_{vh}-2\Re(R_{hv})}{Z_{hh}+Z_{vv}+4Z_{vh}-2\Re(R_{hv})} \tag{3.56}$$

The estimate of ρ_4 by (3.53) is consistent with Huang's estimate since the right hand of (3.56) is exactly same as the value $\rho_4\cos 4\beta_0$ from (3.53). Apparently, Huang's method always give lower estimation for ρ_4 considering small but non-zero β_0 in practice.

3.3.3 Moment Estimation of Canting Angle by Polarization Optimization

The unitary transform space on $\mathbb{C}^2$ is closed and bounded over the tilt angle τ and ellipticity angle ϵ. Minima and maxima exist for the power returns in the whole transform space. The extremum of the power returns depends only on the backscattering medium. The polarization state to obtain such extremum is referred as characteristic polarization states. For deterministic scatters, characteristic polarizations have been studied extensively in [33], [34], [35], [36]. McCormick [37] and Tragl [7] extended the theory to incoherent case for reciprocal random targets. The optimized polarization for incoherent scattering will be reviewed and generalized to arbitrary transformation in this section.

First, the differentiation regarding complex variable is defined to facilitate the derivation. Suppose a real function $f(x)$ depends on complex variable x, then the extrema of $f(x)$ exist when x meets both of the real equations:

$$\frac{\partial f(x)}{\partial u} = 0 \quad \frac{\partial f(x)}{\partial v} = 0 \quad \text{where } x = u + jv \tag{3.57}$$

This set of real equations can be combined to one complex equation by defining

$$\frac{\partial f(x)}{\partial x^*} = \frac{1}{2}\left(\frac{\partial f(x)}{\partial u} + j\frac{\partial f(x)}{\partial v}\right) = 0 \tag{3.58}$$

Note that with this definition, it is easy to prove such properties as

$$\frac{\partial x}{\partial x^*} = 0 \tag{3.59a}$$

$$\frac{\partial x^*}{\partial x^*} = 1 \tag{3.59b}$$

$$\frac{\partial |x|}{\partial x^*} = \frac{1}{2}\frac{x}{|x|} \tag{3.59c}$$

Under the change of polarization basis as described by (3.32), the covariance matrix of the backscattering targets is composed of functions of the polarization ratio χ:

$$\Sigma(\chi) = \mathbf{T}(\chi)\Sigma_0\mathbf{T}^H(\chi) \tag{3.60}$$

Since $\mathbf{T}(\chi)$ is unitary, the partial differentiation of the covariance matrix regarding to χ is given by

$$\frac{\partial \mathbf{\Sigma}(\chi)}{\partial \chi^*} = \frac{\partial \mathbf{T}(\chi)}{\partial \chi^*}\mathbf{\Sigma}_0\mathbf{T}^H(\chi) + \mathbf{T}(\chi)\mathbf{\Sigma}_0\frac{\partial \mathbf{T}^H(\chi)}{\partial \chi^*} \tag{3.61a}$$

$$= \frac{\partial \mathbf{T}(\chi)}{\partial \chi^*}\mathbf{T}^H(\chi)\mathbf{\Sigma}(\chi) + \mathbf{\Sigma}(\chi)\mathbf{T}(\chi)\frac{\partial \mathbf{T}^H(\chi)}{\partial \chi^*} \tag{3.61b}$$

Applying partial differentiation to the unitary relation $\mathbf{T}(\chi)\mathbf{T}^H(\chi) = \mathbf{I}$, we have

$$\frac{\partial \mathbf{T}(\chi)}{\partial \chi^*}\mathbf{T}^H(\chi) + \mathbf{T}(\chi)\frac{\partial \mathbf{T}^H(\chi)}{\partial \chi^*} = 0 \tag{3.62}$$

Therefore, (3.61) can be rewriten as

$$\frac{\partial \mathbf{\Sigma}(\chi)}{\partial \chi^*} = \mathbf{T}_D(\chi)\mathbf{\Sigma}(\chi) - \mathbf{\Sigma}(\chi)\mathbf{T}_D(\chi) \tag{3.63}$$

where

$$\mathbf{T}_D(\chi) = \frac{\partial \mathbf{T}(\chi)}{\partial \chi^*}\mathbf{T}^H(\chi) \tag{3.64}$$

It is straightforward to derive

$$\mathbf{T}_D(\chi) = -\frac{\chi}{1+|\chi|^2}\mathbf{I} + \frac{1}{1+|\chi|^2}\begin{bmatrix} 0 & 0 & 0 \\ \sqrt{2}\frac{\chi}{|\chi|} & \frac{1}{2}\frac{\chi}{|\chi|^2}(|\chi|^2-1) & 0 \\ 0 & \sqrt{2}\frac{\chi}{|\chi|} & \frac{\chi}{|\chi|^2}(|\chi|^2-1) \end{bmatrix} \tag{3.65}$$

Finally, applying $\mathbf{T}_D$ to (3.61) yields

$$\frac{\partial \Sigma(\chi)}{\partial \chi^*} = \frac{1}{1+|\chi|^2}\begin{bmatrix} -2\frac{\chi}{|\chi|}R^a_{cx}(\chi) & - & - \\ - & 2\frac{\chi}{|\chi|}[R^a_{cx}(\chi) - R^{b*}_{cx}(\chi)] & - \\ - & - & 2\frac{\chi}{|\chi|}R^{b*}_{cx}(\chi) \end{bmatrix} \tag{3.66}$$

where the superscripts 'a' and 'b' refers to the pair of orthogonal polarization states for the general elliptic polarization basis.

The sufficient and necessary conditions for the extrema in power terms hence are

$$Z_{co}^{a} : R_{cx}^{a}(\chi) = 0 \tag{3.67a}$$

$$Z_{co}^{b} : R_{cx}^{b}(\chi) = 0 \tag{3.67b}$$

$$Z_{cx} : R_{cx}^{a}(\chi) = R_{cx}^{b*}(\chi) \tag{3.67c}$$

which may correspond to their minima, maxima, or saddle points. When the mean canting angle β_0 is zero, $R_{xh} = R_{xv} = 0$, which satisfies all the conditions. On the other hand, the cross-polar power reaches its minima if only real value rotation is related, i.e., if $\epsilon = 0$. This statement also holds for the transformation if $\tau = 0$. Therefore, the cross-polar power exhibits its minimum value in the whole space $\{\chi\}$ if and only if $\epsilon = 0$ and $\tau = 0$, where the polarization basis coincides with the characteristic polarizations of the precipitation medium.

Thus, we can determine the characteristic polarization that locates at the minimal cross-polar power. Such optimization can be solved by eigenvalue problem [38]. Regarding Z_{cx}, the matrix form is equivalent to the quadratic equation

$$Z_{cx}(\chi) = \frac{1}{2}\vec{z}(\chi)\Sigma_0\vec{z}^{H}(\chi) \tag{3.68}$$

which seeks to be minimized under the constraint

$$\vec{z}(\chi) = \frac{1}{1+|\chi|^2}\left[\begin{array}{cc} \sqrt{2}|\chi| & \chi|\chi| - \chi/|\chi| \end{array}\right.\left.\begin{array}{c} -\sqrt{2}\chi^2/|\chi|^2 \end{array}\right] \tag{3.69a}$$

$$= \frac{1}{1+|\chi|^2}\frac{\chi}{|\chi|}\left[\begin{array}{cc} \sqrt{2}\chi^* & |\chi|^2 - 1 \end{array}\right.\left.\begin{array}{c} -\sqrt{2}\chi \end{array}\right] \tag{3.69b}$$

Note that the phase term $\chi/|\chi|$ in the above equation does not matter in the solution. Discarding that phase, the constrained optimization can be transformed to an unconstrained problem

$$Z_{cx}(\chi) = \frac{1}{2}\vec{v}(\chi)\Sigma_0'\vec{v}^{H}(\chi) \tag{3.70}$$

where

$$\vec{v}(\chi) = \frac{1}{1+|\chi|^2}\left[\begin{array}{ccc} 1-|\chi|^2 & 2\Re\chi & 2\Im\chi \end{array}\right] \tag{3.71}$$

and

$$\boldsymbol{\Sigma}_0' = \mathbf{Q}\boldsymbol{\Sigma}_0\mathbf{Q}^H \tag{3.72a}$$

$$\mathbf{Q} = \frac{1}{\sqrt{2}}\left[\begin{array}{ccc} 0 & -\sqrt{2} & 0 \\ 1 & 0 & -1 \\ -j & 0 & -j \end{array}\right] \tag{3.72b}$$

The eigenvalues of $\boldsymbol{\Sigma}_0'$ respectively correspond to the maxima, saddle, and minima of the quadratic equation $Z_{cx}(\chi)$.

Once χ of the characteristic polarization is known, the ellipse state τ and ϵ can be inversely solved. However, recall that the arbitrary phase noted in (3.28), it is impossible to recover the exact polarization state χ, unless the phase is known apriori. When only rotation of the linear polarization basis by β_0 is involved and no phase offset exists between H and V channel, χ is known as a real variable and τ is available, which gives the estimation for β_0.

Moreover, we would seek to employ the polarization invariant characteristic parameters. Rotating by 45^o from the H/V polarization basis, we have

$$R_{xh}' = R_{xv}' = \frac{1}{8}(\langle|S_{22}|^2 - |S_{11}|^2\rangle - j2\Im\langle S_{11}S_{22}^*\rangle)$$

It satisfies the condition for extrema of the cross-polar power if $\langle S_{11}S_{22}^*\rangle$ approximates 0, which is usually valid for S-band radar measurement. This extreme value represents the saddle point of the cross-polar power in the whole space $\{\chi\}$. With these two polarization invariant extreme values, a robust estimation of ρ_4 is available based on (3.55). A little bias is sacrificed for the robustness of this estimator.

3.3.4 Comparisons

The merit of the direct solution is its simplicity and possibly its insensitivity to the Doppler spectrum. Moreover, if the estimation of β_0 and ρ_4 is sufficiently accurate, the "principal" polarimetric variables $\langle|S_{11}|^2\rangle$, $\langle|S_{22}|^2\rangle$ and $\langle S_{11}S_{22}^*\rangle$, which contains the intrinsic shape factors, can be solved from a set of equations. However, the algorithm is sensitive to phase errors.

As for the method using the circular polarized covariance matrix, some extra computation is incurred but not outstanding since the transformation to the circular basis is very simple as shown by the expanded formula from (3.25):

$$Z_{rr} = Z_{hh} + Z_{vv} + 4Z_{hv} - 2\Re(R_{hv}) + 4\Im(R_{xh} - R_{xv}) \tag{3.73a}$$

$$Z_{ll} = Z_{hh} + Z_{vv} + 4Z_{hv} - 2\Re(R_{hv}) - 4\Im(R_{xh} - R_{xv}) \tag{3.73b}$$

$$Z_{rl} = Z_{hh} + Z_{vv} + 2\Re(R_{hv}) \tag{3.73c}$$

$$R_{rl} = Z_{hh} + Z_{vv} - 4Z_{hv} - 2\Re(R_{hv}) + j4\Re(R_{xh} - R_{xv}) \tag{3.73d}$$

$$R_{xr} = Z_{hh} - Z_{vv} + j2\Im(R_{hv}) + j2(R_{xh}^* + R_{xv}^*) \tag{3.73e}$$

$$R_{xl} = Z_{hh} - Z_{vv} + j2\Im(R_{hv}) - j2(R_{xh}^* + R_{xv}^*) \tag{3.73f}$$

We see the similarity compared to the direct solution. Note that the implication discussed in direct approach, $\Im(R_{xh}) = \Im(R_{xv})$, means $Z_{rr} = Z_{ll}$ in the circular basis. Otherwise, the co-polar powers in the circular basis will not be equal and the estimation of ρ_4 will fail. Since the correlations exist in all the circular covariance terms, the circular polarimetric variable as well as the estimations will be corrupted by phase errors.

The optimization approach requires more computation, but it also holds great similarity compared to the direct solution as we can see from the expansion of (3.72):

$$\Sigma_0' = \begin{bmatrix} 2Z_{hv} & \Re(R_{xv} - R_{xh}) & -\Im(R_{xv} + R_{xh}) \\ - & \frac{1}{2}\Re(Z_{hh} + Z_{vv} - 2R_{hv}) & -\Im(R_{hv}) \\ - & - & \frac{1}{2}\Re(Z_{hh} + Z_{vv} + 2R_{hv}) \end{bmatrix} \tag{3.74}$$

The merit of this method is its ability in the whole unitary transform space to determine the cross-polar power in the characteristic polarization states given "distorted" radar measurement, which leads to a robust estimator of ρ_4 valid in all orthogonal polarization basis. The capability to obtain unbiased estimation of β_0 is still limited if phase errors exist due to the ambiguity in determining the polarization state χ.

Concerning the ambiguity, to make the transform invertible, we may force the determinant of the transformation matrix (see 3.28) to equal 1, which in turn demands an extra phase offset $\pi - \arg\chi$ introduced to V channel. Then the transformation matrix becomes

$$\mathbf{Rep}_{E,L} = \begin{bmatrix} 1 & -\chi^* \\ \chi & 1 \end{bmatrix} \tag{3.75}$$

This form of transformation, restoring the rotation form in (3.34) when $\epsilon = 0$, was also used by Tragl [7], [38]. With this transformation, we can transform the simulated covariance matrix to other basis in the complete transform space (τ, ϵ). The values of polarimetric variables in new bases are shown in Fig.3.5 as functions of (τ, ϵ). From panel (c), the minimum of cross-polar power is apparent at the polarization state represented by $(0^o, 0^o)$, where the co-to-cross correlation coefficients both are zero (see panels (d) and (e)); and the saddle points are very close to the polarization states represented by $(\pm 45^o, 0^0)$, where the difference of two co-to-cross correlation coefficients is close to 0 (see panel (f)). The cross-polar power increases along with the ellipticity angle.

Fig.3.6 illustrates the estimation of the tilt angle in space $\{\chi\}$. The estimate shown in panel (a) is obtained from the circular covariance matrix, falling inside $\pm 45^o$ as implied by (3.42); that shown in panel (b) is obtained by the direct solution, valid between $\pm 90^o$ as implied by (3.47) and (3.48); that shown in panel (c) is obtained by polarization optimization, falling inside $\pm 45^o$ as implied by

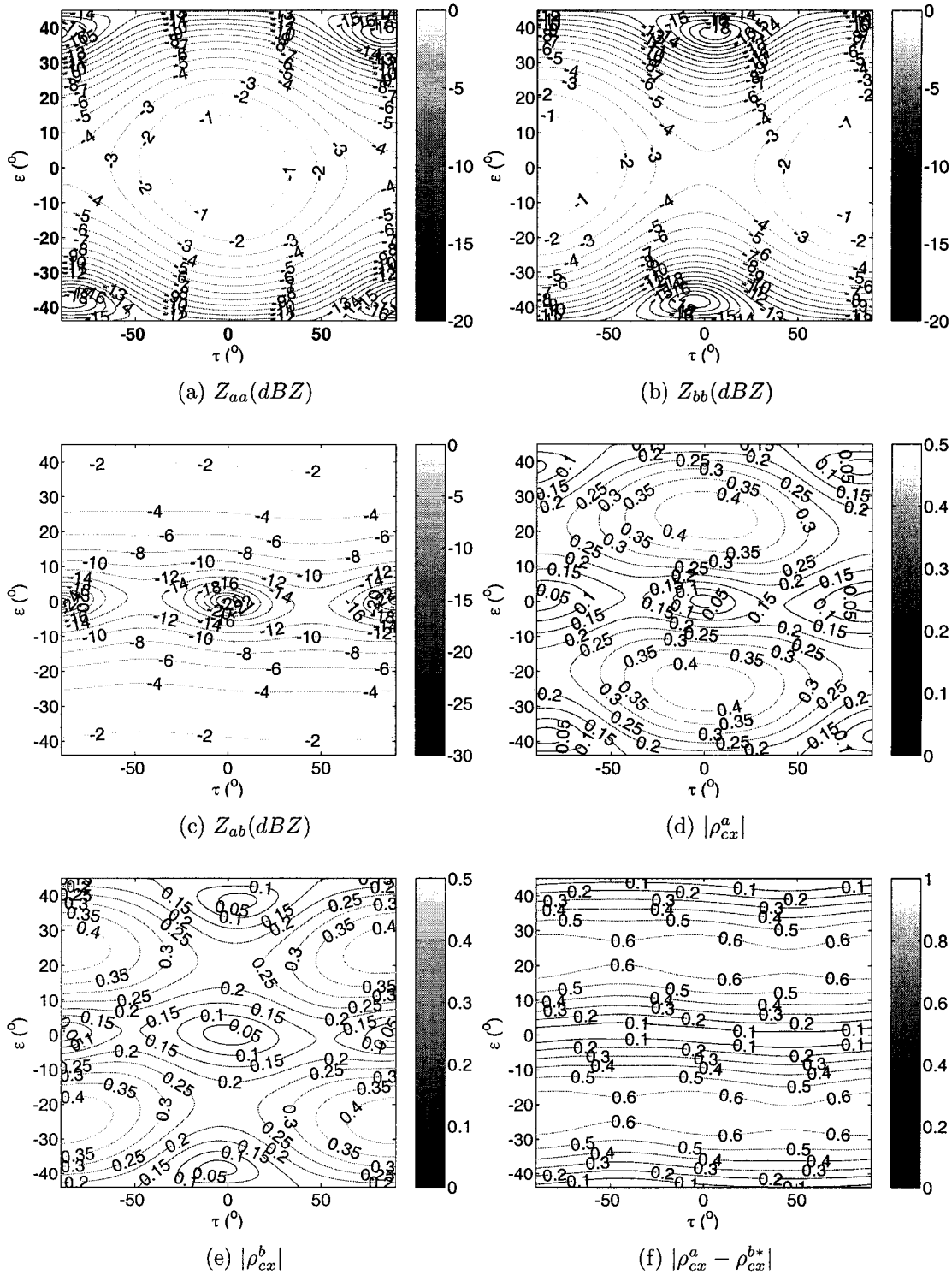

(a) $Z_{aa}(dBZ)$ (b) $Z_{bb}(dBZ)$

(c) $Z_{ab}(dBZ)$ (d) $|\rho_{cx}^{a}|$

(e) $|\rho_{cx}^{b}|$ (f) $|\rho_{cx}^{a} - \rho_{cx}^{b*}|$

Figure 3.5: The dependencies of polarimetric variables on the polarization bases. The X-axis refers to the tilt angle of polarization ellipse in degree while the Y-axis refers to ellipticity angle in degree. The reflectivities were normalized to Z_{hh}.

(3.15). All the three methods could recover the tilt angle, or the mean canting angle, when $\epsilon = 0$. The estimator by direct solution has no ambiguity. When ellipticity angle increases, the estimation by circular covariance matrix is invalid.

Fig.3.7 presents the estimation of ρ_4. The panel (a) shows the estimate from circular covariance matrix by (3.43); (b) shows that from linear covariance matrix by direct solution (3.53); while (c) shows that from optimized polarization by (3.55). When $\epsilon = 0$, the estimated ρ_4 by the three methods are: (a) 0.9234; (b) 0.9234; (c) 0.9214. Based on the models, the former two results would be rather precise, while the result by optimization would have small bias. That is true compared to the theoretical value of ρ_4, derived as 0.9228 using numerical integration over the orientation distribution. However, the former two estimators lead to incorrect solutions as soon as $\epsilon \neq 0$, while the estimator by optimization gives same decent result throughout the whole space $\{\chi\}$.

In summary, considering the basis transformation due to canting angle, accurate estimation of the orientation factors can be obtained by all the three methods developed on above. In presence of phase errors on the measurement, the estimation may have significant biases. However, applying the concept of approximate saddle of the cross-polar power, the polarization optimization gives a robust estimator of ρ_4.

3.4 Effect of Propagation

For a homogeneous propagation path, the propagation matrix $\mathbf{P}$ should be taken into consideration because

$$\begin{bmatrix} E_h(r) \\ E_v(r) \end{bmatrix} = \mathbf{P}(r) \begin{bmatrix} E_h(0) \\ E_v(0) \end{bmatrix} \tag{3.76}$$

Hence the radar equation needs to be modified as follows [18]:

$$\begin{bmatrix} V_h \\ V_v \end{bmatrix} = \frac{\lambda G}{4\pi r^2} \mathbf{PSP} \begin{bmatrix} M_h \\ M_v \end{bmatrix} \tag{3.77}$$

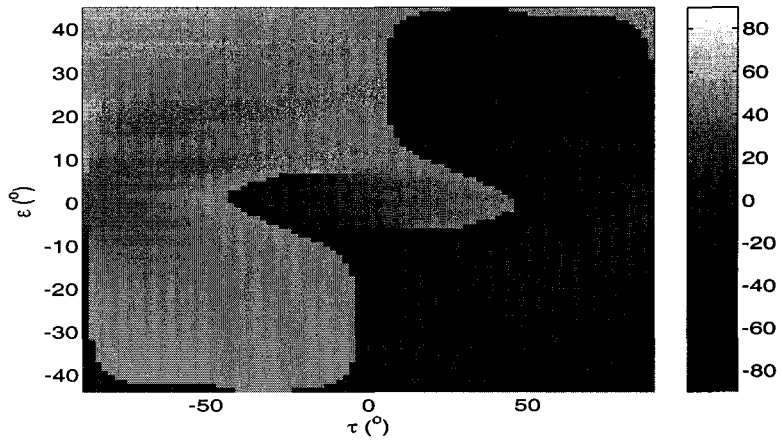

(a) Estimation by circular covariance matrix

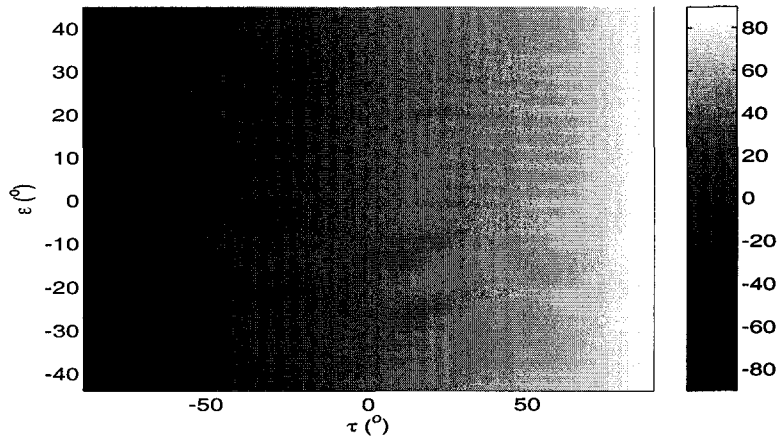

(b) Estimation by direct solution

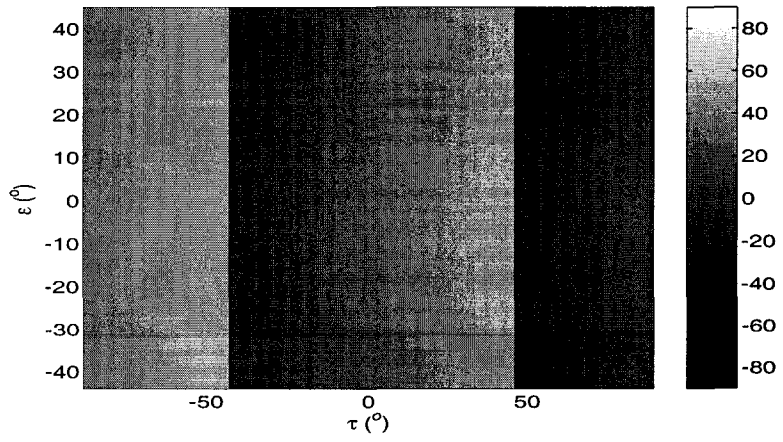

(c) Estimation by polarization optimization

Figure 3.6: The estimate of τ (β_0) from the covariance matrices under different polarization bases

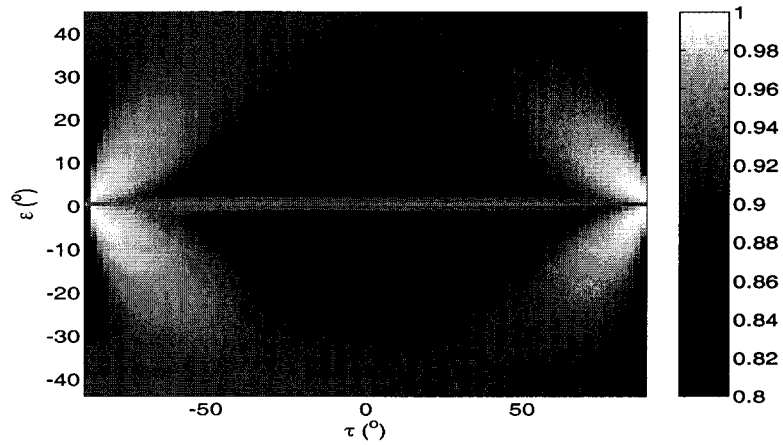

(a) Estimation by circular covariance matrix

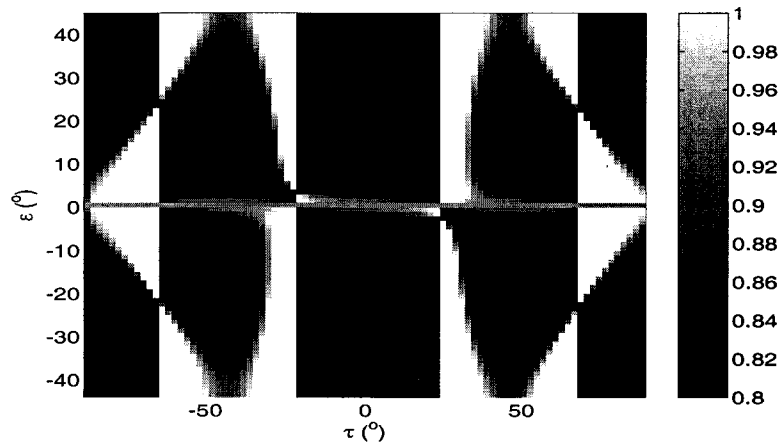

(b) Estimation by direct solution

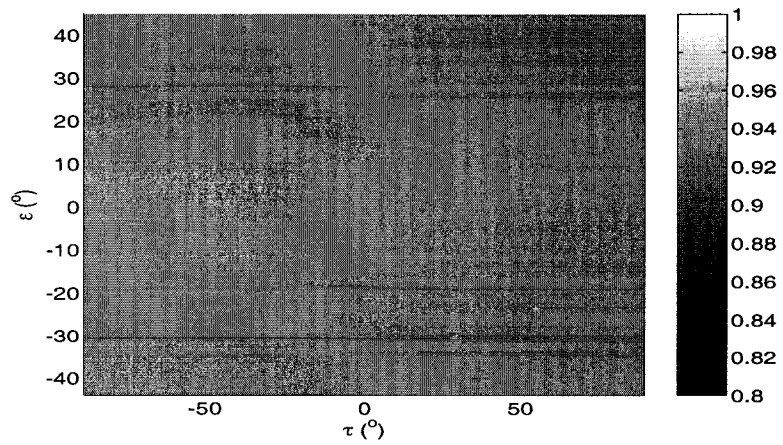

(c) Estimation by polarization optimization

Figure 3.7: The estimate of ρ_4 from the covariance matrices under different polarization bases

where λ refers to the wavelength.

By Oguchi's solution [39], the propagation matrix can be solved as:

$$\mathbf{P}(r) = \begin{bmatrix} P_{hh} & P_{hv} \\ P_{vh} & P_{vv} \end{bmatrix} = \mathbf{R}(\alpha) \begin{bmatrix} e^{\lambda_1 r} & \\ & e^{\lambda_2 r} \end{bmatrix} \mathbf{R}(-\alpha) \tag{3.78}$$

where α is the mean canting angle for this segment of propagation path and $\mathbf{R}$ is the related rotation matrix. As a result, the propagation matrix $\mathbf{P}$ is symmetric. What the radar measures is a "modified scattering" matrix, **PSP**, to which the concepts of basis transformation and feature vector are still applicable.

When the mean canting angle is zero, the propagation matrix deteriorates to a diagonal matrix that associates to λ_1 and λ_2. Such situation is referred as principal propagation where both the H and V polarized waves propagate without depolarization. The principal propagation parameters λ_1 and λ_2 depend on the elements of $\mathbf{P}$:

$$\lambda_{1,2} = -jk_0 + \frac{1}{2}\left[P_{hh} + P_{vv} \pm \sqrt{(P_{hh} - P_{vv})^2 + 4P_{vh}P_{hv}}\right] \tag{3.79}$$

Both are complex with the real parts relating to attenuation and the imaginary parts relating to phase lag incurred by propagation. Because we are only concerned with the relative functional dependency for the covariance matrix, the propagation matrix can be normalized by $e^{\lambda_1 z}$ such that

$$\mathbf{P}(r) = \mathbf{R}(\alpha) \begin{bmatrix} 1 & \\ & e^{u} \end{bmatrix} \mathbf{R}(-\alpha) \tag{3.80}$$

where

$$u = (\lambda_2 - \lambda_1)r = \left(\frac{A_{dp}}{8.686} + jK_{dp}\right) r \tag{3.81}$$

Therefore, at least two unknowns are introduced by propagation: the differential attenuation A_{dp} and the specific differential phase K_{dp}. In the past, K_{dp} was investigated intensively and was found to be an important measure of rain

rate [18]. However, as discussed above, the differential phase Φ_{dp} introduced by K_{dp} will smear the estimation of canting angle, hence Φ_{dp} must be estimated and adjusted. A filtering schema to estimate Φ_{dp} was described in [40]. For S-band radar, A_{dp} is fairly small except in heavy rain. Bringi [41] presented a self-consistent adaptive approach to make attenuation correction. In general, A_{dp} is related to K_{dp} by

$$A_{dp} = \beta K_{dp}^{b} \tag{3.82}$$

where b is close to 1 for over a wide frequency range (from 2.8 to 19 GHz) [42].

A unitary basis transformation can be imposed either directly to the propagation modified covariance matrix or separately to the scattering covariance matrix and the propagation matrix [43]. The proof is simply given in the following equation:

$$\begin{aligned}
\mathbf{S}'_E &= \mathbf{U}^T \mathbf{S}'_L \mathbf{U} \\
&= \mathbf{U}^T (\mathbf{P}_L \mathbf{S}^0_L \mathbf{P}_L) \mathbf{U} \\
&= \mathbf{U}^T \mathbf{P}_L (\mathbf{U}^* \mathbf{U}^T) \mathbf{S}^0_L (\mathbf{U}\mathbf{U}^{-1}) \mathbf{P}_L \mathbf{U} \\
&= (\mathbf{U}^{-1} \mathbf{P}_L \mathbf{U})^T (\mathbf{U}^T \mathbf{S}^0_L \mathbf{U}) (\mathbf{U}^{-1} \mathbf{P}_L \mathbf{U}) \\
&= \mathbf{P}^T_E \mathbf{S}^0_E \mathbf{P}_E
\end{aligned} \tag{3.83a}$$

Apparently, the propagation matrix in the new basis becomes $\mathbf{P}_E = \mathbf{U}^{-1} \mathbf{P}_L \mathbf{U}$.

3.4.1 Principal Propagation

Although for every single resolution bin the hydrometeor particles may exhibit non-zero canting, in average the canting angle tends to be zero such that the propagation matrix in linear H/V basis is diagonal for a homogeneous path [15].

Under diagonal propagation, the normalized propagation matrix is simply

$$\mathbf{P} = \begin{bmatrix} 1 & \\ & e^{u} \end{bmatrix} \tag{3.84}$$

and the covariance transformation matrix can be written as

$$\mathbf{T} = \begin{bmatrix} 1 & & \\ & e^{u} & \\ & & e^{2u} \end{bmatrix} \tag{3.85}$$

Hence the radar variables undergo such deviations including

$$Z'_{DR} = Z_{DR} - 2A_{dp}r \tag{3.86a}$$

$$LDR'_h = LDR_h + A_{dp}r \tag{3.86b}$$

$$\rho'_{hv} = \rho_{hv}e^{-j\phi_{dp}} \tag{3.86c}$$

$$\rho'_{xh} = \rho_{xh}e^{-j\phi_{dp}/2} \tag{3.86d}$$

$$\rho'_{xv} = \rho_{xv}e^{j\phi_{dp}/2} \tag{3.86e}$$

The power terms get biased by the differential attenuation A_{dp} while the correlation coefficients only experience phase shift. Therefore, the differential phase Φ_{dp} can be retrieved correctly from the correlations with appropriate filtering. Once Φ_{dp} is retrieved, A_{dp} is available from (3.82). In this thesis, the linear relation $A_{dp} = \beta K_{dp}$ is assumed and β will be fixed at 0.005 dB/km which is valid for S-band [42]. The principal propagation is the simplest case for wave propagation in rain medium, and the only situation that can be correctly adjusted.

The propagation matrix in circular basis can be obtained by applying (3.22) to $\mathbf{U}^{-1}\mathbf{P}_L\mathbf{U}$:

$$\mathbf{P}_C = \frac{1}{2}\begin{bmatrix} 1+e^{u} & 1-e^{u} \\ 1-e^{u} & 1+e^{u} \end{bmatrix} \tag{3.87}$$

which means circular polarized waves will suffer depolarization along the propagation path, as illustrated in Fig.3.8. From panel (b), the depolarization ratio keeps increasing with Φ_{dp}, along which both the returned powers and the correlation $ORTT$ change, as observed from other panels. Compared to the linear H/V polarization basis, the propagation correction is, in general, infeasible in circular basis [44].

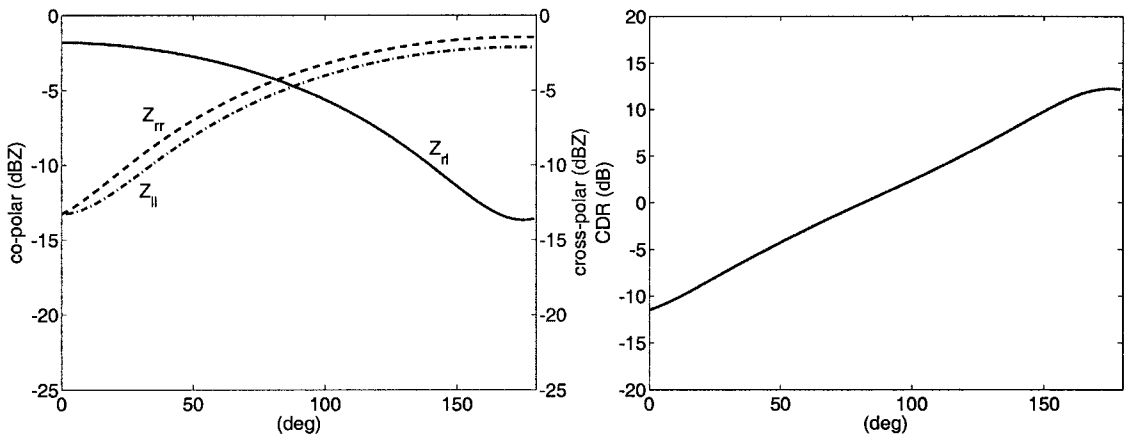

(a) reflectivities

(b) depolarization ratio

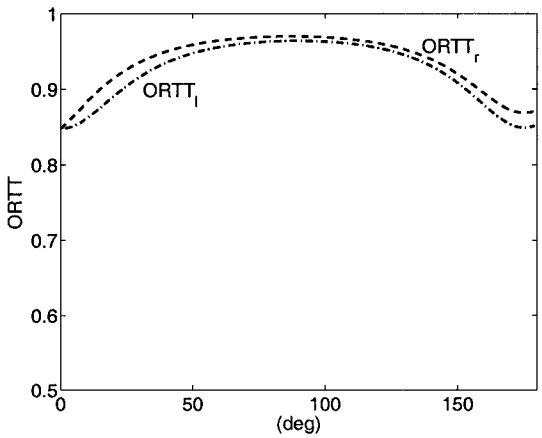

(c) ORTT

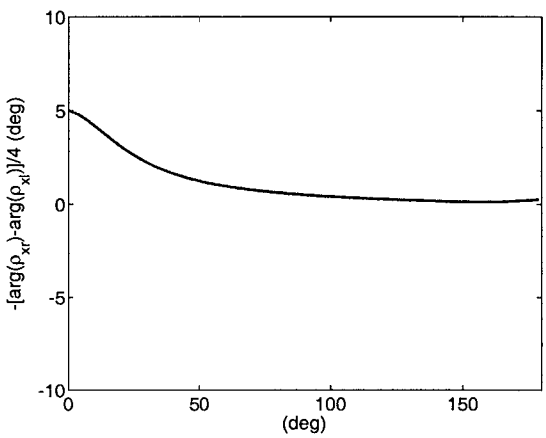

(d) differential phase

Figure 3.8: The circular polarimetric variables under diagonal propagation by simulation. The X-axis refers to Φ_{dp} defined in the linear H/V polarization basis.

3.4.2 Non-diagonal Propagation

However, occasionally there exist situations with non-zero canting on average, for example, small ice particles may be preferentially aligned due to cloud electrification.

Starting from (3.80), the propagation matrix in the linear H/V basis is now with depolarization:

$$\mathbf{P} = \begin{bmatrix} \cos\alpha & -\sin\alpha \\ \sin\alpha & \cos\alpha \end{bmatrix}^T \begin{bmatrix} T_h & \\ & T_v \end{bmatrix} \begin{bmatrix} \cos\alpha & -\sin\alpha \\ \sin\alpha & \cos\alpha \end{bmatrix} \tag{3.88a}$$

$$= \begin{bmatrix} \cos^2\alpha T_h + \sin^2\alpha T_v & (T_v - T_h)\sin\alpha\cos\alpha \\ (T_v - T_h)\sin\alpha\cos\alpha & \sin^2\alpha T_h + \cos^2\alpha T_v \end{bmatrix} \tag{3.88b}$$

There is no way to adjust the propagation effect correctly unless the net mean canting angle (α) could be retrieved accurately. Unfortunately, the net mean canting angle along propagation path usually cannot be separated from the mean canting angles (β_0) in individual resolution volumes.

Even a small α could increase the co-to-cross polar correlation coefficients dramatically [15], [45]. Fig.3.9 illustrates the effect of propagation with non-zero α on the cross-polar variables in the linear H/V basis where both β_0 and α equal to 0.5^o. The co-to-cross correlation coefficients increase with Φ_{dp} from 0.1 up to 0.3.

The propagation matrix in the circular basis can be modified to account for α as follows

$$\mathbf{P}_C = \begin{bmatrix} e^{j\alpha} & \\ & e^{-j\alpha} \end{bmatrix} \begin{bmatrix} 1+e^u & 1-e^u \\ 1-e^u & 1+e^u \end{bmatrix} \begin{bmatrix} e^{-j\alpha} & \\ & e^{j\alpha} \end{bmatrix} \tag{3.89a}$$

$$= \begin{bmatrix} T_a & T_b e^{j2\alpha} \\ T_b e^{-j2\alpha} & T_a \end{bmatrix} \tag{3.89b}$$

where $T_a = 1 + e^u$ and $T_b = 1 - e^u$. Similarly, if we define $R_a = S_{11} + S_{22}$ and $R_b = S_{11} - S_{22}$, the backscattering matrix in circular polarization basis can be

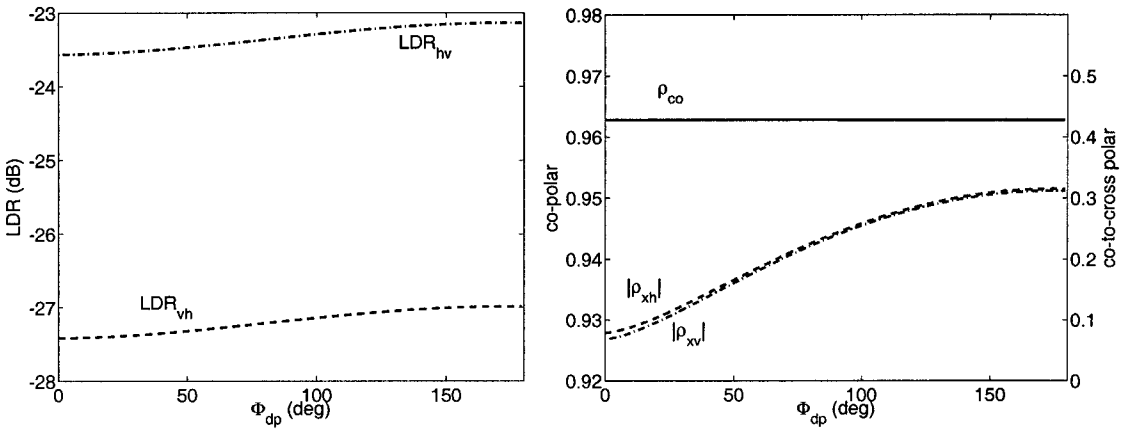

(a) linear depolarization ratio (dB)

(b) correlation coefficients

Figure 3.9: The effect of non-diagonal propagation on cross-polar polarimetric variables with α of 0.5^o. The propagation path is modelled with identically aligned particles, i.e., $\beta_0 = \alpha$.

formulated as

$$\mathbf{S}_C = \begin{bmatrix} e^{-j\beta} & \\ & e^{j\beta} \end{bmatrix} \begin{bmatrix} S_{11} - S_{22} & S_{11} + S_{22} \\ S_{11} + S_{22} & S_{11} + S_{22} \end{bmatrix} \begin{bmatrix} e^{-j\beta} & \\ & e^{j\beta} \end{bmatrix} \tag{3.90a}$$

$$= \begin{bmatrix} R_b e^{-j2\beta} & R_a \\ R_a & R_b e^{j2\beta} \end{bmatrix} \tag{3.90b}$$

Applying them to (3.83a), we have the propagation modified scattering matrix with elements:

$$S'_{RR} = T_a^2 R_b e^{-j2\beta} + 2T_a T_b R_a e^{-j2\alpha} + T_b^2 R_b e^{-j4\alpha + j2\beta} \tag{3.91a}$$

$$S'_{RL} = T_a T_b R_b e^{j2\alpha - j2\beta} + (T_a^2 + T_b^2) R_a + T_a T_b R_b e^{-j2\alpha + j\beta} \tag{3.91b}$$

$$S'_{LL} = T_a^2 R_b e^{j2\beta} + 2T_a T_b R_a e^{j2\alpha} + T_b^2 R_b e^{j4\alpha - j2\beta} \tag{3.91c}$$

This set of equations clearly illustrate how the angles β and α entangle together. Only if $\langle\beta\rangle = \alpha$, for example when the propagation path is composed of uniformly aligned particles, the orientation angle could be estimated correctly. Even though this situation is rarely encountered considering the inhomogeneous nature of precipitation, it describes the exact scenario for the misalignment of the antenna polarization axes. Such fact may be used to make a quick check on antenna alignment.

For general cases of non-diagonal propagation, the mean canting angle can be obtained if the propagation effect is minor compared to backscattering, or the average value α is available if the backscattering effect is minor compared to propagation. Checking with (3.91), the propagation effect will be minor only when

$$\frac{|T_b|}{|T_a|} = \frac{|1 - e^u|}{|1 + e^u|} \ll \frac{|R_b|}{|R_a|} \tag{3.92}$$

On the other hand, the backscattering effect is minor only when

$$\frac{|R_b|}{|R_a|} \ll \frac{|T_b|}{|T_a|} \tag{3.93}$$

Since only light attenuation is experienced in S-band, $u \approx j\Phi_{dp}/2$. When Φ_{dp} is small, we have

$$\frac{|T_b|}{|T_a|} \approx \sqrt{\frac{1 - \cos(\Phi_{dp}/2)}{1 + \cos(\Phi_{dp}/2)}} \tag{3.94}$$

For narrow shape distribution,

$$\frac{|R_b|}{|R_a|} \approx \sqrt{CDR} \tag{3.95}$$

Therefore, whether the backscattering effect or propagation effect dominates the measurement depends on which of Φ_{dp} and CDR is significantly large.

Assume $\beta_0 = 5^o$ and $\alpha = 1^o$, Fig.3.10(a) illustrates the effect of propagation on the estimate of orientation angles. In the simulation the intrinsic CDR is known as -11.5 dB, then by approximation the propagation is minor when $\Phi_{dp} < 6^o$; on the contrary the average value α is approached when Φ_{dp} becomes large. However, using the propagation modified covariance matrix in circular polarization basis, the estimate of ρ_4 is always goes up toward 1 with increasing Φ_{dp} due to cross-coupling, as shown in Fig.3.10(b).

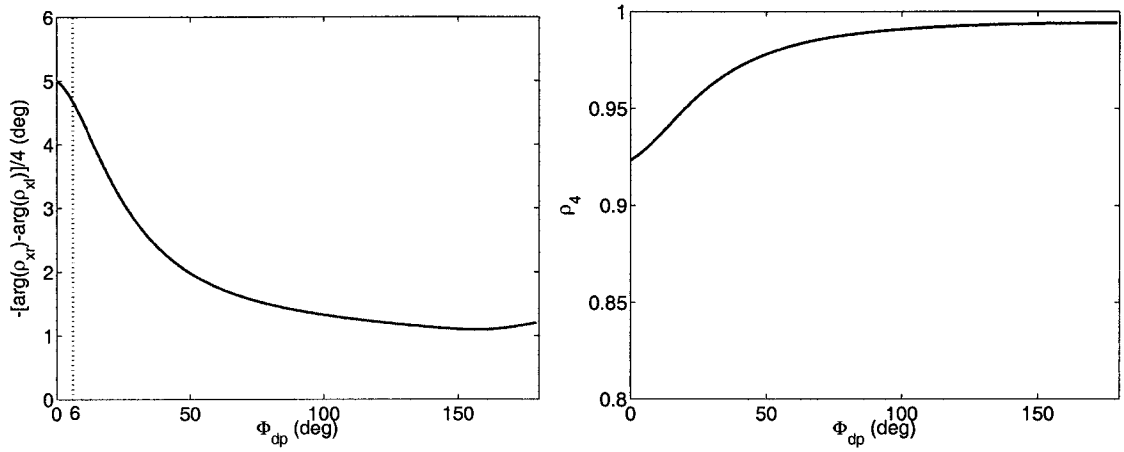

(a) orientation angle (b) ρ_4

Figure 3.10: The propagation effect on orientation estimation in circular polarization basis by simulation: $\beta_0 = 5^o$, $\alpha = 1^o$.

In addition, if the backscattering medium meets the condition of (3.93), the equations in (3.91) are simplified to:

$$W_- = 2\langle|R_a|^2\rangle e^{j2\alpha} T_a T_b (T_a^2 + T_b^2)^* \tag{3.96a}$$

$$W_+ = 2\langle|R_a|^2\rangle e^{-j2\alpha} T_a T_b (T_a^2 + T_b^2)^* \tag{3.96b}$$

$$W_2 = \langle|R_a|^2\rangle (T_a^2 + T_b^2)(T_a^2 + T_b^2)^* \tag{3.96c}$$

Therefore, the same results are reached as in [4]:

$$\frac{W_-}{W_2} e^{-j2\alpha} = \frac{W_+}{W_2} e^{j2\alpha} = \frac{2T_a T_b}{T_a^2 + T_b^2} = \frac{2(1 - e^{-2u})}{2(1 + e^{2u})} = \tanh(u) \tag{3.97}$$

3.4.3 Inhomogeneous Propagation

The propagation modified radar equation and covariance matrix can be generalized to inhomogeneous propagation path by segmenting the path into a cascade of homogeneous propagation matrices $\mathbf{P}_1$, $\mathbf{P}_2$, ..., $\mathbf{P}_n$, i.e.,

$$\mathbf{S}' = \mathbf{P}_1 \mathbf{P}_2 ... \mathbf{P}_{n-1} \mathbf{P}_n \mathbf{S}^0 \mathbf{P}_n \mathbf{P}_{n-1} ... \mathbf{P}_2 \mathbf{P}_1 \tag{3.98}$$

The equivalent propagation matrix for the whole inhomogeneous propagation path is the product of all the cascading homogeneous segments:

$$\mathbf{P} = \mathbf{P}_n \mathbf{P}_{n-1} ... \mathbf{P}_2 \mathbf{P}_1 \tag{3.99}$$

There still exists a pair of characteristic waves that can propagate without depolarization. However, we note from (3.99) that the propagation matrix is not symmetric anymore and the Oguchi's solution shown in (3.78) will not come with real element rotation, which means the principal propagation corresponds to a pair of general elliptical polarized waves.

The simulation of a ray profile in Fig.3.11 demonstrates this point. The principal plane variables as input to the model come from the field data of the CSU-CHILL radar for a heavy rain case in the STEPS project on Jun 11, 2000. The co-to-cross correlations are forced to 0 in order to mimic the principal plane measurement. The accumulated Φ_{dp} is estimated by adaptive filtering. Then the isolated backscattering covariance matrix is imposed to rotation by mean canting angle β_0 that is generated as Gaussian distributed random variable $N(2, 36)$ (in degree). In every gate the precipitation is assumed to be homogenous: $\alpha = \beta_0$.

Therefore, $\mathbf{P}_i$ can be derived from the filtered Φ_{dp} profile and the mean canting angle in every gate. By cascading, the total effective propagation matrix is decomposed into principal propagation and a complex matrix in the form of

$$\begin{bmatrix} \cos\alpha & \sin\alpha e^{j\delta_1} \\ \sin\alpha e^{j\delta_2} & \cos\alpha \end{bmatrix}$$

where α and $\delta_{1,2}$ are comparable to those in (3.14). The rotation angle α, shown in Fig.3.12(a), approaches the average of mean canting angle with farther propagation. Fig.3.12(b) indicates the primary difference between inhomogeneous propagation and homogenous propagation since, in homogeneous case, the phase offsets $\delta_{1,2}$ are 0^o and 180^o respectively.

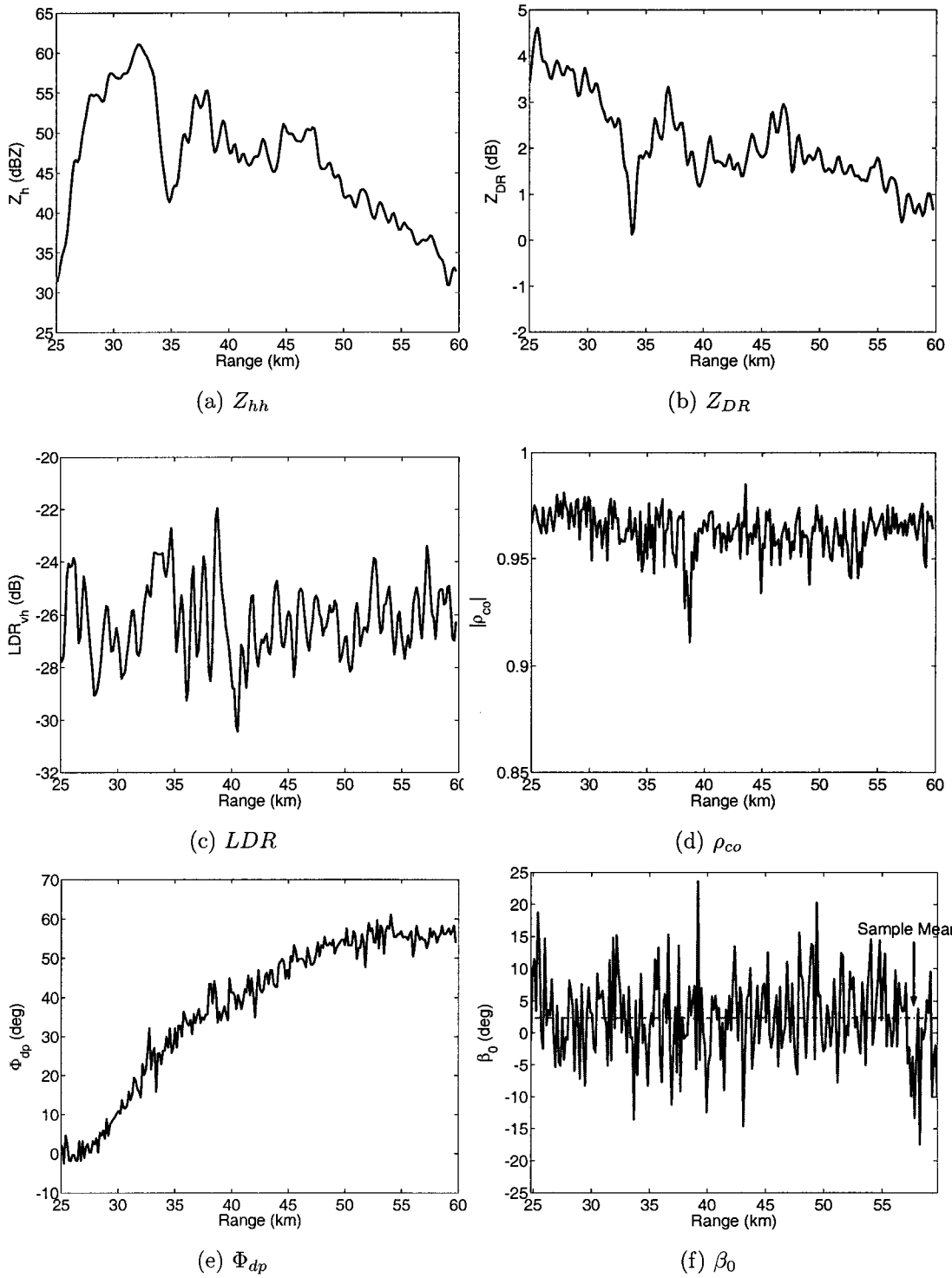

Figure 3.11: The input ray profiles for simulation of inhomogeneous propagation path: the CSU-CHILL field data of a heavy rain on Jun 11, 2000 22:25 UTC is taken for the radar variables in the principal plane, from (a) to (e); a Gaussian random model is presumed for mean canting angle β_0 in (f).

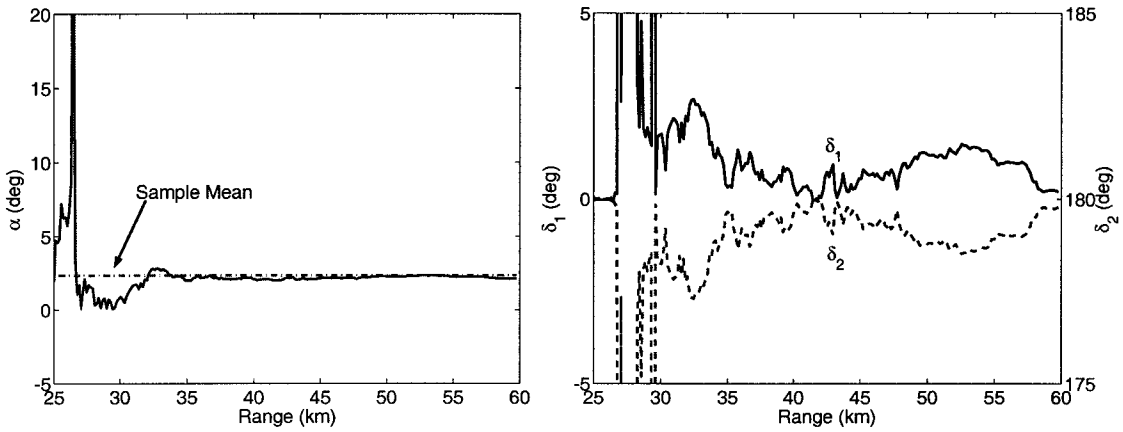

(a) α (b) δ

Figure 3.12: The decomposed propagation parameters for the simulated ray: (a) the rotation angle; (b) the associated phase offsets.

The above estimation algorithms, based on the linear and circular polarization basis, were developed with real value rotation matrix, which may fail for the inhomogeneous propagation path where elliptical polarization comes up. As for the optimization approach, however, since the full propagation matrix is unitary if A_{dp} is negligible, by investigating (3.80) and (3.99), the estimator of ρ_4 is still valid. To estimate the mean canting angle β_0, we assume the propagation to be almost diagonal. It is necessary to adjust Φ_{dp} first in order to apply the estimation algorithms. In practice α would be small, only small ellipticity can be introduced by this process and thus we presume that β_0 can be estimated. Suppose $A_{dp} = 0.005K_{dp}$ and no effort is made for the correction of A_{dp}, the estimates of β_0 are obtained and plotted in Fig.3.13(a). It shows that the optimization approach can restore β_0 quite accurately, while the estimation from circular covariance matrix suffers large errors. Fig.3.13(b) presents the estimates of ρ_4. As expected the estimate by optimization cannot exactly recover the intrinsic ρ_4 due to non-zero A_{dp}, but it out performs the other two approaches.

Similarly, more rays are simulated from the same field case. The statistics of estimation are listed in Table 3.2. In order to emphasis the propagation effect,

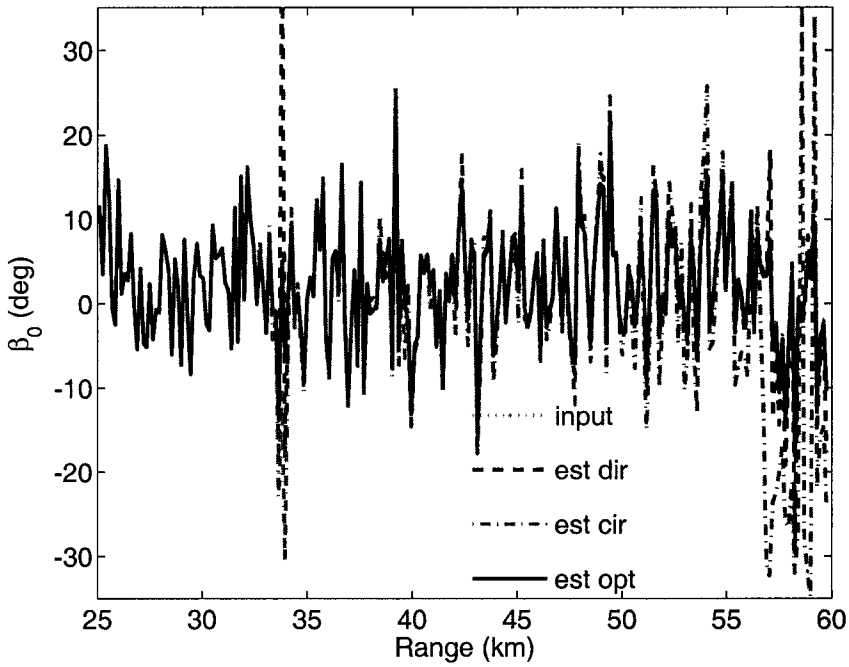

(a) β_0 and its estimation

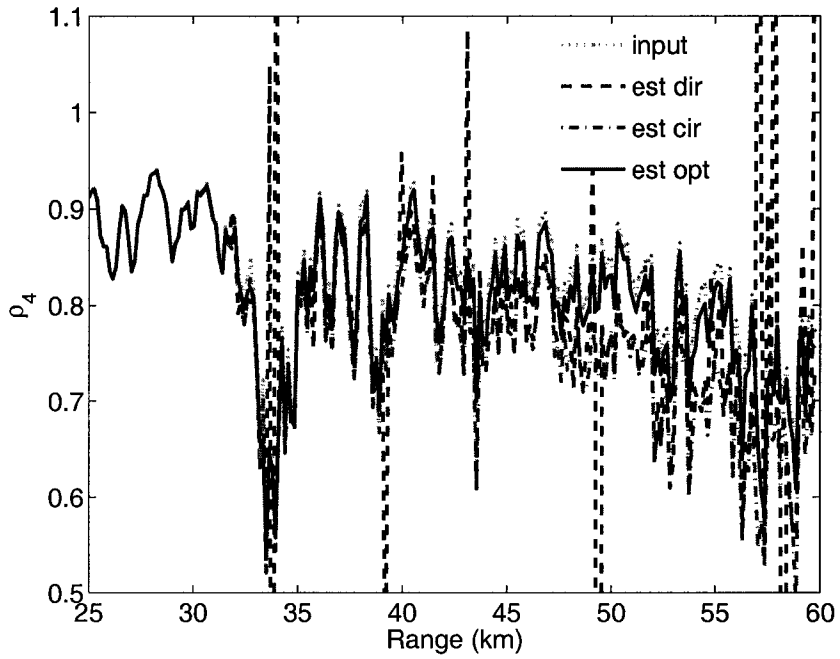

(b) ρ_4 and its estimation

Figure 3.13: The estimation of the orientation parameters for the simulated ray

the statistics take advantage of non-uniform weighted expectation where penalty is introduced to deep propagation segment. When no differential attenuation is experienced, β_0 can be estimated with reasonable accuracy by the direct solution or the optimization approach, and ρ_4 can be obtained by optimization very accurately. When propagation suffers differential attenuation, all the estimation performance deteriorates, but using the optimization approach, the estimation accuracy becomes only a little worse especially for ρ_4. If the differential attenuation can be properly corrected, accurate estimate of ρ_4 is still available by optimization. On the other hand, when α increases, worse performance will be expected as shown in Table 3.3 where it is raised to 10 degree.

Differential Attenuation		**Estimation Method**	$\hat{\beta}_0$		$\hat{\rho}_4$	
			Bias	**MSE**	**Bias**	**MSE**
$A_{dp} = 0$		Linear Cov.	-0.200	0.053	-0.055	0.006
		Circular Cov.	-1.327	28.008	-0.050	0.004
		Optimization	-0.200	0.053	-0.002	0.000
$A_{dp} = 0.005K_{dp}$	with attenuation correction	Linear Cov.	-0.534	0.586	-0.062	0.006
		Circular Cov.	-1.924	36.439	-0.054	0.004
		Optimization	-0.301	0.115	-0.002	0.000
	no attenuation correction	Linear Cov.	-0.512	37.782	-0.043	0.150
		Circular Cov.	-2.241	93.090	-0.070	0.008
		Optimization	-0.206	0.163	-0.016	0.000

Table 3.2: Statistics of the estimation of orientation factors over inhomogeneous propagation path. The mean canting angle β_0 is generated as $N(2, 36)$ (in degree).

Differential Attenuation	**Estimation Method**	$\hat{\beta}_0$		$\hat{\rho}_4$	
		Bias	**MSE**	**Bias**	**MSE**
$A_{dp} = 0.005K_{dp}$ (with attenuation correction)	Linear Cov.	-2.382	9.735	-0.620	197.3
	Circular Cov.	-20.579	1308.2	-0.496	0.276
	Optimization	-1.353	2.124	-0.003	0.000

Table 3.3: Same as Table 3.2 except that β_0 is generated as $N(10, 36)$ (in degree).

3.5 Effect of Antenna Polarization Errors

The antenna polarization error is another factor distorting the polarimetric measurement. For polarimetric applications, the ideal linear dual polarization radar should be able to radiate pure H or V polarized electromagnetic waves and receive pure orthogonal H and V components of the scattered fields. However, imperfection always exists in antenna and its feeding network. The antenna polarization errors include two parts: spatial distributed imperfection across the beam and "integrated" imperfection. The former one has been studied along gradients in the previous chapter. In this section, the latter one will be analyzed, i.e., beam "integrated" errors.

After the gradient induced polarization errors are sorted out using the methodology in Chapter 2, the precipitation medium could be regarded as homogeneous in the sense of reflectivity intensity and the beam integrated polarization errors are applicable as the matrix

$$\mathbf{X} = \begin{bmatrix} i_h & e_v \\ e_h & i_v \end{bmatrix} \tag{3.100}$$

where $i_h, i_v \in \mathbb{R}$ and $i_h^2 + |e_h|^2 = i_v^2 + |e_v|^2 = 1$. The measurement is then distorted by $\mathbf{X}$ as follows:

$$\mathbf{S}' = \mathbf{X}^T \mathbf{S} \mathbf{X} \tag{3.101}$$

The error matrix $\mathbf{X}$ generally is nonorthogonal. Therefore, the theory of unitary transformation is not applicable to analyze the antenna polarization errors.

However, the error matrix in (3.101) is still comparable to the basis transformation given in (3.31), so the analysis can be facilitated through two independent complex polarization ratios, each of which builds connection with a pair of tilt angle and ellipticity angle. Define the depolarization ratio in h transmission as

$$\chi_h = e_h / i_h \tag{3.102}$$

and the depolarization ratio in v transmission as

$$\chi_v = e_v/i_v \tag{3.103}$$

then the antenna polarization error matrix $\mathbf{X}$ can be reformulated as follows,

$$\mathbf{X} = \begin{bmatrix} \frac{i_h}{\sqrt{i_h^2+|e_h|^2}} & \frac{e_v}{\sqrt{i_v^2+|e_v|^2}} \\ \frac{e_h}{\sqrt{i_h^2+|e_h|^2}} & \frac{i_v}{\sqrt{i_v^2+|e_v|^2}} \end{bmatrix} \tag{3.104a}$$

$$= \begin{bmatrix} \frac{1}{\sqrt{1+|\chi_h|^2}} & \frac{\chi_v}{\sqrt{1+|\chi_v|^2}} \\ \frac{\chi_h}{\sqrt{1+|\chi_h|^2}} & \frac{1}{\sqrt{1+|\chi_v|^2}} \end{bmatrix} \tag{3.104b}$$

The definition of χ_h is consistent with (3.14). Consulting (3.15) and (3.16), we get the geometric representation:

$$2\tau_h = \arctan\left(\frac{2\Re(\chi_h)}{1-|\chi_h|^2}\right) \tag{3.105a}$$

$$2\epsilon_h = \arcsin\left(\frac{2\Im(\chi_h)}{1+|\chi_h|^2}\right) \tag{3.105b}$$

Considering χ_v, however, extra care is necessary to account for the convention of its definition. The geometric representation turns out to be:

$$2\tau_v = 180^o + \arctan\left(\frac{2\Re(\chi_v^{-1})}{1-|\chi_v|^{-2}}\right) \tag{3.106a}$$

$$2\epsilon_v = \arcsin\left(\frac{2\Im(\chi_v^{-1})}{1+|\chi_v|^{-2}}\right) \tag{3.106b}$$

where the additional 180^o accounts for the fact that the angle is measured from h polarization. Thus, we see the advantage of the representation (3.104) over that (3.100) such as:

(1) achieve a geometric understanding of the antenna polarization errors;

(2) map the error space into a closed and bounded space of angles τ ($[-90^o, 90^o]$) and ϵ ($[-45^o, 45^o]$).

Suppose the error matrix is given as

$$\begin{aligned} &\tau_h = 0.4^o;\ \epsilon_h = 0.6^o \\ &\tau_v = 89.6^o;\ \epsilon_v = -0.3^o \end{aligned} \tag{3.107}$$

which corresponds to a matrix

$$\mathbf{X} = \begin{bmatrix} 1.000 & 0.009e^{j36.9^o} \\ 0.013e^{j56.3^o} & 1.000 \end{bmatrix} \tag{3.108}$$

we expect some trend on the cross-polar variables with increasing Φ_{dp} similar to that of non-diagonal propagation. Such relation appears in Fig.3.14 but it is hard to tell whether the trend is positive or negative due to the nonorthogonality.

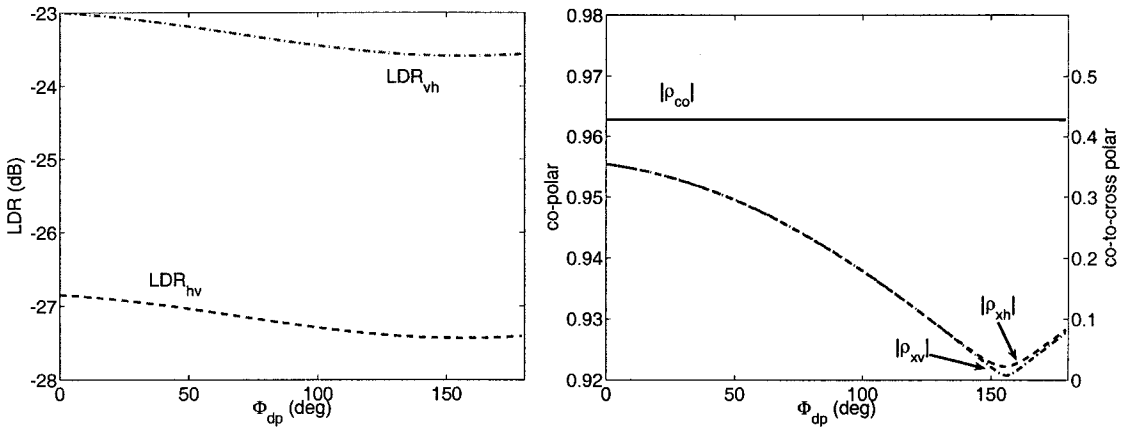

(a) linear depolarization ratio

(b) correlation coefficients

Figure 3.14: The effect of antenna polarization errors on the cross-polar polarimetric variables. The mean canting angle is zero throughout the propagation path.

It has already been proved in the previous sections that the ellipticity angle and tilt angle will increase the cross-polar power return if orthogonal basis transformation is applied. As for antenna polarization errors, we need to check whether the cross-polar power in the principal plane reaches its minimum under nonorthogonal basis transformation. Following the same procedure developed for basis transformation, we get the cross-polar power in terms of polarization ratios as

$$\begin{aligned} Z'_{vh} =& \frac{1}{(1+|\chi_h|^2)(1+|\chi_v|^2)}\{Z_{hh}|\chi_v|^2 + Z_{vv}|\chi_h|^2 \\ &+ Z_{vh}\left[1 + 2\Re(\chi_h\chi_v) + |\chi_h|^2|\chi_v|^2\right] + 2\Re(R_{hv}\chi_h^*\chi_v)\} \end{aligned} \tag{3.109}$$

where the radar variables on the right hand refer to those in the principal plane, which convention is followed hereafter in this section. Note that zero co-to-cross correlations are enforced in the above equation.

By defining $\chi_h = s + jt$ and $\chi_v = u + jv$, the following equation is arrived

$$\begin{aligned} Z'_{vh} =& \frac{1}{(1+s^2+t^2)(1+u^2+v^2)}[Z_{hh}(u^2+v^2) + Z_{vv}(s^2+t^2) \\ &+ Z_{vh}(1+s^2v^2+t^2u^2+s^2u^2+t^2v^2+2su-2tv) \\ &+ 2\Re(R_{hv})(su+tv) + 2\Im(R_{hv})(tu-sv)] \end{aligned} \tag{3.110}$$

Its gradient $\vec{g}$ can be evaluated as

$$\begin{aligned} \begin{bmatrix} \frac{\partial P'_{vh}}{\partial s} \\ \frac{\partial P'_{vh}}{\partial t} \\ \frac{\partial P'_{vh}}{\partial u} \\ \frac{\partial P'_{vh}}{\partial v} \end{bmatrix} =& -2 \begin{bmatrix} \frac{s}{1+s^2+t^2} \\ \frac{t}{1+s^2+t^2} \\ \frac{u}{1+u^2+v^2} \\ \frac{v}{1+u^2+v^2} \end{bmatrix} P'_{vh} + \frac{2}{(1+s^2+t^2)(1+u^2+v^2)} \cdot \\ & \begin{bmatrix} sZ_{vv} + (sv^2+su^2+u)Z_{vh} + u\Re(R_{hv}) - v\Im(R_{hv}) \\ tZ_{vv} + (tv^2+tu^2-v)Z_{vh} + v\Re(R_{hv}) + u\Im(R_{hv}) \\ uZ_{hh} + (ut^2+us^2+s)Z_{vh} + s\Re(R_{hv}) + t\Im(R_{hv}) \\ vZ_{hh} + (vt^2+vs^2-t)Z_{vh} + t\Re(R_{hv}) - s\Im(R_{hv}) \end{bmatrix} \end{aligned} \tag{3.111}$$

If there is no antenna polarization error, the error matrix equals to the 2×2 identity matrix and hence $\chi_h = \chi_v = 0$ based on the definitions (3.102) and (3.103). Then,

$$\vec{g}_{\mathbf{X}=\mathbf{I}} = \vec{g}(s=t=u=v=0) = \mathbf{0} \tag{3.112}$$

Since the gradient is 0, it proves that the cross-polar power has one of its extrema located on the principal plane in nonorthogonal transformation space. This statement could also be validated through simulation. Using the simulated covariance matrix for rain, its cross-polar power on the principal plane shows a minimum value. Two separate cuts on plane χ_h and χ_v are given in Fig.3.15.

When the measurement is contaminated by antenna polarization errors, we can find and locate its minima by optimization.The location of this minima is then given by,

$$\mathbf{X}\mathbf{X}' = \mathbf{I} \tag{3.113}$$

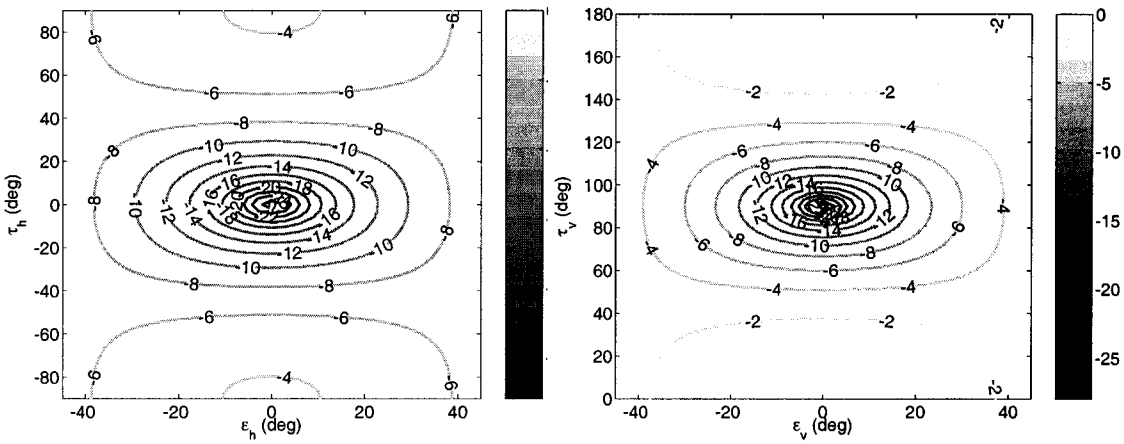

(a) The cross-polar power on χ_h plane

(b) The cross-polar power on χ_v plane

Figure 3.15: The change of cross-polar power due to nonorthogonal basis transformation. Here the contours on two planes cutting through the principal plane are displayed.

or simply by directly changing the sign of the geometrical angles that attain this optimization. Since we starts from the error contaminated radar measurement, the co-to-cross correlations need to be considered in the formulating of optimization. The cross-polar power due to nonorthogonal basis transformation becomes

$$\begin{aligned} P'_{vh} =& \frac{1}{(1+|\chi_h|^2)(1+|\chi_v|^2)}\{Z_{hh}|\chi_v|^2 + Z_{vv}|\chi_h|^2 + 2\Re(R_{hv}\chi_h^*\chi_v) \\ &+ Z_{vh}\left[1 + 2\Re(\chi_h\chi_v) + |\chi_h|^2|\chi_v|^2\right] + 2\Re(R_{xh}\chi_v) \\ &+ 2\Re(R_{xh}^*\chi_h|\chi_v|^2) + 2\Re(R_{xv}\chi_h) + 2\Re(R_{xv}^*|\chi_h|^2\chi_v)\} \end{aligned} \tag{3.114}$$

Its gradient vector $\vec{g}$ and Hessian matrix $\mathbf{H}$ could be evaluated analytically but the formula would be cumbersome. To simplify the algorithm, the antenna error is further assumed to be very small so that

$$1 + |\chi_h|^2 \approx 1, 1 + |\chi_v|^2 \approx 1 \tag{3.115}$$

The gradient can be written as follows:

$$\begin{aligned}\vec{g} \approx 4 \Bigg[& \begin{array}{l} sZ_{vv} + (sv^2 + su^2 + u)Z_{vh} + u\Re(R_{hv}) - v\Im(R_{hv}) \\ tZ_{vv} + (tv^2 + tu^2 - v)Z_{vh} + v\Re(R_{hv}) + u\Im(R_{hv}) \\ uZ_{hh} + (ut^2 + us^2 + s)Z_{vh} + s\Re(R_{hv}) + t\Im(R_{hv}) \\ vZ_{hh} + (vt^2 + vs^2 - t)Z_{vh} + t\Re(R_{hv}) - s\Im(R_{hv}) \end{array} \\ & \begin{array}{l} +(u^2 + v^2)\Re(R_{xh}) + (2su + 1)\Re(R_{xv}) + 2sv\Im(R_{xv}) \\ +(u^2 + v^2)\Im(R_{xh}) + 2tu\Re(R_{xv}) + (2tv - 1)\Im(R_{xv}) \\ +(2su + 1)\Re(R_{xh}) + 2tu\Im(R_{xh}) + (s^2 + t^2)\Re(R_{xv}) \\ +2sv\Re(R_{xh}) + (2tv - 1)\Im(R_{xh}) + (s^2 + t^2)\Im(R_{xv}) \end{array} \Bigg]\end{aligned} \tag{3.116}$$

and the Hessian is derived as

$$\mathbf{H} \approx 4 \begin{bmatrix} Z_{vv} + (v^2 + u^2)Z_{vh} + 2u\Re(R_{xv}) + 2v\Im(R_{xv}) & 0 \\ 0 & Z_{vv} + (v^2 + u^2)Z_{vh} + 2u\Re(R_{xv}) + 2v\Im(R_{xv}) \\ (2su + 1)Z_{vh} + \Re(R_{hv}) + 2u\Re(R_{xh}) + 2s\Re(R_{xv}) & 2utZ_{vh} + \Im(R_{hv}) + 2u\Im(R_{xh}) + 2t\Re(R_{xv}) \\ 2vsZ_{vh} - \Im(R_{hv}) + 2v\Re(R_{xh}) + 2s\Im(R_{xv}) & (2vt - 1)Z_{vh} + \Re(R_{hv}) + 2v\Im(R_{xh}) + 2t\Im(R_{xv}) \end{bmatrix}$$
$$\begin{bmatrix} (2su + 1)Z_{vh} + \Re(R_{hv}) + 2u\Re(R_{xh}) + 2s\Re(R_{xv}) & 2svZ_{vh} - \Im(R_{hv}) + 2v\Re(R_{xh}) + 2s\Im(R_{xv}) \\ 2tuZ_{vh} + \Im(R_{hv}) + 2u\Im(R_{xh}) + 2t\Re(R_{xv}) & (2tv - 1)Z_{vh} + \Re(R_{hv}) + 2v\Im(R_{xh}) + 2t\Im(R_{xv}) \\ Z_{hh} + (t^2 + s^2)Z_{vh} + 2s\Re(R_{xh}) + 2t\Im(R_{xh}) & 0 \\ 0 & Z_{hh} + (t^2 + s^2)Z_{vh} + 2s\Re(R_{xh}) + 2t\Im(R_{xh}) \end{bmatrix} \tag{3.117}$$

Once the gradients and Hessian are available, the minima could be located and retrieved by Newton's method. The mathematic foundation of Newton's method is the fact that every continuous function can be locally approximated by a quadratic form around the minima. The related iteration is given as follows,

$$\vec{x}_{i+1} = \vec{x}_i + \mathbf{H}^{-1}\vec{g} \tag{3.118}$$

where the subscript i denotes the iteration number and x_0 is the initial point. The initial point is set to $s = t = u = v = 0$ since the antenna error is usually small. The minimum is assumed to be reached if

$$|Z'_{vh}(x_{i+1}) - Z'_{vh}(x_i)| < \epsilon \tag{3.119}$$

From (3.114) the cross-polar power approximates a quadratic function, it could be expected that the algorithm will converge fast. Applying the error matrix (3.108) to the simulated intrinsic covariance matrix (3.38), we obtain the "measured" covariance matrix contaminated with antenna polarization errors. The algorithm

by Newton's method is able to converge to the minimum within several iterations as shown in Table (3.4). In the first iteration, the algorithm has already approached the solution, which in turn shows a quadratic function as a good approximation to (3.114). The Hessian on the solution point is positive definite, which proves the solution is a minimum. From the solution, the estimation of antenna polarization errors is retrieved in polar angles. The estimates are very close to the input error (3.107).

Init:				
	$\epsilon = 10^{-12}$			
	$[\chi_h, \chi_v] = [0, 0]$			
Iterations:				
	i	Z'_{vh}	χ_h	χ_v
	1.0000	0.0036	-0.0072-j0.0105	-0.0069-j0.0052
	2.0000	0.0036	-0.0072-j0.0106	-0.0069-j0.0052
	3.0000	0.0036	-0.0072-j0.0106	-0.0069-j0.0052
Status:				
	$\mathbf{H} > 0$, optimization succeeds.			
Estimation:				
	$\begin{bmatrix} \hat{\tau}_h & \hat{\tau}_v \\ \hat{\epsilon}_h & \hat{\epsilon}_v \end{bmatrix} = \begin{bmatrix} 0.4119 & 89.6064 \\ 0.6049 & -0.2953 \end{bmatrix}$			

Table 3.4: The iterations of Newton optimization algorithm for simulated covariance matrix contaminated with antenna polarization errors

This optimization approach can be used to obtain complex calibration matrix accounting for the antenna polarization errors. Suppose the mean canting angle on average could be reasonably assumed to be zero, then estimates of the antenna errors can be retrieved. With the same approach used for the simulated ray profile in Fig.(3.11) except setting the propagation matrix diagonal and the mean canting angle on average zero, the estimated polarization angles for the antenna errors are given in Table 3.5. The estimated polarization angles in sample mean closely approach the intrinsic values for the input antenna polarization errors in this simulation. Remember that the mean canting angle is generated as

Gaussian distributed random variable with 6^o standard deviation. The estimated polarization angles also have large variation. To improve the confidence level, lots of samples may be required depending on the variance of canting angle.

Total Samples:	3510
Sample Mean:	$E\begin{bmatrix} \hat{\tau}_h & \hat{\tau}_v \\ \hat{\epsilon}_h & \hat{\epsilon}_v \end{bmatrix} = \begin{bmatrix} 0.46 & 89.66 \\ 0.59 & -0.25 \end{bmatrix}$
Sample Standard Deviation:	$\sigma\begin{bmatrix} \hat{\tau}_h & \hat{\tau}_v \\ \hat{\epsilon}_h & \hat{\epsilon}_v \end{bmatrix} = \begin{bmatrix} 4.98 & 5.23 \\ 1.95 & 2.04 \end{bmatrix}$

Table 3.5: Statistics of the estimated polarization angles for antenna polarization errors

3.6 Effect of Mixed Type Precipitation

In reality, precipitation is often composed of different hydrometeor types, for example, a mixture of raindrop and hailstone, and the mixed phase in melting level. The covariance matrix for the mixture precipitation is a superposition of all individual covariance matrices for every component. The observed characteristics of precipitation depends on the dominating components. If several components exist comparably, the "mirror" reflection symmetry may not be justified even if it is valid for every single component.

In some cases, one component of the mixture exhibits "mirror" reflection symmetry, while the other component may exhibit polarization plane isotropy, for example, when hail mixes with rain. The orientation of rain is of interest. For the component with polarization plane isotropy, its covariance matrix could be written

as follows according to (3.36)

$$Z_{hh} = Z_{vv} = \frac{3}{8}(\langle|S_{11}|^2\rangle + \langle|S_{22}|^2\rangle) + \frac{1}{4}\Re(\langle S_{11}S_{22}^*\rangle) \tag{3.120a}$$

$$Z_{vh} = \frac{1}{8}(\langle|S_{11}|^2\rangle + \langle|S_{22}|^2\rangle - 2\Re(\langle S_{11}S_{22}^*\rangle)) \tag{3.120b}$$

$$R_{hv} = \frac{1}{8}(\langle|S_{11}|^2\rangle + \langle|S_{22}|^2\rangle + 6\Re(\langle S_{11}S_{22}^*\rangle)) \tag{3.120c}$$

$$R_{xh} = R_{xv} = 0 \tag{3.120d}$$

Since $Z_{hh} - Z_{vv} = 0$ and $R_{xh} - R_{xv} = 0$, (3.51) can still be applied to retrieve the mean canting angle of the component with "mirror" reflection symmetry. However based on (3.53) the dispersion ρ_4 is not available for the individual component.

This fact is consistent with the conclusion drawn on circular covariance matrix in [18]. From (3.41), it is obvious that the covariance for isotropic component is:

$$Z_{rr} = Z_{ll} = \frac{1}{4}\langle|S_{11} - S_{22}|^2\rangle \tag{3.121a}$$

$$Z_{rl} = \frac{1}{4}\langle|S_{11} + S_{22}|^2\rangle \tag{3.121b}$$

$$R_{rl} = 0 \tag{3.121c}$$

$$R_{xr} = R_{xl} = 0 \tag{3.121d}$$

Since the correlations are unaltered, it follows that the mean canting angle of the other component is given unaffected by (3.42). However, because the power terms attribute to both components, a direct estimation of ρ_4 is not possible.

When the problem is put on the context of optimization, it is immediately realized that the basis rotation will not affect the cross-polar power for the isotropic component, therefore the mean canting angle can be estimated from the optimization for the other component. Even the difference between maximum cross-polar power and minimum cross-polar power does not change, the ratio in (3.55) does change by the mixture.

The extent of influence on ρ_4 can be derived considering such two-component scenario. If we use superscript 's' to label the component with "mirror" reflection

symmetry and 'i' to label the other, the effective ρ_4 is estimated for the mixture as

$$\rho_4^m = \rho_4^s \frac{\langle |S_{11}^s - S_{22}^s|^2 \rangle}{\langle |S_{11}^s - S_{22}^s|^2 \rangle + \langle |S_{11}^i - S_{22}^i|^2 \rangle} \tag{3.122}$$

Generally, the estimation for mixture deserves particular care to draw valid implications.

3.7 Summary

The dual-polarization radar measurement was studied on complex vector space and the underlying physical process was represented by linear map on this space. A polarization pair implemented in the radar system defines the basis of the vector space. The representation of the linear map depends on the employed basis and can be transformed from one orthogonal basis to another through unitary matrix. The general form of basis transformation was given. All the effect of canting, propagation and antenna polarization errors can be described by basis transformation.

Concerning polarimetric radar measurement, the transformation between different polarization bases was also derived. With the derived transformation matrix, the radar measurement (the constructed covariance matrix) in one polarization configuration can be transformed to any other polarization configuration. The commonly used configurations include linear polarization and circular polarization. The linear covariance matrix by CSU-CHILL radar was transformed to the corresponding circular covariance matrix.

Hydrometeor particles may experience non-zero canting. The canting angle rotates the polarization basis from its principal plane. The distribution of canting angle can be described by two orientation factors: mean canting angle and its dispersion, both of which can be retrieved directly from the covariance matrix in circular polarization basis. The covariance matrix in linear polarization basis

can be also directly solved to obtain the orientation factor and shape factors. For orientation factors, the ambiguity range of estimated mean canting angle is doubled. Optimization can be utilized to obtain the orientation parameters from the covariance matrix under any orthogonal basis. The polarization optimization was extended to obtain robust estimation of the orientation dispersion.

When the mean canting angle is zero, the net effect over the propagation path will be zero even though it may not true for individual backscattering volume. Linear polarized wave in H/V polarization propagates in such medium without depolarization. In contrast, the circular polarized wave may suffer strong depolarization. Large Φ_{dp} may be experienced and must be adjusted to obtain orientation estimation for the backscattering volume. When the net mean canting angle is not zero, the propagation matrix is not diagonal and depolarization will be induced for both linear and circular polarization basis. The mean canting angle for the backscattering volume or the net angle for the propagation path may be estimated from the circular covariance matrix depending on Φ_{dp}, but in general, it is impossible to separate the two variables. When large Φ_{dp} is accumulated, the cross-polar radar variables in linear polarization basis will experience significant change even when the net mean canting angle is rather small. This effect can be used to examine whether the propagation matrix is diagonal. If identical orientation distribution governs the precipitation medium along the propagation path, the developed algorithms are still able to obtain reasonable estimation of the mean canting angle.

Generally, the antenna polarization error introduces non-diagonal transformation. The antenna polarization error matrix can be studied conveniently through its ellipticity and tilt angles, which implies that the effect of antenna polarization errors is comparable to non-diagonal propagation. Similar but more complicated changes can be observed on the cross-polar radar signatures in linear polarization

basis. The polarization optimization theory was extended to non-orthogonal basis transformation and the antenna polarization errors can be estimated with reasonable accuracy. An optimization algorithm based on Newton method was given and shown to converge very fast.

Chapter 4

ESTIMATION OF ORIENTATION FACTORS

Up to now, the polarimetric covariance measurement for radar meteorology has been analyzed by decomposing the model in (1.13) into several parts: that due to canting, that due to propagation, and that due to antenna; and related methods and algorithms have been presented. In this chapter, those algorithms will be applied to radar data to estimate the orientation factors β_0 and ρ_4.

The procedure to construct the covariance matrix will be reviewed first where the radar measurement is carefully calibrated, especially for the phase terms. Then the antenna polarization errors will be estimated from rain observation assuming its mean canting angle is zero. The estimated errors will be examined through the cross-polar radar variables such as co-to-cross correlation coefficients. Finally the "intrinsic" covariance matrix is obtained and the algorithms for retrieving the orientation factors can be applied.

Several cases for different precipitation types will be analyzed. The radar variables under both linear and circular polarization basis will be compared for those different hydrometeor types along with the estimated orientation factors. The comparison has two objectives: to validate further the estimation algorithms; and to explore potential usage of the derived/estimated variables for improving hydrometeor type classification.

4.1 Construct Covariance Matrix from Measurement

The first step is to construct the covariance matrix from the radar measurement. The gain imbalance and relative phase between two channels have not been considered in the previous analysis. Both artifacts need to be adjusted carefully to our best knowledge. An in-depth development on calibration methodology can be found in [46]. Moreover, since the "weak" cross-polar signals act on the process of estimation, the noise power should be taken out during the construction as well.

4.1.1 Calibration on power terms

With a meteorological radar working on full covariance mode, the complex voltage samples $V_{vv}(2i)$, $V_{hv}(2i)$, $V_{hh}(2i+1)$, and $V_{vh}(2i+1)$ are available. The power terms are directly estimated as follows:

$$\hat{P}_{hh} = \frac{1}{M}\sum_{i=1}^{M}|V_{hh}(2i+1)|^2 - N0_h \tag{4.1a}$$

$$\hat{P}_{vv} = \frac{1}{M}\sum_{i=1}^{M}|V_{vv}(2i)|^2 - N0_v \tag{4.1b}$$

$$\hat{P}_{vh} = \frac{1}{M}\sum_{i=1}^{M}|V_{vh}(2i+1)|^2 - N0_v \tag{4.1c}$$

$$\hat{P}_{hv} = \frac{1}{M}\sum_{i=1}^{M}|V_{hv}(2i)|^2 - N0_h \tag{4.1d}$$

where $N0_h$ and $N0_v$ denote the noise power presented at receiver channel h and v, respectively. Then absolute calibration is applied to get reflectivity:

$$Z_{hh} = 10\log_{10}\hat{P}_{hh} + \Delta Z_{hh} + RC + 20\log_{10}(r) \tag{4.2}$$

where ΔZ_{hh} is the bias, RC is radar constant, and r is the slant range at this gate. The absolute calibration is not important in the estimations. Instead, the relative

calibration is critical, such as:

$$Z_{DR} = 10\log_{10}\hat{P}_{hh} - 10\log_{10}\hat{P}_{vv} + \Delta Z_{DR} \tag{4.3a}$$

$$LDR_{vh} = 10\log_{10}\hat{P}_{vh} - 10\log_{10}\hat{P}_{hh} + \Delta LDR_{vh} \tag{4.3b}$$

$$LDR_{hv} = 10\log_{10}\hat{P}_{hv} - 10\log_{10}\hat{P}_{vv} + \Delta LDR_{hv} \tag{4.3c}$$

These biases Z_{DR}, LDR_{vh} and LDR_{hv} can be calculated using sun calibration [46], [16].

4.1.2 Estimation of correlations and phase offsets

The co-to-cross correlation terms are estimated as

$$\hat{R}_{xh} = \frac{1}{M}\sum_{i=1}^{M} V_{hh}(2i+1)V_{vh}^{*}(2i+1) \tag{4.4a}$$

$$\hat{R}_{xv} = \frac{1}{M}\sum_{i=1}^{M} V_{vv}(2i)V_{hv}^{*}(2i) \tag{4.4b}$$

However, the co-polar correlation cannot be estimated directly from measurement due to the alternate pulsing scheme in full covariance mode. A description on how to obtain the co-polar correlation is given in [47] where several approaches are compared and an additional polarization state is suggested on transmission. Without the additional polarization state, the co-polar correlation can be approximated from its estimation at lag 1 according to:

$$|\hat{R}_{hv}| = \frac{1}{2}\rho_{hh}(2)^{-1/4}[|\hat{R}_{hv}(-1)| + |\hat{R}_{hv}(1)|] \tag{4.5}$$

where

$$\hat{R}_{hv}(-1) = \frac{1}{M}\sum_{i=1}^{M} V_{vv}^{*}(2i)V_{hh}(2i+1) \tag{4.6a}$$

$$\hat{R}_{hv}(1) = \frac{1}{M-1}\sum_{i=1}^{M-1} V_{vv}^{*}(2i+2)V_{hh}(2i+1) \tag{4.6b}$$

$$\rho_{hh}(2) = \frac{1}{M-1}\sum_{i=1}^{M-1} V_{hh}(2i)V_{hh}^{*}(2i+2)/\hat{P}_{hh} \tag{4.6c}$$

The value $\rho_{hh}(2)$ is used to adjust the decorrelation incurred between two consecutive pulses assuming the Doppler spectrum is Gaussian shaped. Note that irregular Doppler spectrum will result in bias [48]. Similarly the differential phase is estimated as

$$\Psi_{dp} = -\frac{1}{2}\arg\{\hat{R}_{hv}(-1)\hat{R}_{hv}(1)\} \tag{4.7}$$

The phase offsets in transmission ϕ^t_{off} and in reception ϕ^r_{off} affect the estimates as [46]:

$$\hat{\Phi}_{dp} = \Phi_{dp} - \phi^t_{off} - \phi^r_{off} \tag{4.8a}$$

$$\hat{\Phi}_{xh} = \Phi_{xh} + \phi^r_{off} \tag{4.8b}$$

$$\hat{\Phi}_{xv} = \Phi_{xv} - \phi^r_{off} \tag{4.8c}$$

The accumulated differential phase Φ_{dp} should start from around 0, so its offsets $(\phi^t_{off} + \phi^r_{off})$ can be obtained by observing the filtered phase profiles. Besides, the differential propagation phase shift can be estimated from the co-to-cross correlations by

$$\Phi_{dp} = \Phi_{xv} - \Phi_{xh} \tag{4.9}$$

Substituting this relation into (4.8), we have

$$\hat{\Phi}_{dp} - (\hat{\Phi}_{xv} - \hat{\Phi}_{xh}) = 2\phi^r_{off} - (\phi^t_{off} + \phi^r_{off}) \tag{4.10}$$

which will give us the estimate of the phase offsets contained in co-to-cross polar differential phase shifts after the phase offset contained in co-polar differential phase shift is determined through (4.8a).

4.1.3 Filtering over phase profiles

A filtering process on phase profiles was described in [40]. In this section, instead of filtering on the real valued phase profiles, an approach of phase filtering is proposed based on directional statistics.

The differential propagation phase obtained by differencing the phases of co-to-cross correlations as expressed in (4.9) has high variance due to low power level in cross-polar channels. Moreover, for Raleigh scatters with small imaginary parts of refractive index (e.g., crystals), the phase of both co-to-cross correlations is either 0 or π depending on the sign of the mean canting angle [15]. Therefore, its range profiles are very likely flipping by 360^o as shown in Fig.4.1(a). Such flipping needs to be detected and adjusted first in order to achieve decent filtering. However, it is awkward to flip back but also difficult to design a robust algorithm for that considering phase wrapping.

Such a problem comes from the artificial discontinuities introduced by expanding circular variables to the real axis. The appropriate approach is to filter the phase profile along the unit circle rather than on the real axis. Therefore, complex polar representation is necessary and directional statistics should be applied.

Suppose there is an angular random variable θ which is periodic over 2π, its sample statistics can be formulated as follows [49]. The sample mean is

$$\bar{\theta} = \arg\{\frac{1}{N}\sum_{i=1}^{N} e^{j\theta_i}\} \tag{4.11}$$

and a measure of its concentration can be given by

$$\bar{\rho} = |\frac{1}{N}\sum_{i=1}^{N} e^{j\theta_i}| \tag{4.12}$$

The relation between its standard deviation and this concentration could be derived if the distribution is known. To demonstrate the relation, commonly used Gaussian

distribution and uniform distribution are taken as examples:

$$\bar{\rho} = e^{-\sigma^2/2} \quad \text{for } \theta : G(\bar{\theta}, \sigma^2) \tag{4.13a}$$

$$\bar{\rho} = |\frac{\sin(\Delta)}{\Delta}| \quad \text{for } \theta : U(\bar{\theta} - \Delta, \bar{\theta} + \Delta) \tag{4.13b}$$

Note that the derived concentration is independent of the sample mean.

Applying such definition of mean and concentration to the phase profile is equivalent to filtering over the complex valued range profile $e^{j\theta(r)}$. The same FIR filter is used as before to keep the range resolution. The argument of the filtered profile gives filtered phases and its magnitude presents information on the standard deviation. The filtered profiles are overlaid in Fig.4.1(a) for comparison. Without adjustment for flipping, the direct FIR filtering results in incorrect profile. Even though discontinuities may still exist in the filtered profile by directional statistics, they are caused by phase wrapping only so the edges would be sharp, e.g., the discontinuity shown in Fig.4.1(a) gives a jump of 359.52^o, which is as close as the period 360^o. Concerning the co-polar phase profile, however, Fig.(4.1(b)) illustrates the comparison on the same ray and it is obvious that both filtering methods generate same results.

The initial Φ_{dp} for every ray can be estimated by 10 consecutive "good" gates. As an example, we take a heavy rain case (which will be described in the next section), estimate the initial Φ_{dp} for every individual ray and collect them to generate a histogram as shown in Fig.(4.2(a)). The abscissa with the largest frequency is selected as the phase offset of the radar system. Similar approach is used to decide the phase offsets in cross-polar correlations by investigating the histogram of $\hat{\Psi}_{dp} - (\hat{\Psi}_{xv} - \hat{\Psi}_{xh})$ over the whole volume, according to (4.10). The phase offsets are then determined for this case as: $\phi^t_{off} + \phi^r_{off} = 61^o$; $\phi^r_{off} = -80.5^o$. Finally full covariance matrices could be constructed.

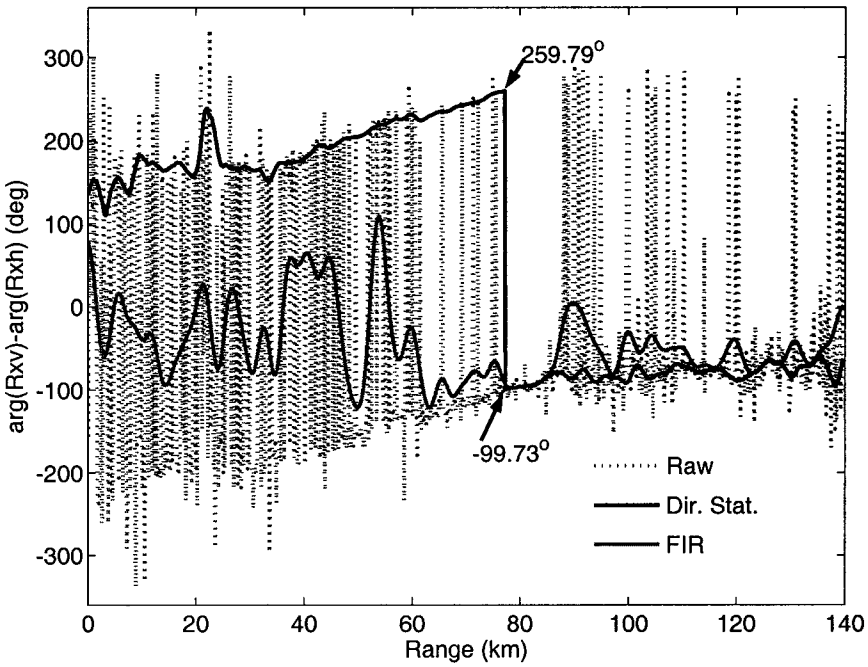

(a) cross-polar phase profile

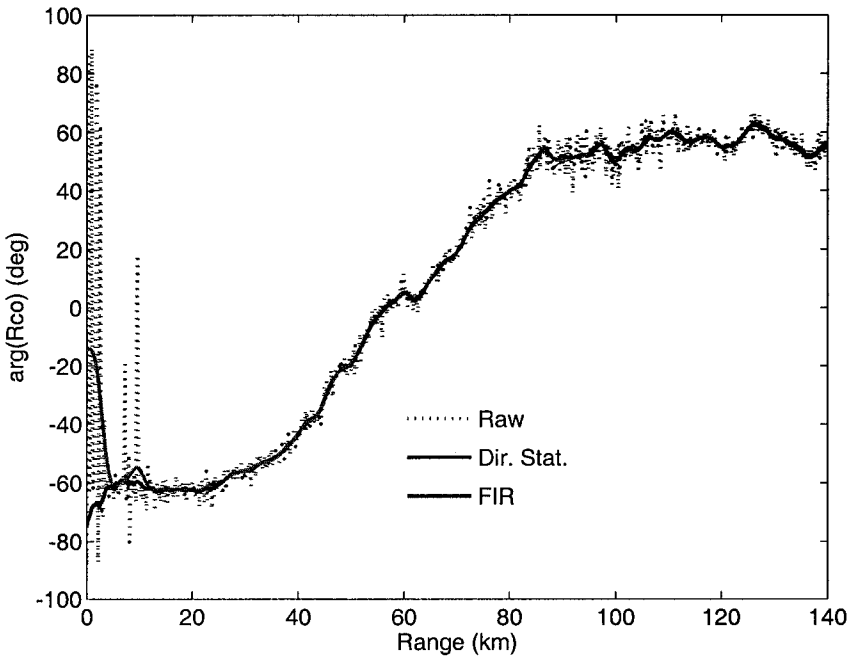

(b) co-polar phase profile

Figure 4.1: Range profiles of Φ_{dp} with different filtering approaches. The ray is selected from a heavy rain storm on July 21, 2000. EL: 0.54°; AZ: 343.36°.

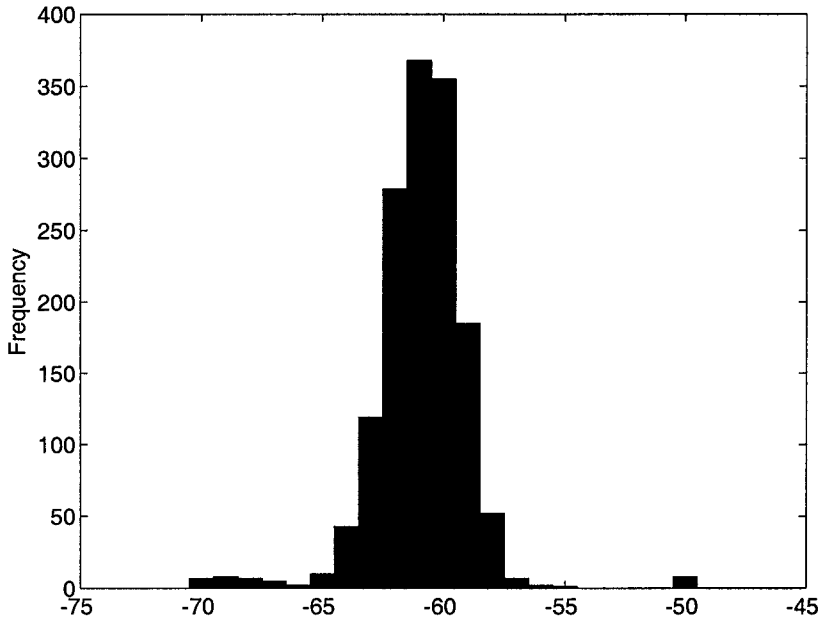

(a) $\hat{\Psi}_{dp}$ (deg)

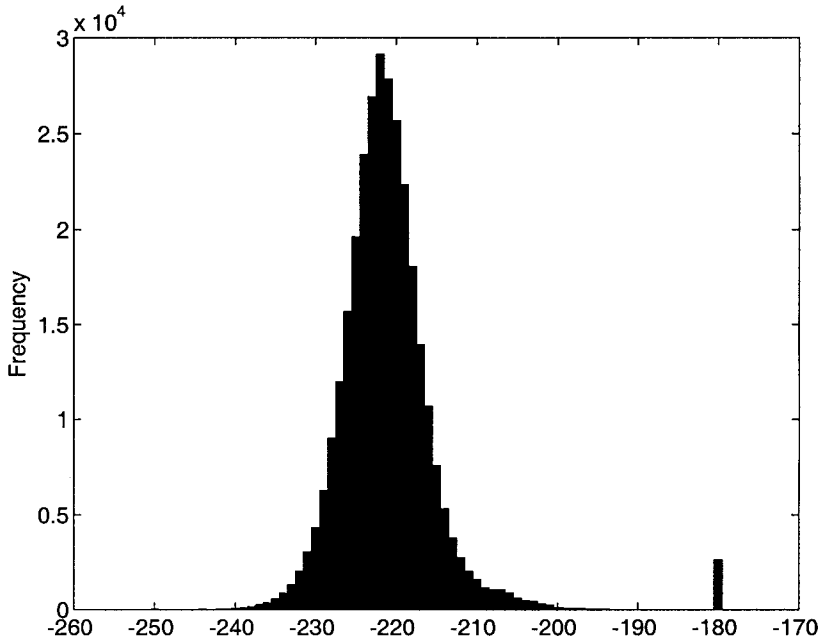

(b) $\hat{\Psi}_{dp} - (\hat{\phi}_{xv} - \hat{\phi}_{xh})$ (deg)

Figure 4.2: The histogram of phase offsets that are estimated from filtered range profiles for a heavy rain case. There are 1458 rays in the whole volume and 666 gates in every ray.

4.2 Estimation of Antenna Polarization Errors

Calibration of polarimetric radar measurements requires the knowledge of antenna polarization errors. It has been shown that the effect of antenna polarization errors is comparable to that of non-diagonal propagation. When the covariance matrix is used to estimate the orientation factors, it is very important to correct for the antenna polarization errors.

The quantitative estimation of antenna polarization errors can be calculated from both power patterns and phase patterns of the antenna. However, it is impractical to get accurate phase patterns. When the cross-polar power primarily attributes to the contamination of antenna polarization errors, the co-to-cross polar correlation coefficients would be high. High co-to-cross polar correlations were examined from dual-polarization measurements to show the existence of such errors and estimate the mean square terms in [27]. Similarly, vertical observation of light rain was used to estimate an adjustment factor for the calibration matrix in [29]. Both methods require that scattering only undergoes slight depolarization and $Z_h = Z_v$.

On the other hand, simulations show that even small polarization errors may lead to significant error in the polarimetric covariance matrix if large Φ_{dp} is accumulated over the propagation path. When large Φ_{dp} occurs, the tendency of co-to-cross polar correlation coefficients can be used to estimate the polarization errors [50]. The optimization approach given in previous section improve that methodology in both algorithm and extension of assumption. The optimization turns out to converge quickly and accurately, and large Φ_{dp} accumulation is not necessary. The simulation in previous section also demonstrates that the depolarization is allowed as long as the mean canting angle is zero.

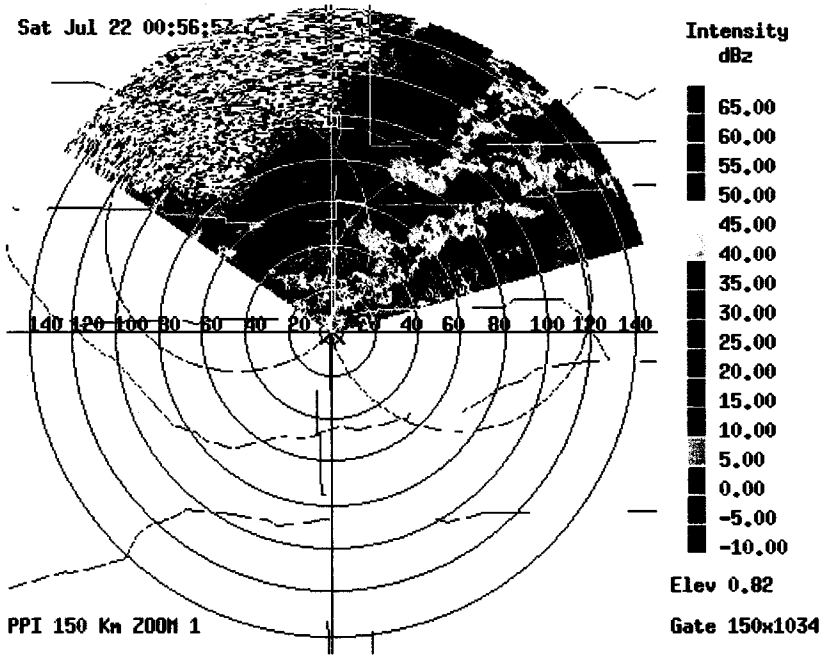

Figure 4.3: A PPI scan of Z_h (dBZ) at low elevation angle for the heavy rain case on July 21, 2000.

4.2.1 Case study 1: July 21, 2000 STEPS

On July 21, 2000 00:56 UTC, a heavy rain storm was observed by the CSU-CHILL radar during the STEPS project (see Fig.4.3 for a low elevation PPI scan of Z_h). Total differential propagation phase shifts greater than 200 degrees were observed along certain azimuths. Fig.4.4 illustrates the rapid increase of Φ_{dp} for several rays. The corresponding filtered coefficients ρ_{xh} and ρ_{xv} are given in Fig.4.5. A obvious increasing trend can be observed from these ray profiles, which indicates the existence of either non-diagonal propagation or antenna polarization errors. If we assume the mean canting angle of raindrops is zero, the optimization approach can be applied to estimate the antenna polarization errors. To further suppress canting effect along the propagation path, only resolution volumes with Φ_{dp} of less than 10^o are selected for the estimation and its statistics. Other constraints are also enforced to assure the data quality as shown in Table 4.1.

Selection Criteria:	$LDR < -26$ dB $\Phi_{dp} < 10^o$ $SNR > 40$ dB $\lvert\rho_{co}\rvert > 0.9$			
Total Samples Selected:	372			
Estimation (in degree):	$\hat{\tau}_h$ $\hat{\tau}_v$ $\hat{\epsilon}_h$ $\hat{\epsilon}_v$	=	-0.66 89.56 -0.08 0.17	

Table 4.1: The estimation of antenna polarization errors based on radar measurement from the selected volume.

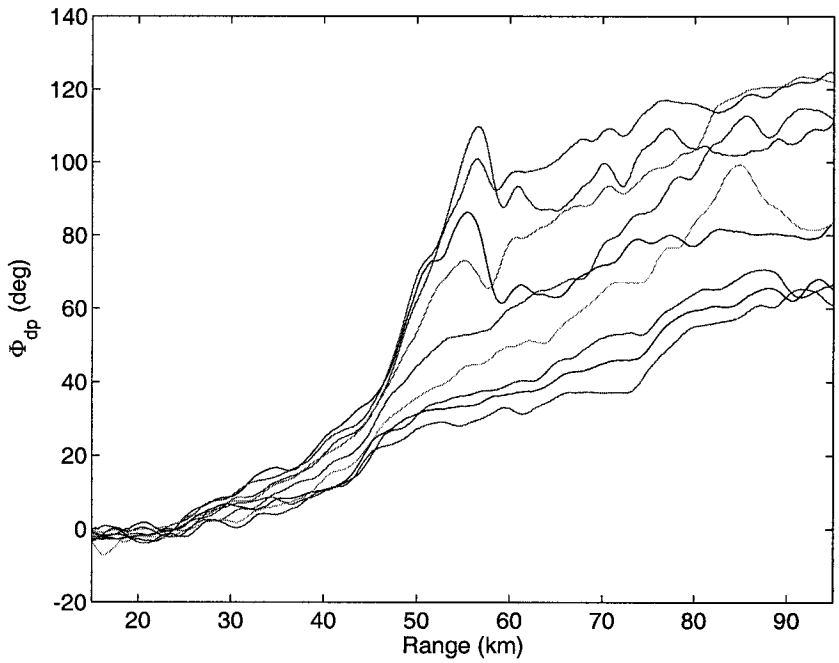

Figure 4.4: Selected range profiles of filtered Φ_{dp}. EL: 0.52°; AZ: 44.79°-51.51°.

The estimation result obtained here is close to that by Hubbert [50]: $\tau_h = -0.5^o$, $\tau_v = 89.5^o$, $\epsilon_h = -0.1^o$, and $\epsilon_v = 0.4^o$, which was obtained from 333 gates of a single ray at (EL=1.37 degree; AZ=47.85 degree). Just for the purpose of testing, the range profile for that ray is recovered by applying the estimated error matrix (given in Table 4.1) as shown in Fig.4.6. These curves are consistent with Hubbert's results. Since only the gates with Φ_{dp} of less than 10^o contribute to the estimation, the obtained value are more likely to be isolated from possible non-zero mean canting angle.

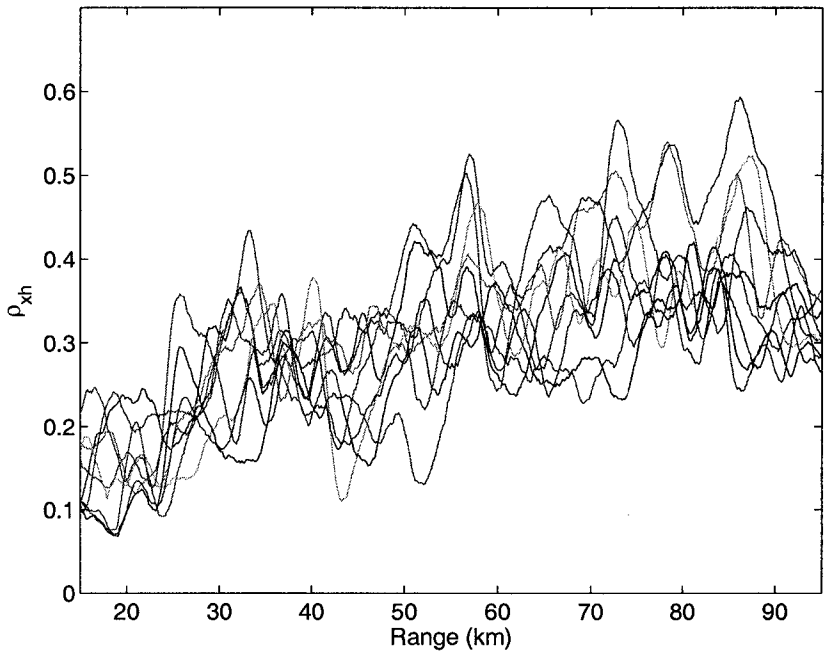

(a) ρ_{xh}

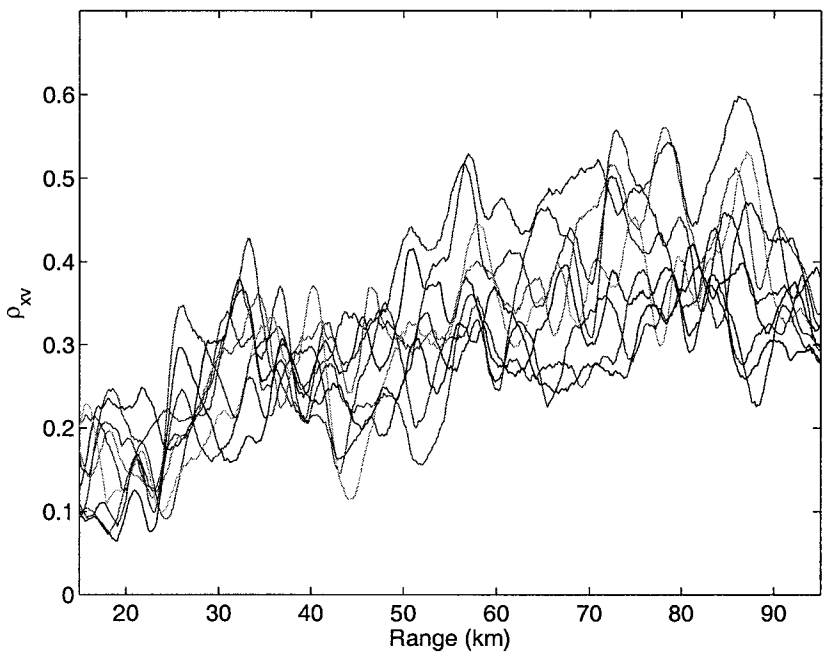

(b) ρ_{xv}

Figure 4.5: Same as Fig.4.4 except for the co-to-cross correlation coefficients.

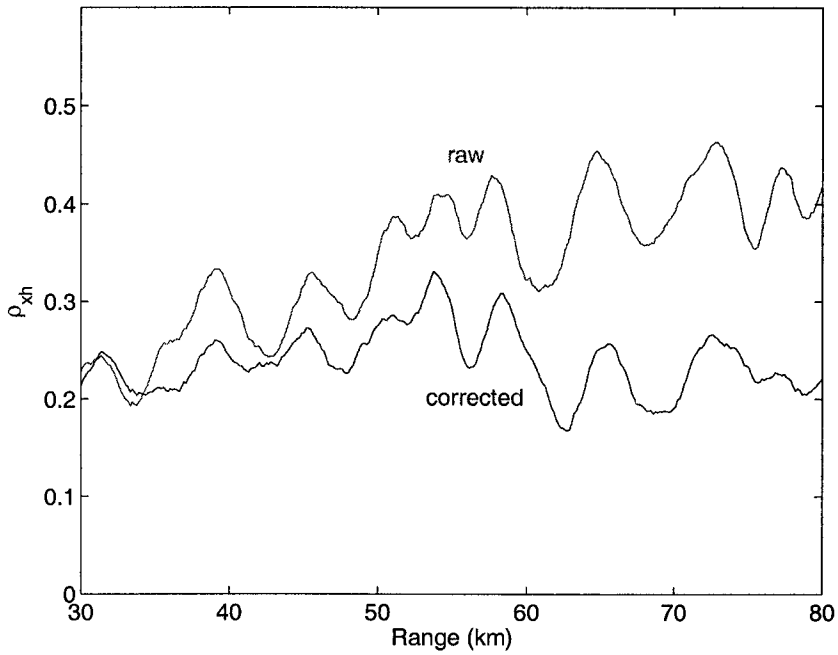

(a) ρ_{xh}

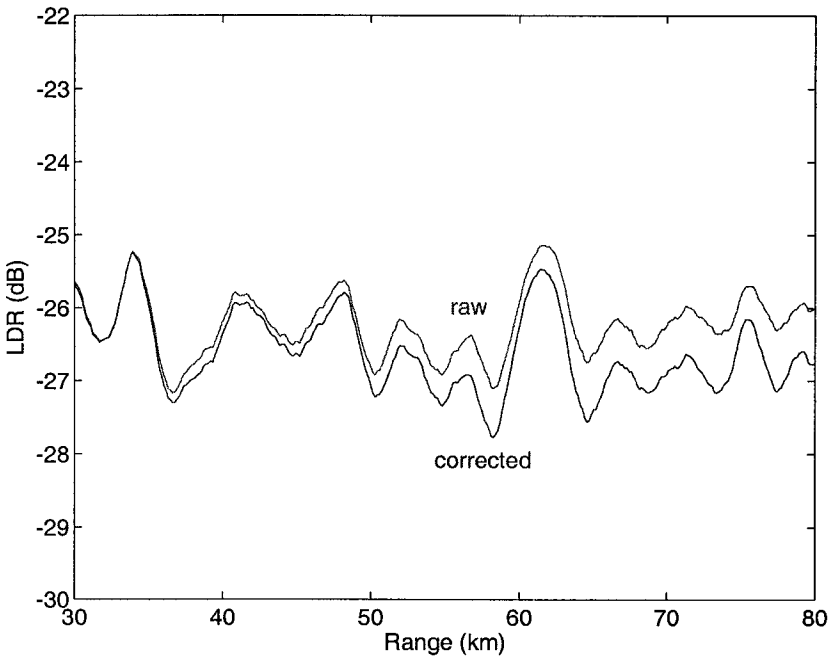

(b) LDR

Figure 4.6: The range profiles of the filtered ρ_{xh} and LDR, along with their correction for antenna polarization errors. EL: 1.37^o; AZ: 47.85^o.

It was shown in Fig.4.5 that such effect is not an isolated phenomena for that individual ray. Fig.4.7 illustrates the statistics of the cross-polar radar variables for the selected volume with comparisons between raw measurement and corrected measurement. The advantage of such error estimation and correction is apparent: both coefficients present "flat" signature, and the incurred LDR bias gets adjusted, after correction using the estimated error matrix.

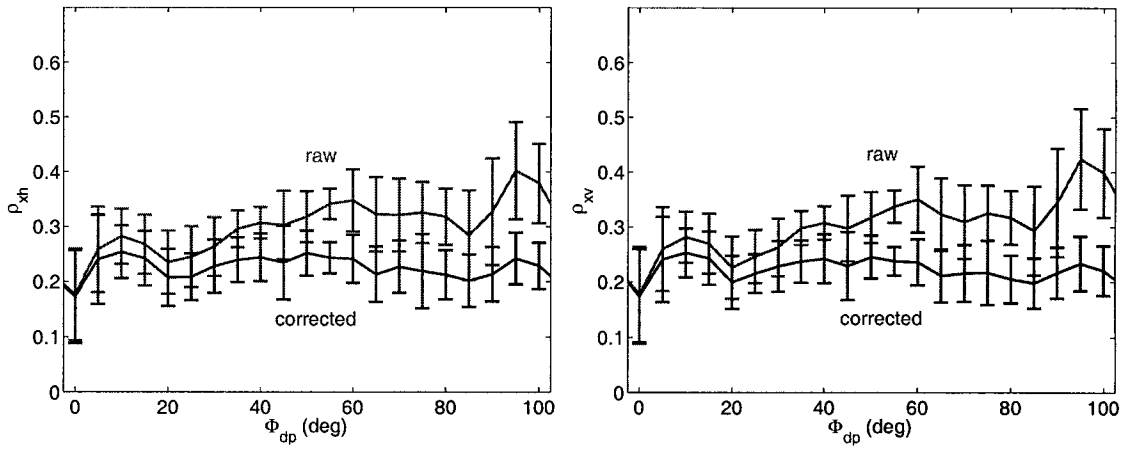

(a) ρ_{xh}

(b) ρ_{xv}

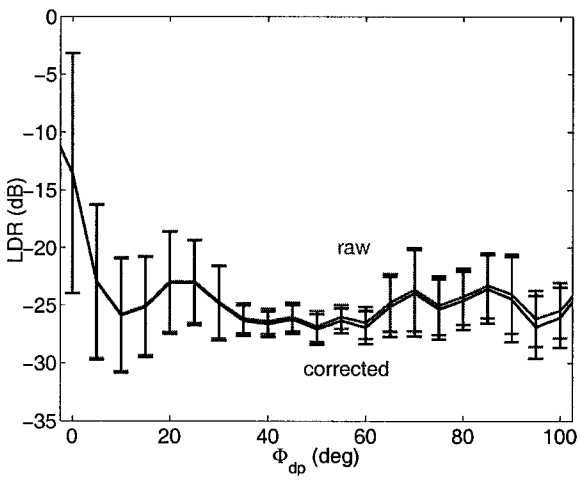

(c) $LDR(dB)$

Figure 4.7: The statistics of cross-polar radar variables over the selected volume, before and after the correction for antenna polarization error: (a) ρ_{xh}; (b) ρ_{xv}; (c) LDR.

4.2.2 Case study 2: July 19, 2000 STEPS

Two days earlier than the previous case, another convective storm was recorded during the STEPS project. On July 19, 2000 00:38 UTC, some other interesting rays are observed with decreasing trend for the range profiles of co-to-cross correlation coefficients while Φ_{dp} has large accumulation. A sample ray is taken from this volume and its range profile of Φ_{dp} is given in Fig.4.8.

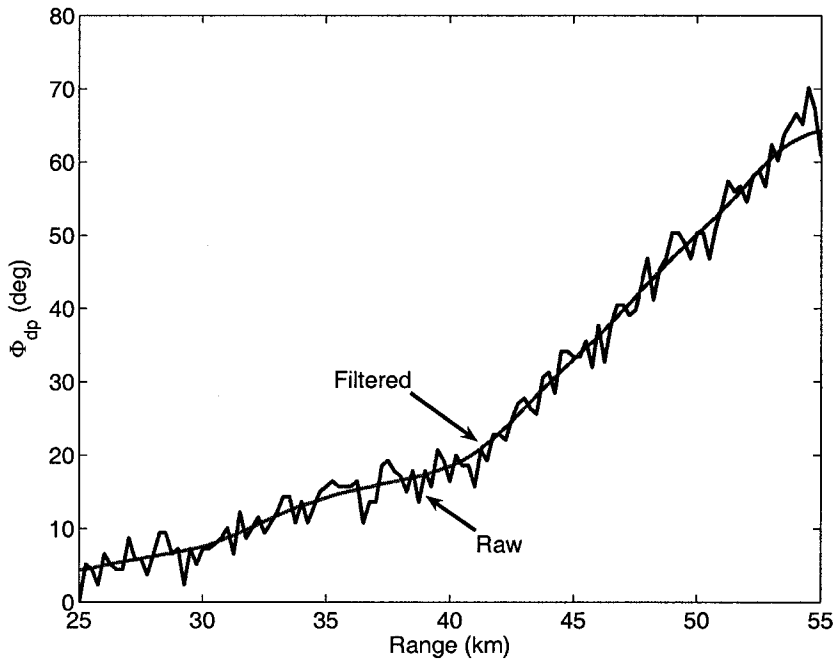

Figure 4.8: A selected range profile of Φ_{dp} from the convective storm on July 19, 2000 00:38 UTC. EL: 1.60°; AZ: 225.65°.

The Φ_{dp} increases by more than 60° from 25 km to 55 km along range. Over this segment apparent decrease can be observed on the profiles of co-to-cross correlation coefficients as shown in Fig.4.9. At the same time, the range profile of LDR does not show any abnormal increase based on Fig.4.10. Therefore, the apparent increase of the co-to-cross coefficients must be due to other system factors.

Just as shown by simulation in the previous chapter, the antenna polarization error can cause both increasing and decreasing trend over the propagation path

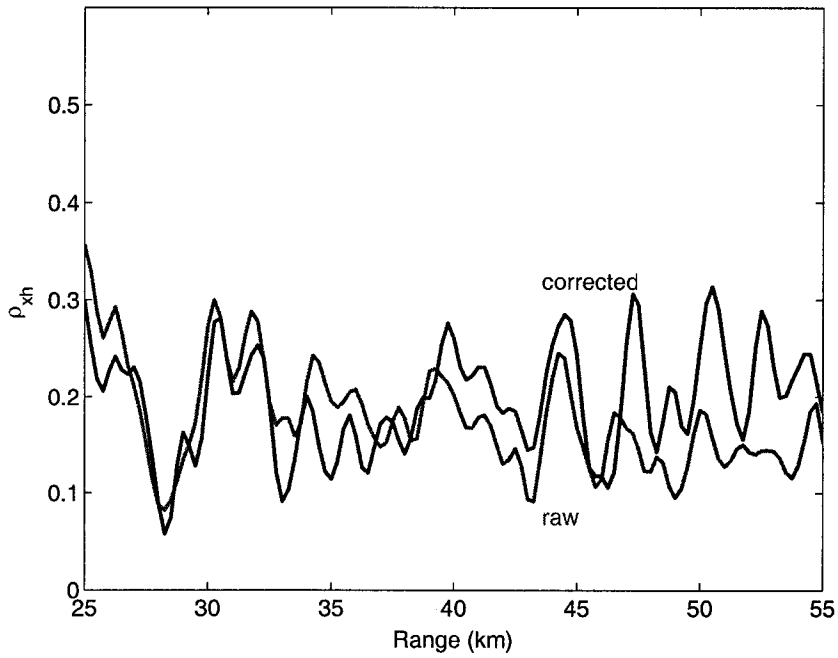

(a) ρ_{xh}

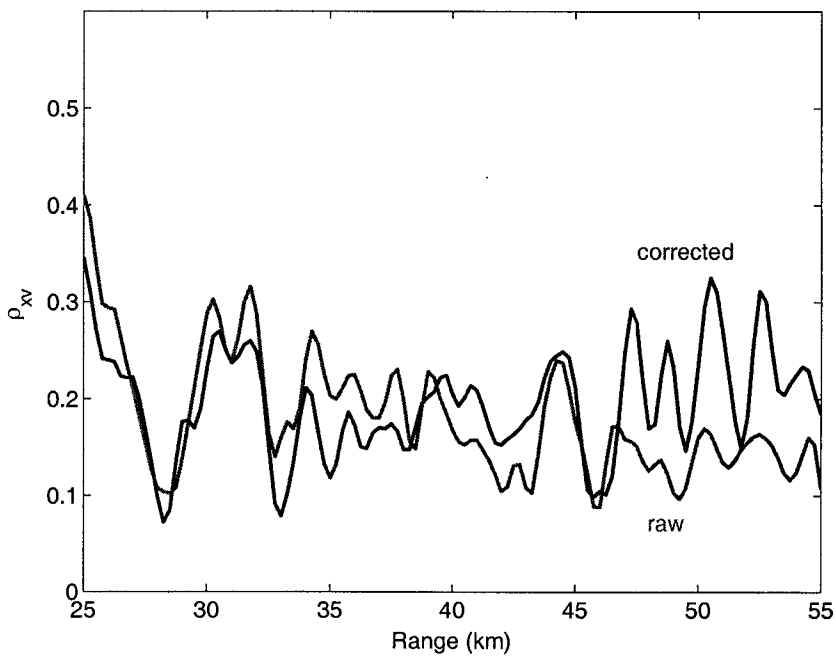

(b) ρ_{xv}

Figure 4.9: The range profiles of ρ_{xh} and ρ_{xv} for the selected ray as in Fig.4.8.

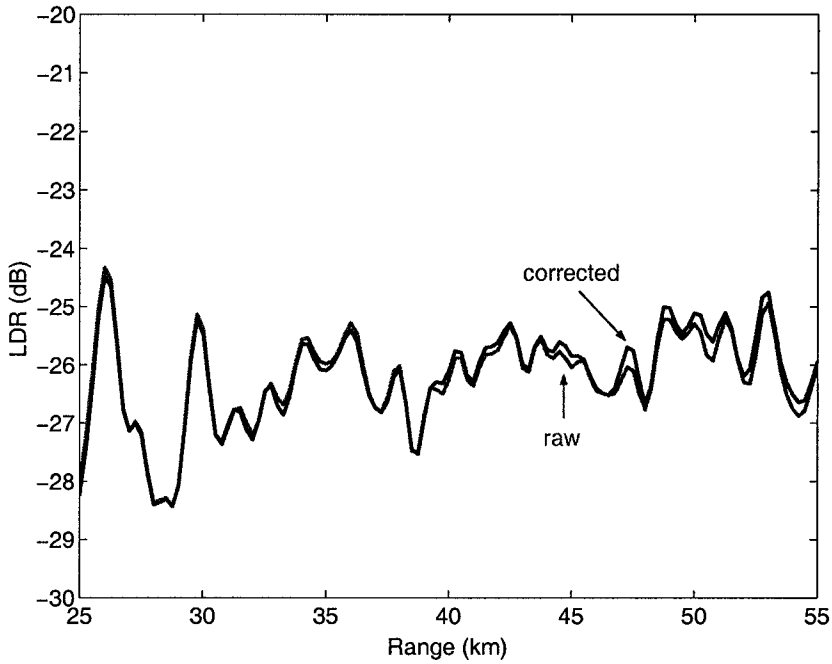

Figure 4.10: The range profile of LDR for the selected ray as in Fig.4.8.

when large Φ_{dp} is accumulated. Therefore, we know for this case that the antenna polarization error must affect the measurement since the non-diagonal propagation can only increase the coefficients.

For this selected volume, the phase offsets are estimated as: $\phi^t_{off} + \phi^r_{off} = 26^o$; $\phi^r_{off} = -80.5^o$. The same criteria are used as in the previous case to select samples to estimate the antenna polarization errors, which turns out to be:

$$\begin{bmatrix} \hat{\tau}_h & \hat{\tau}_v \\ \hat{\epsilon}_h & \hat{\epsilon}_v \end{bmatrix} = \begin{bmatrix} -0.53 & 89.61 \\ 0.08 & 0.25 \end{bmatrix}$$

The estimated errors are applied back to the measured covariance matrices in order to make the corresponding correction. The corrected range profiles are also shown in Fig.4.9 and Fig.4.10 respectively. In comparison, the corrected coefficients behave much more "flat" over that range, and contrary to the previous case, the LDR profile gets raised by a small amount. Again, such phenomenon also exists for the neighboring rays. However, the storm structure does not show local stationary and no reliable statistics are available.

4.2.3 Discussion

The results presented above for two events of rain demonstrate that LDR may get either positive or negative biases along the propagation path if antenna polarization errors exist in the measurement and large Φ_{dp} occurs. For a homogenous medium, however, it can be generally expected that LDR will decrease after the antenna polarization errors are corrected for since the induced cross-polar coupling is "calibrated".

As analyzed in [29], when co-to-cross polar correlation coefficients are large, then the antenna polarization errors probably dominate the measurement. Therefore, data with co-to-cross polar correlation coefficients greater than 0.6 are selected to make the comparison between the "raw" and "corrected" LDR. To ensure proper computation, data quality is also checked and co-polar correlation coefficient is forced to be greater than 0.95. The scatter plot of corrected LDR versus measured LDR is shown in Fig.4.2.3. The correction is obvious but the amount of correction is fairly small.

Since the correction is small, it implies that the antenna of the CSU-CHILL radar has excellent cross-polar performance as shown in Chapter 2. Normally, the antenna cross-polar performance is related to the LDR system limit which is derived from the antenna power patterns which discard all the information on phase terms. In practice, the phase of the error matrix is not known. The approach here is believed to be useful in correcting the measured data using beam-averaged error matrix in homogeneous precipitation.

4.3 Retrieve the Orientation Factors

With antenna polarization errors corrected for, the propagation effect needs to be adjusted next. As explained above, the propagation matrix will be assumed to be diagonal. The differential propagation phase, Φ_{dp}, can be readily obtained

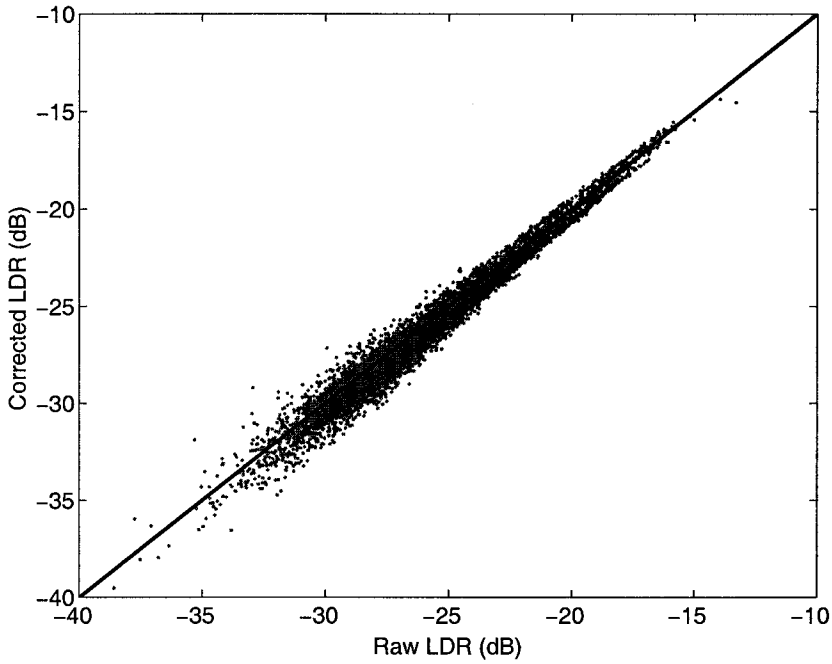

Figure 4.11: The comparison on LDR before and after the antenna polarization errors corrected. The data is collected from case 1.

and "smoothed" by the filtering process, while the fixed linear relationship (3.82) is assumed for the differential attenuation. Then the adjustment for the propagation effect is straightforward, according to (3.86). Finally, the "intrinsic" covariance matrix of the backscattering medium is obtained. The methods to estimate the moments of the orientation distribution can be applied to this estimated "intrinsic" covariance matrix.

For the same ray illustrated in the previous section (see Fig.4.6, the heavy rain case dated on July 21, 2000), the estimated orientation factors β_0 and ρ_4 are plotted respectively in Fig.4.12 and Fig.4.13. In both figures, the results with all three estimation algorithms are presented for comparison, and panel (a) shows the estimation without correcting the antenna polarization errors while panel (b) shows that with such errors corrected. Several points could be drawn from both figures by observation:

1. All the three methods are able to reach similar estimation. The profiles of the estimation are consistent to each other, e.g., the parity of the estimated mean canting angle along range (see Fig.4.12. After the correction for antenna polarization error, the results match much better. This consistency is another implication of the accuracy of the estimation algorithms.

2. The profiles of estimated mean canting angle do approach more closely to zero, especially at large Φ_{dp} segment (between 60 km to 80 km), with the polarization errors corrected for. The estimations from linear covariance matrix by the direct solution and that from circular covariance matrix give non-zero mean canting angle before the correction at that segment.

3. The profiles of estimated orientation dispersion on linear basis and that on circular basis drop by nearly 0.02 at large Φ_{dp} segment before the polarization error correction, likely due to the incurred cross-polar contamination. After polarization errors corrected, however, the profiles rise up.

4. The estimation by optimization method seems to be immune to such errors, especially on the orientation dispersion. The reason probably is the almost-orthogonality of the antenna polarization errors, and as discussed above, the optimization method is valid as long as the transformation matrix is orthogonal.

To further increase the confidence over the estimation algorithms, we can compare the estimations to the range profiles of raw radar variables Z_h and Z_{DR}, as shown in Fig.4.14, as well as the range profile of LDR shown in Fig.4.6. Based on the conventional radar variables, the rain cell around 55 km should have similar physical characteristics as the rain cell around 70 km except in angular resolution. Therefore, the orientation dispersion should maintain in the same level for both locations. The ρ_4 profiles in Fig.4.13 support this hypothesis.

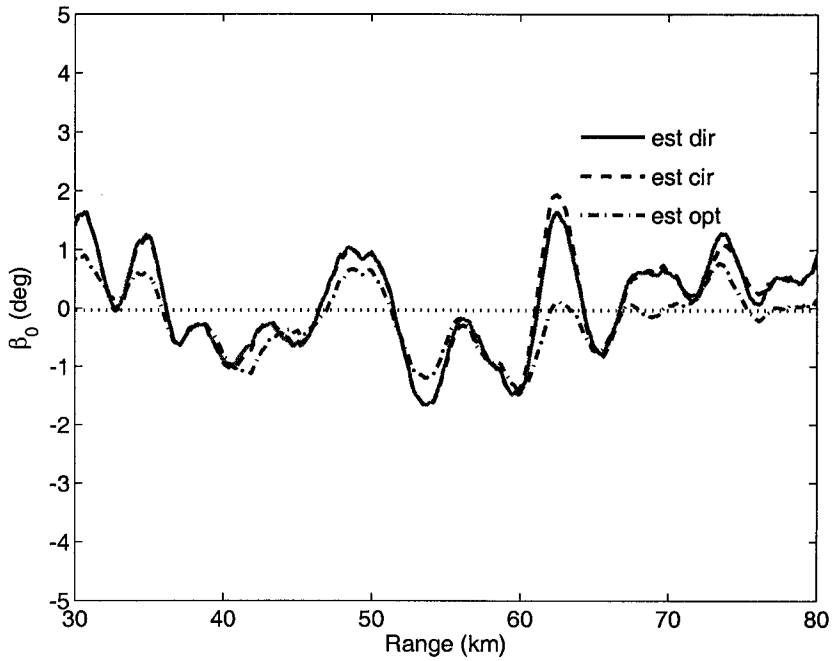

(a) without correction for antenna polarization errors

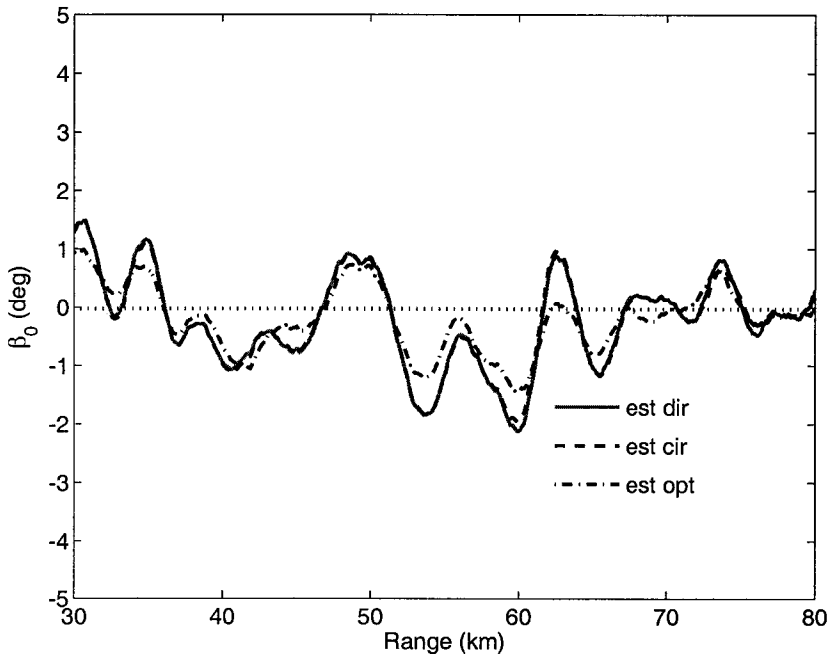

(b) with correction for antenna polarization errors

Figure 4.12: The filtered range profiles of the estimated mean canting angle for the selected ray from radar data on July 21, 2000 00:56 UTC.

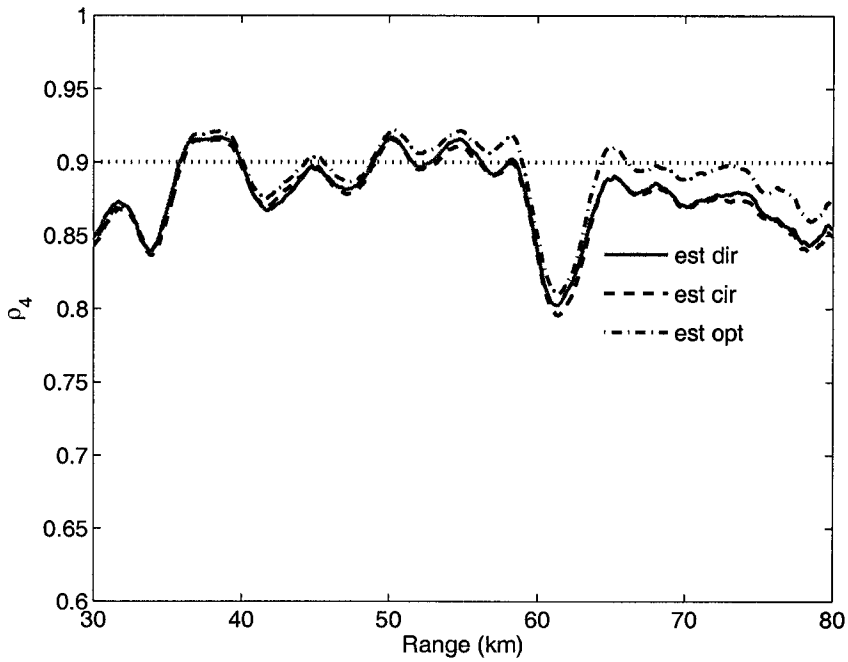

(a) without correction for antenna polarization errors

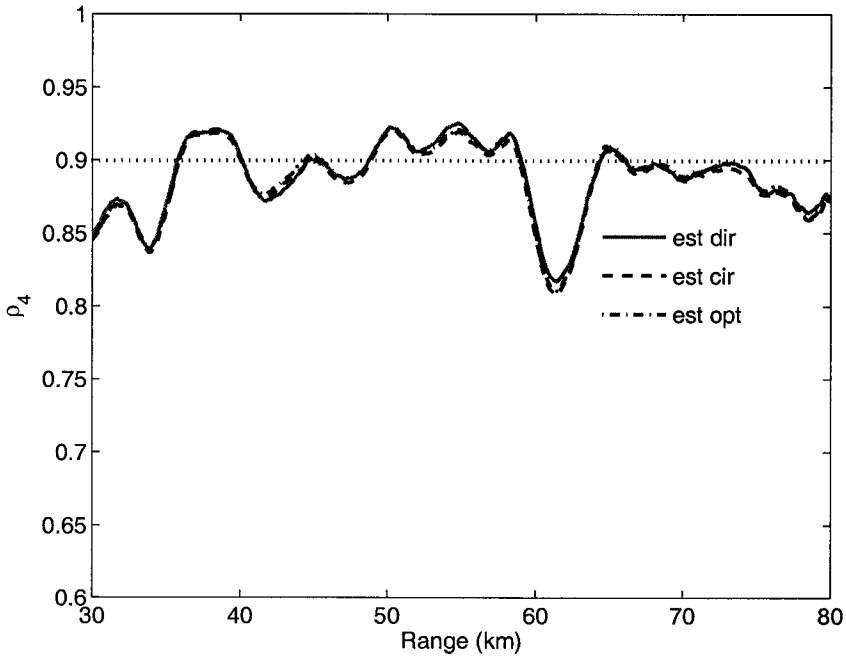

(b) with correction for antenna polarization errors

Figure 4.13: The filtered range profiles of estimated orientation dispersion for the selected ray from radar data on July 21, 2000 00:56 UTC.

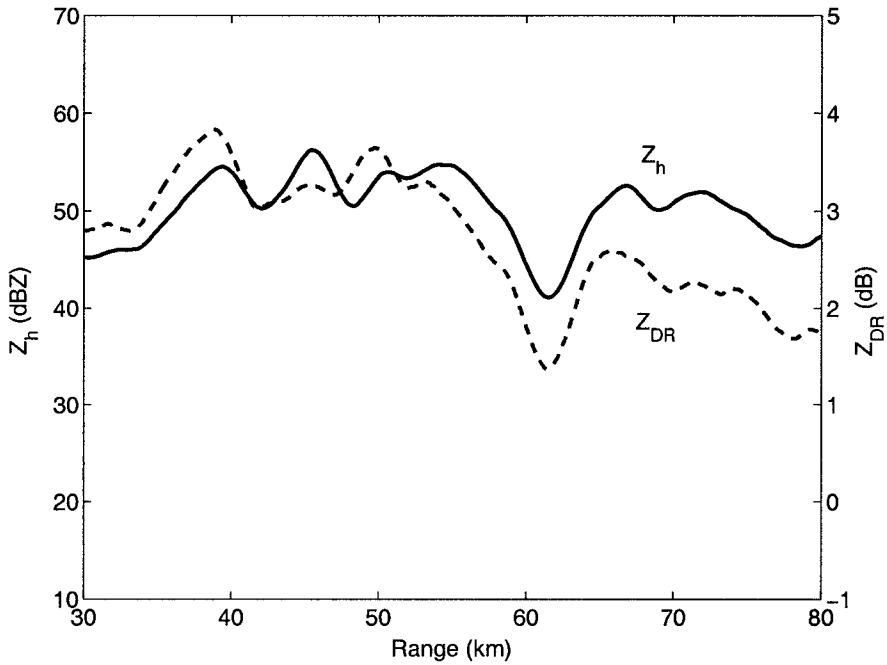

Figure 4.14: The filtered range profiles of the conventional radar variables Z_h and Z_{DR} for the selected ray from radar data on July 21, 2000 00:56 UTC. No attenuation correction is applied.

The statistics of the mean canting angle is likely to further verify the correction for antenna polarization errors. Fig.4.15(a) presents the histogram of estimated mean canting angle over this event. Again in order to ensure the data quality, constraints for "good" data are applied as follows: high SNR (greater than 30 dB), high co-polar correlation (greater than 0.9), and low spatial variation. A direct observation tells that the mean canting angle estimated from the corrected radar measurement is closer to 0 for all the three approaches. Same feature is also presented in the histogram of estimated mean canting angle for another event on July 19, 2000 00:38 UTC (see Fig.4.15(b)).

Both simulation and the results above indicate that the estimation by optimization is better that the other methods in the sense of both insensitivity to probable system errors and low variation. Hereafter, only the estimation by polarization optimization will be presented.

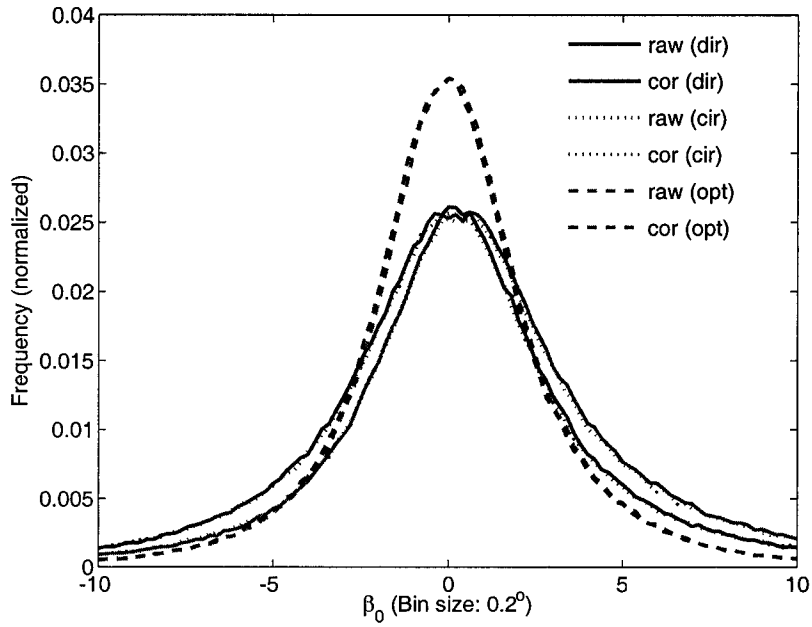

(a) July 21, 2000 00:56 UTC

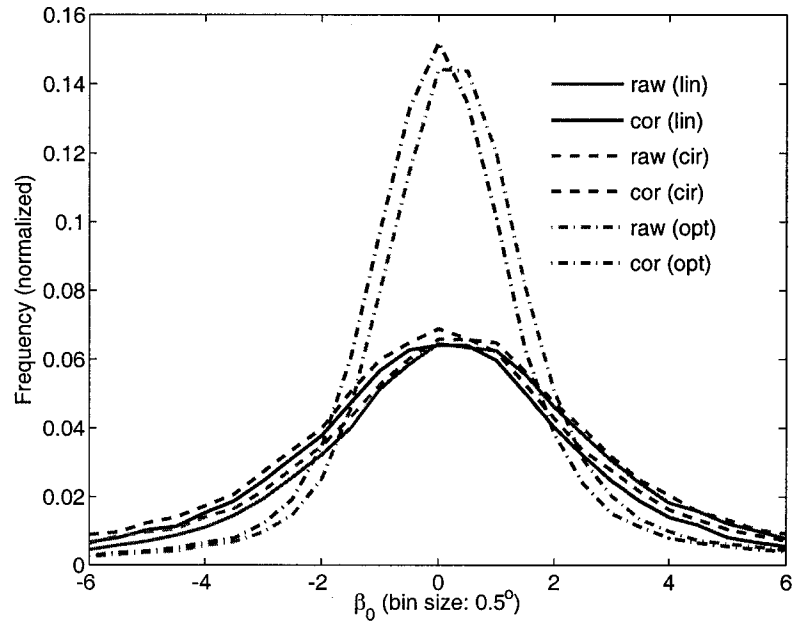

(b) July 19, 2000 00:38 UTC

Figure 4.15: Histogram of the estimated mean canting angle before and after the correction for antenna polarization errors. The dark lines represent for the estimation after correction (cor), while other lines for that before correction (raw); different line styles indicate different estimation methods: that from circular covariance matrix (cir), that from linear covariance matrix by direct solution (dir), and that from optimized polarization (opt).

4.4 Comparison of Polarimetric Variables

Using the polarization basis transformation and the algorithms developed so far, we can derive the corresponding polarimetric radar variables in circular polarization basis such as CDR and $ORTT$, and we can estimate the orientation factors β_0 and ρ_4, in addition to the conventional radar variables in linear polarization basis which are obtained straightforward from measurement. Since the data is basically maneuvered through unitary transformation, no extra new information could be expected. However, the different polarimetric variables do carry information in different manner such that they could present the polarimetric properties in a new perspective. For example, it is well known that the shape factors and orientation factors can be separated in circular polarization basis while the conventional radar variables in linear polarization basis are affected jointly by the shape and orientation distributions. In this section, we will explore the relation among these polarimetric variables with efforts to improve our understanding about the microphysical properties of precipitation.

Because, at this point, we are mainly interested in the backscattering properties, no effort will be made to include K_{dp} for in the comparisons. The candidate polarimetric variables in this study include the radar reflectivity Z_h, the differential reflectivity Z_{DR}, the linear depolarization ratio LDR, the co-polar correlation coefficient ρ_{co}, the circular depolarization ratio CDR, the "apparent degree of orientation" $ORTT$, and the orientation dispersion ρ_4. These variables will be analyzed within the context of "mirror" reflection symmetry. Under this assumption, a hydrometeor particle can be described by its major-axis scattering component S_{11}, minor-axis scattering component S_{22} and orientation angle β. Considering the incoherent average effective in the polarization plane, the state of a precipitation

volume can be determined by the orientation factors:

$$\beta_0 = \langle \beta \rangle \tag{4.14a}$$

$$\rho_4 = \langle \cos 4(\beta - \beta_0) \rangle \tag{4.14b}$$

and the shape factors in the principal plane:

$$Z_1 = \langle |S_{11}|^2 \rangle \tag{4.15a}$$

$$Z_2 = \langle |S_{22}|^2 \rangle \tag{4.15b}$$

$$R + jI = \langle S_{11} S_{22}^* \rangle \tag{4.15c}$$

In the previous chapter, simulation was used to show the dependency of the linear polarimetric variables on canting angle (see Fig.3.4). We can also write the functional forms for the polarimetric covariances in linear or circular basis, according to (3.36) and (3.41), in terms of the orientation factors and shape factors:

$$Z_h = \frac{1}{8}[3(Z_1 + Z_2) + 2R + (Z_1 + Z_2 - 2R)\rho_4 \cos 4\beta_0 + 4(Z_1 - Z_2)\rho_2 \cos 2\beta_0] \tag{4.16a}$$

$$Z_v = \frac{1}{8}[3(Z_1 + Z_2) + 2R + (Z_1 + Z_2 - 2R)\rho_4 \cos 4\beta_0 - 4(Z_1 - Z_2)\rho_2 \cos 2\beta_0] \tag{4.16b}$$

$$Z_{vh} = \frac{1}{8}[(Z_1 + Z_2 - 2R)(1 - \rho_4 \cos 4\beta_0)] \tag{4.16c}$$

$$R_{hv} = \frac{1}{8}[Z_1 + Z_2 + 6R - (Z_1 + Z_2 - 2R)\rho_4 \cos 4\beta_0 + j8I\rho_2 \cos 2\beta_0] \tag{4.16d}$$

$$Z_{rr} = Z_{ll} = \frac{1}{4}(Z_1 + Z_2 - 2R) \tag{4.16e}$$

$$Z_{rl} = \frac{1}{4}(Z_1 + Z_2 + 2R) \tag{4.16f}$$

$$R_{xr} = \frac{1}{4}(Z_1 - Z_2 + j2I)\rho_2 e^{-j2\beta_0} \tag{4.16g}$$

Since only the normalized covariance matrix is of concern, the shape factors can be alternatively described by the "principal" differential reflectivity z and the

"principal" correlation coefficient ρ, which are defined as:

$$z = Z_1/Z_2 \tag{4.17a}$$

$$\rho = (R + jI)/\sqrt{Z_1 Z_2} \tag{4.17b}$$

Then, the polarimetric covariances can be expressed as explicit functions of z, ρ, ρ_4 and β_0. At S-band wavelength the backscattering co-polar differential phase shift δ_{co} is negligibly small [51], hence we can regard the correlation coefficient ρ as a real variable.

Intrinsic Variables	z	ρ	β_0	ρ_4
Default Values	4 dB	0.98	0^o	0.8

Table 4.2: The default values used for the intrinsic shape factors and orientation factors

Fig.4.16 illustrates the change of Z_h with the shape factors z and ρ, as shown in panel (a), and that with the orientation factors β_0 and ρ_4, as shown in panel (b). Panels (c) and (d) demonstrate the impact of coupling ρ_4 and z or ρ. The shape factors are fixed to obtain its relation with orientation factors, or the orientation factors are fixed to obtain its relation with shape factors. Their default values are listed in Table 4.2. From the panel (a), Z_h appears to experience little bias if the particles are well aligned with zero mean canting angle. However, according to panel (b), Z_h can be slightly biased (typically < 1 dB) by randomness of orientation alignment or large mean canting angle. Panel (c) further shows that more oblateness can cause more significant errors especially when their alignment is not perfect. Panel (d) shows that Z_h is less affected by ρ. Although these four panels only display the change on selected planes, they do present the overall dependency jointly on the intrinsic shape and orientation factors. Concerning rain, the drops have good alignment with zero mean canting angle, then the bias on Z_h is only about a few tenths dB, which is not of concern in the estimation of rainfall. For

most other precipitation types, the bias, at most less than 1.5 dB, is negligible for qualitative interpretation of precipitation. Therefore, it is not surprising that Z_h provides a credible dimension for classification. Besides, it is also an important dimension since it carries the size information.

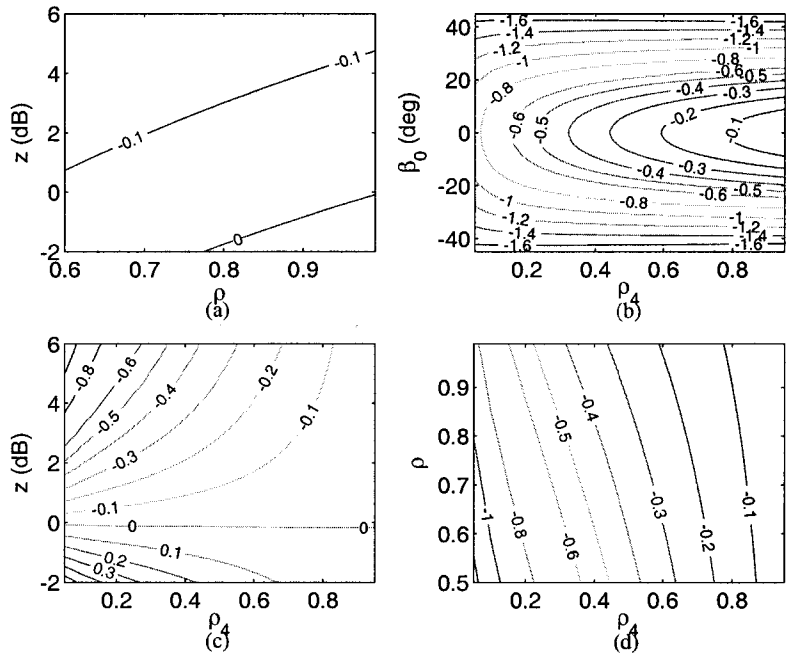

Figure 4.16: The contour of Z_h bias (dBZ) in terms of the intrinsic shape factors and orientation factors.

Fig.4.17 illustrates the change of Z_{DR} with selected pairs of intrinsic shape or orientation factors. Similar to Z_h, panel (a) implies that Z_{DR} experiences little bias if the particles are well aligned with zero mean canting angle. The bias increases to a few tenths of dB which could bias the quantitative estimation of rainfall. Panel (b) shows that both orientation factors can cast big impact on the bias of Z_{DR}, which increases with random orientation or non-zero mean canting angle. Panel (c) shows that the error becomes worse with more oblateness. Panel (d) implies that ρ has little effect on Z_{DR} bias. The demonstrated change looks similar as that for Z_h except that the Z_{DR} bias could be significantly large relative to its dynamic range.

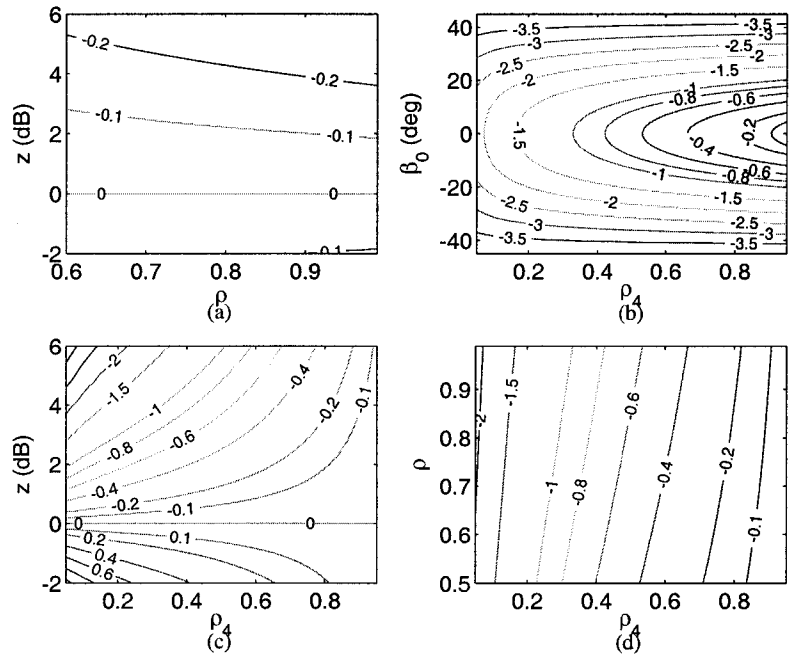

Figure 4.17: Same as Fig.4.16 except for Z_{DR} bias (dB).

Fig.4.18 illustrates the change of ρ_{co} with selected pairs of intrinsic shape or orientation factors. In panel (a)-(c), the bias in ρ_{co} is small relative to its estimation accuracy. However, panel (d) shows that ρ_4 and ρ jointly could bias the correlation coefficient by 0.2 when both ρ_4 and ρ are small. In general, ρ_{co} does not change so significantly that it would affect the microphysical interpretation even though the orientation factors do impact it. In other words, credible information can be drawn based on measured ρ_{co} regardless of orientation distribution.

Fig.4.19 illustrates the change of LDR with selected pairs of intrinsic shape or orientation factors. Panel (a) shows that the measured LDR greatly depends on the shape factors z and ρ even if the drops have good alignment with zero mean canting angle. Panel (b) demonstrates its dependency on the orientation factors. The impact of these physical factors are significant, which means that large ambiguities will exist in the interpretation of LDR. Panel (c) and panel (d) further show how the coupling of shape factors and orientation factors affect LDR.

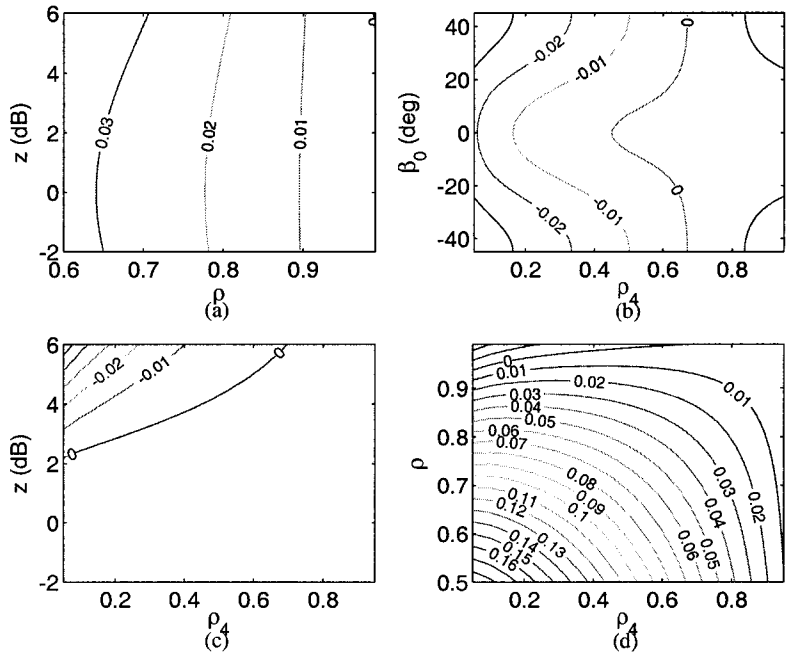

Figure 4.18: Same as Fig.4.16 except for ρ_{co} error.

Large LDR could be attributed to oblateness, low correlation, random alignment and/or non-zero mean canting angle.

Concerning the circular polarimetric variables, CDR and $ORTT/\rho_2$ are purely dependent on the shape factors. Such isolation from orientation distribution appears to be preferable from a classification viewpoint. Since both CDR and $ORTT/\rho_2$ are only dependent on z and ρ, their functional forms can be easily and clearly illustrated as shown in Fig.4.20, where ρ acts as a parameter and the curves show their relations with respect to z. It could be determined from Fig.4.20 that ambiguity still exists on both circular variables to interpret the values in terms of particle shapes. Based on the illustrated relation between CDR and z, we see that CDR is strongly correlated with z if ρ is very large, but such correlation become weak quickly as ρ decreases. The relation between $ORTT/\rho_2$ and z behaves in the other direction. Therefore, $ORTT/\rho_2$ and CDR probably can bear similar information as Z_{DR} with the advantage that they are immune to orientation distribution.

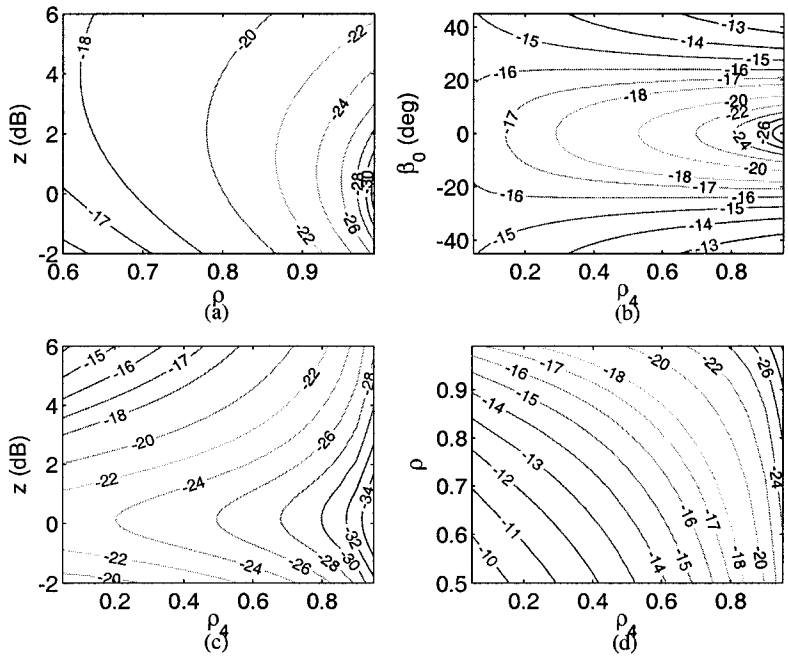

Figure 4.19: Same as Fig.4.16 except for LDR (dB).

In conclusion, we should always take Z_h as one dimension in classification. When β_0 is significantly different from zero, or the orientation is nearly isotropic, Z_h can be lower than the intrinsic value Z_1 by a couple of dB. The coefficient ρ_{co} has little dependency on the orientation distribution as long as its intrinsic value is high. When both ρ and ρ_4 are fairly small, ρ_{co} can be increased by less than 20%, which is not significant enough to misinterpret the precipitation types. In application, ρ_{co} is an important indicator of shape variation or mixture of precipitation types. The orientation factors can affect Z_{DR} to a large extent. Especially, for particles with large oblateness, Z_{DR} can be lower by several dB when β_0 is far off from zero or ρ_4 is low. In contrast, the circular polarimetric variables CDR and $ORTT/\rho_2$ are only dependent on the intrinsic shape factors; however, the strong impact of ρ on them limit their usage to represent the intrinsic value of z. As we will see later, the mean canting angle is always close to zero for most precipitation targets, which reduces the benefit of using CDR and $ORTT/\rho_2$

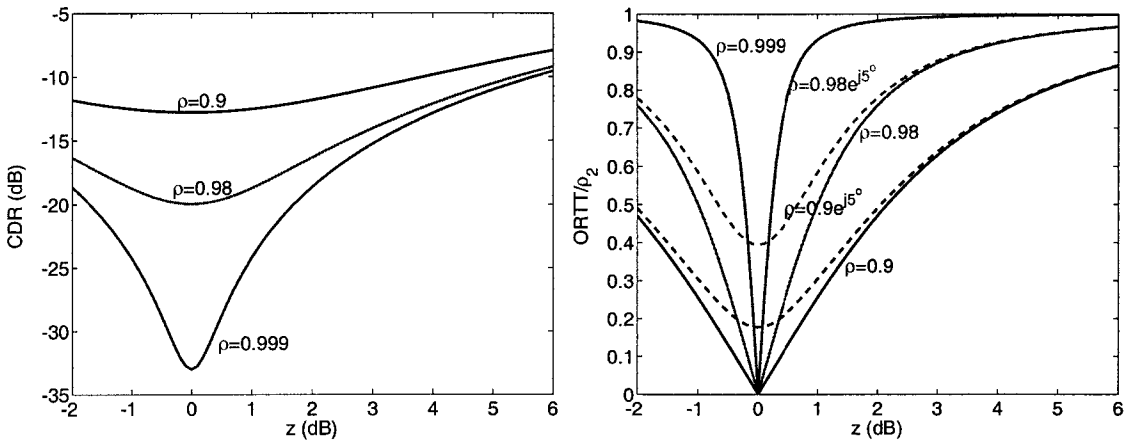

(a) CDR (b) $ORTT/\rho_2$

Figure 4.20: The dependencies of (a) CDR and (b) $ORTT/\rho_2$ on the intrinsic shape factors z and ρ.

in classification. However, LDR depends on all the intrinsic factors such as z, ρ, β_0 and ρ_4. For non-spherical particles, LDR increases from $-\infty$ quickly if ρ is low, β_0 off zero, or ρ_4 small, which means that significant ambiguity can be expected in interpreting the LDR data.

4.5 Case Studies

4.5.1 Rain

Rain is the primary observation in radar meteorology and the shape and orientation of rain drops have been well understood. Its equilibrium shape can be described by an oblate spheroid with well-defined orientation alignment [9], with which the estimation algorithms for orientation factors can be applied. The mean axis ratio, a figure of oblateness, has been shown to be related to the drop size by several function models. Now we can study the features of orientation distribution related to the drop size. The radar data are from the event on July 21 2000 (see Fig.4.3) and from another event on June 11 2000 (as shown in Fig.4.21).

To ensure high data quality and pure rain, the following criteria will be enforced: altitude less than 1 km (such that rain drops have been fully melted and

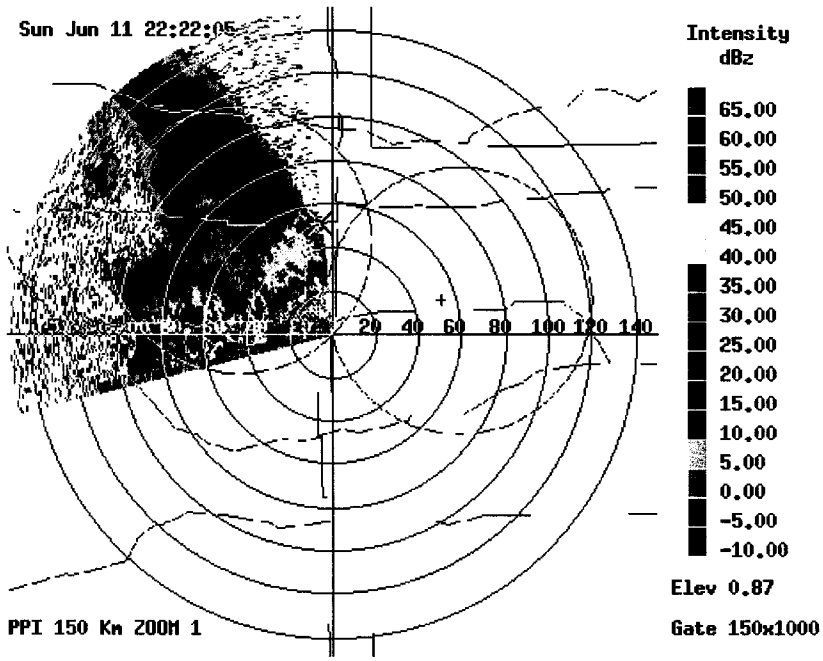

Figure 4.21: A PPI scan of Z_h (dBZ) at low elevation angle for the heavy rain case on June 11, 2000.

formed with their equilibrium shape), co-polar correlation coefficient larger than 0.96 (in effort to avoid mixed precipitation types), range less than 60 km (to ensure good spatial resolution). Moreover, at the low altitudes, the radar echo could be contaminated with non-hydrometeor targets such as clutter. To avoid clutter, we also force the range to be larger than 20 km. The last criterion is that the estimated mean canting angle fall within $\pm 20^o$, which is based on the assumption that the mean canting angle of rain drops should not vary much from zero. To see this point, we plot the samples with $|\beta_0| > 20^o$ in Fig.4.22 from a PPI scan in the lowest elevation angle for both rain events. It is shown that these samples coincide with suspicious clutter or regions that are likely to be corrupted with gradient errors (due to antenna).

The relation between Z_h and Z_{DR} is plotted in Fig.4.23(a), where the mark 'x' and 'o' indicate, respectively for the two events, the median value of Z_{DR} falling inside the individual bin of Z_h, and the upper bar represents for the first quartile

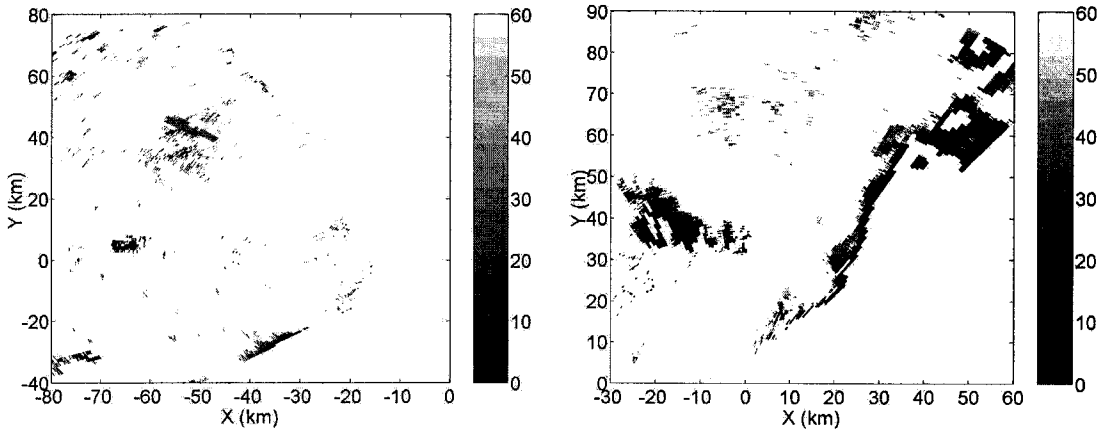

(a) Case: June 11, 2000 (b) Case: July 21, 2000

Figure 4.22: PPI plots of Z_h (dBZ) for the data samples with $|\beta_0| > 20^o$.

while the lower bar for the last quartile. From Fig.4.23(b), on average the LDR decreases with increasing Z_{DR} but stabilizes beyond Z_{DR} of 3 dB. In panel (c), the ρ_4 increases with Z_{DR} which implies that larger drops are more oriented as compared with smaller ones. In terms of drop oscillation it means that larger drops are less susceptible to transverse oscillations as compared to smaller drops. The larger LDR values for smaller Z_{DR} may also support the hypothesis of larger transverse oscillations for smaller drops. To further explore the coupling between shape and orientation factors for LDR, Fig.4.24 shows the scatter plot of LDR versus ρ_4 with Z_{DR} as a grey-scale overlay. The general trend is for LDR to decrease with increasing ρ_4 but there is also a strong dependence on Z_{DR}.

The observables Z_h and Z_{DR} can be quantitatively used to estimate the rainfall rate. With the orientation factors estimated, we can take advantage of the direct solution in linear basis (as shown from (3.47) through (3.50)) to estimate their intrinsic values. The histogram of obtained Z_h bias $(Z_h - Z_1)$ and Z_{DR} bias $(Z_{DR} - 10\log_{10} z)$ is given in Fig.4.25. Based on panel (a), Z_h shows little bias due to orientation, mostly less than 0.1 dBZ. However, Z_{DR} could be biased a little more – there are a significant amount of samples with biases between 0.05 dB to 0.15

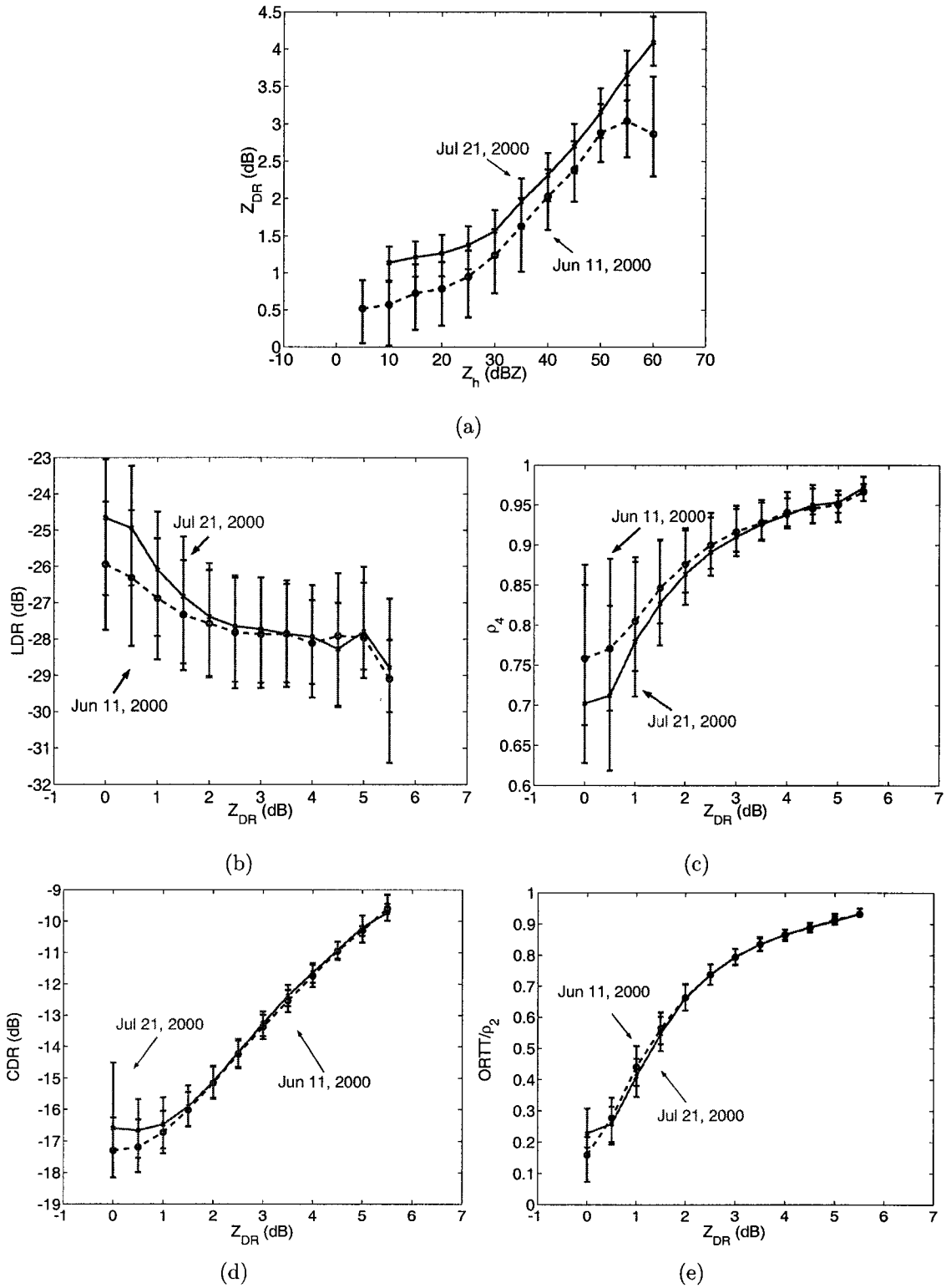

Figure 4.23: The statistic relations among the conventional linear polarimetric variables and the derived polarimetric variables. The symbol 'x' and 'o' mark the median values, the upper bar represents for the first quartile, and the lower bar for the last quartile.

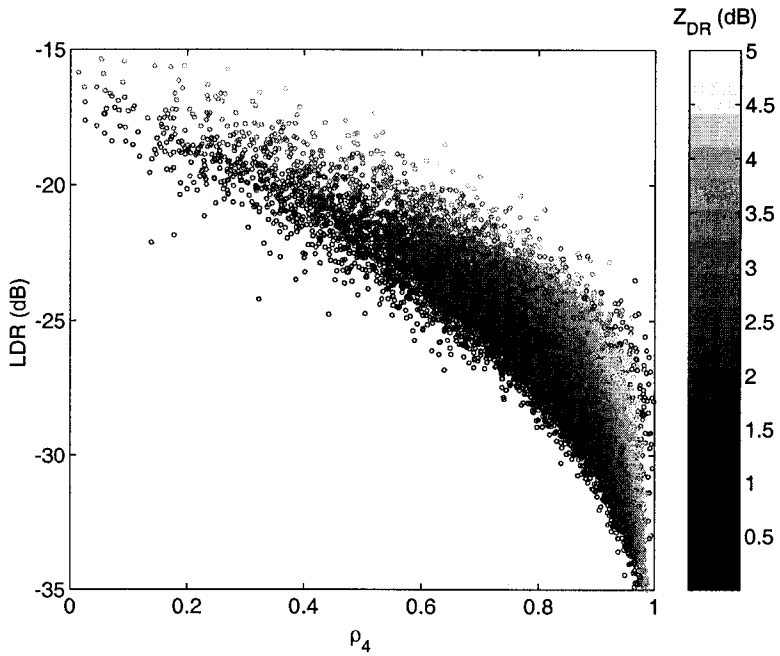

Figure 4.24: The scatter plot between LDR and ρ_4 with Z_{DR} (dB) as parameter indicated in gray scale. Data samples are collected from the event on July 21, 2000.

dB. If the rainfall estimation is based on formula [52],

$$R(Z_h, Z_{DR}) = 6.7 \times 10^{-3} \times 10^{0.1*0.927*Z_h} \times 10^{-0.1*3.433*Z_{DR}} \tag{4.18}$$

the biases will result in estimation error on rainfall rate, as illustrated in the panel (c). Due to the negative bias on Z_{DR}, positive bias shows up on the rainfall estimation by (4.18). The estimation error is not significant though, mostly within 10% as shown in the histogram. Therefore, the estimation of orientation factors can potentially help to fine tune the rainfall estimation, even though the adjustment may not be much for most rain events.

Since the bias on Z_{DR} is usually small for rain, the measured Z_{DR} can be regarded as its intrinsic value and hence can act as a dimension of oblateness. The relations between CDR, $ORTT/\rho_2$ and Z_{DR} are illustrated in Fig.4.23(d) and Fig.4.23(e) respectively. Both plots describe a strong correlation, which is

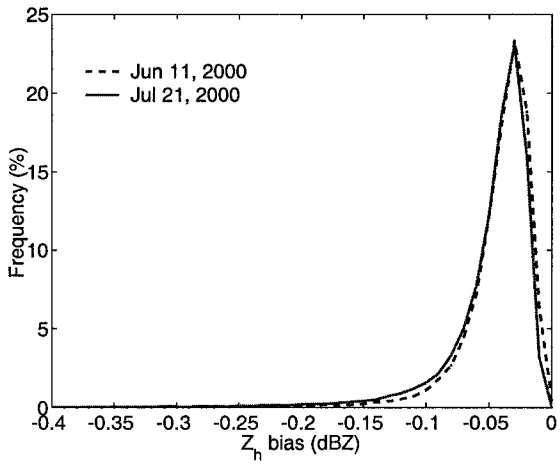

(a) Histogram of Z_h bias (dBZ)

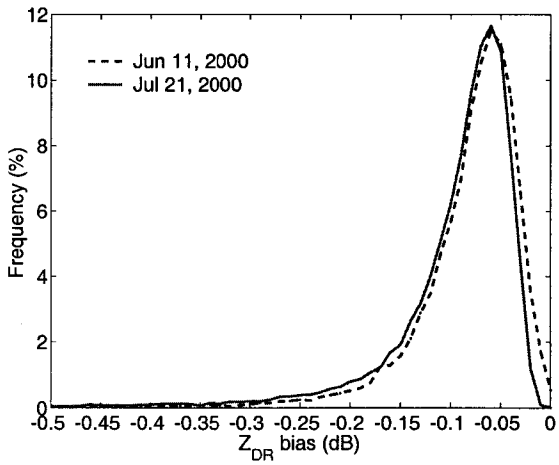

(b) Histogram of Z_{DR} bias

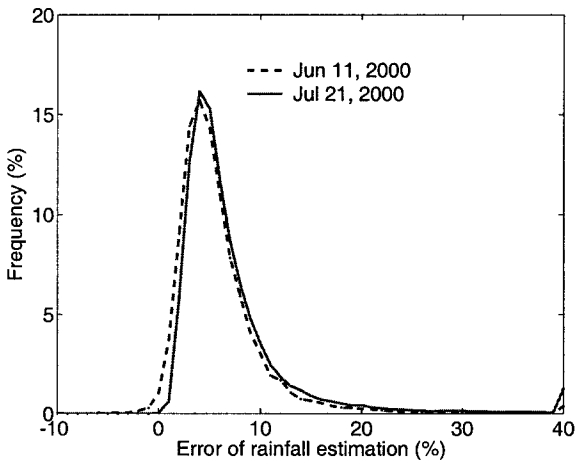

(c) Histogram of the incurred estimation error of rainfall rate

Figure 4.25: The histogram of biases due to orientation distribution and the incurred estimation error of rainfall rate.

consistent with the theoretical curves as shown in Fig.4.20. When Z_{DR} is large, both CDR and $ORTT/\rho_2$ follow as functions of Z_{DR} with small dispersion. Only when Z_{DR} is smaller than 1 dB, CDR and $ORTT/\rho_2$ can distribute over a limited range depending on the value of ρ_{co} (or the intrinsic counterpart ρ).

4.5.2 Ice Particles

Fig.4.26 presents a composite RHI scan at 00:53 UTC by the CSU-CHILL radar for the storm event on July 21, 2000. The contours of Z_h are overlaid on the plots, from which two strong storm cells can be observed at 25 km and 45 km along range, with Z_h greater than 40 dBZ. Below 2 km in altitude (AGL), Z_h for the two cells increases to more than 50 dBZ and Z_{DR} shows significant positive value as large as 4 dB. These signatures are representative of large size oblate drops. From panel (b,d), fairly low values can be read from the corresponding signature LDR and ρ_{xh}, which implies that the particles experience light oscillation with zero mean canting angle. Meanwhile, ρ_{co} is about 0.97 in the close-in cell and even lower in the further cell, therefore, the shape of oblate drops may have some degree of variation or, as a special case, there may exist rain/hail mixture. Between 2 km and 3 km in altitude, the melting level can be clearly observed based on high LDR (around -20 dB) and relatively low ρ_{co} (around 0.94). Above the melting level, the hydrometeor particles are in ice phase, where Z_{DR} is near zero. The LDR is almost at the same level as that below the melting level, and ρ_{co} shows higher values around 0.98. On the other hand, the coefficient ρ_{xh} stays below 0.3. Therefore, the hydrometeor particles at this level, likely graupel, distributed with highly identical shapes (e.g., conical).

From the constructed linear covariance matrix, the corresponding circular variables can be readily derived and the orientation factors are estimated through polarization optimization after the slight antenna polarization errors and the propagation effects are corrected for. These variables are presented in Fig.4.27. Within

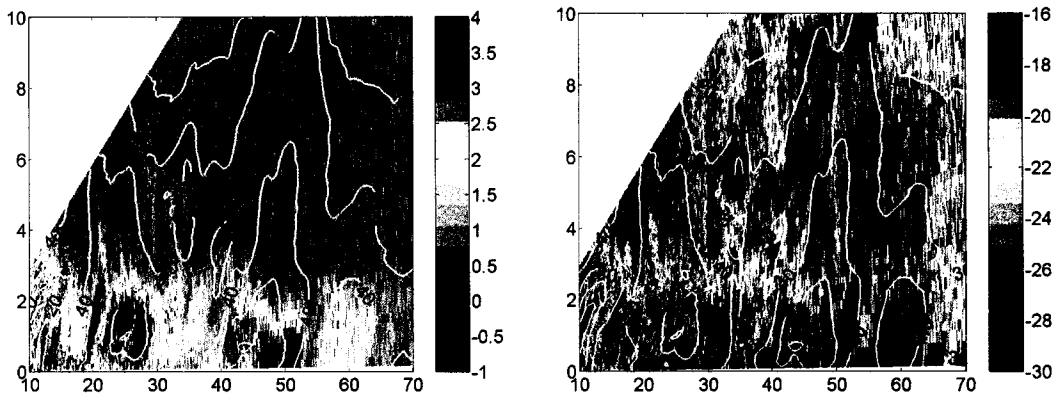

(a) Z_{DR} (dB)

(b) LDR (dB)

(c) ρ_{co}

(d) ρ_{xh}

Figure 4.26: Composite RHI scan with radar variables in the linear H/V basis for a heavy rain event on July 21, 2000 00:53 UTC. The X-axis is the ground distance (km) from the radar, and the Y-axis is the altitude (km) above ground level (AGL).

the two rain cells, CDR of -10 dB can be observed from the RHI plot in panel (a) that mainly attributes to the high oblateness of rain drops (in accordance with large Z_{DR}). The mean canting angle is estimated within $\pm 2^o$ for this region. Concerning the orientation dispersion ρ_4, it is higher than 0.9 in both cells, implying that the raindrops at low altitudes are oriented with a narrow distribution. In melting level, since melting occurs and mixed type precipitation exists in this phase, the particles do not possess well-defined symmetric axes and ρ_4 drops significantly. Moving to higher altitude above the rain cells, CDR gradually drops to -20 dB, while ρ_4 increases up to 0.8. The orientation distribution becomes broader, while the estimated mean canting angle is still concentrated near zero. The $ORTT$ combines the shape factors and the orientation dispersion in such a way that either nearly spherical particles or isotropic-like orientation could lead to its small readings. Such signature is very clear in panel (b), where $ORTT$ at low altitude is as high as 0.8 to 0.9 for raindrops while at high altitude is as low as 0.3.

On June 04, 2001, a severe hail event occurred in the area of Denver International Airport (DIA) with damaging hailstones reported. A composite RHI scan by the CSU-CHILL radar is given in Fig.4.28 with the conventional linear radar variables. At the ground distance of 62 km, the radar reflectivity Z_h reaches 65 dB, and over this region negative Z_{DR} can be observed, both of which together imply existence of large wet hail. The high reflectivity extends up to 5 km in altitude and negative Z_{DR} column can be observed. This hypothesis of wet hail could be supported from high depolarization (LDR) and fairly low co-polar correlation coefficient (ρ_{co}). Those signatures suggest that the hydrometeors in this region are mainly composed of large hail stones coated with water. At closer range ($\sim$ 57-60 km), the reflectivity is still high, but Z_{DR} becomes closer to zero an altitudes above 1 km. The LDR experiences a significant drop to around -23 dB while the co-polar correlation increases to above 0.97. The hail stones in this region may be

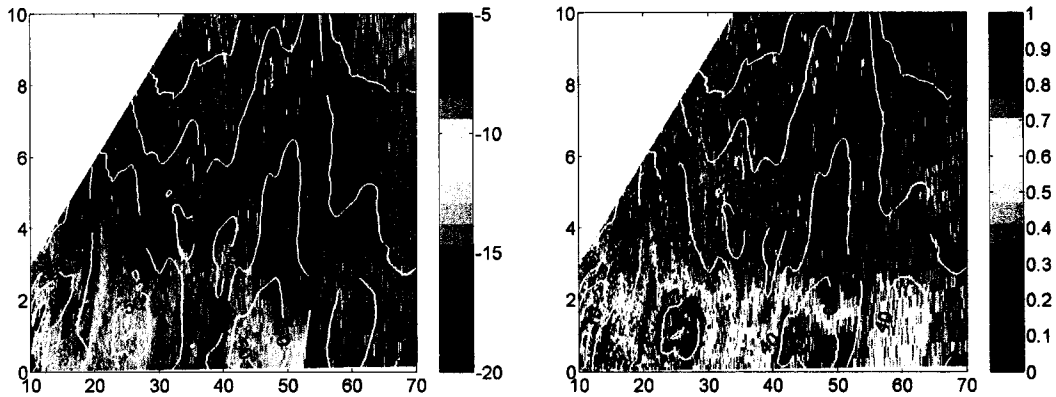

(a) CDR (dB) (b) $ORTT$

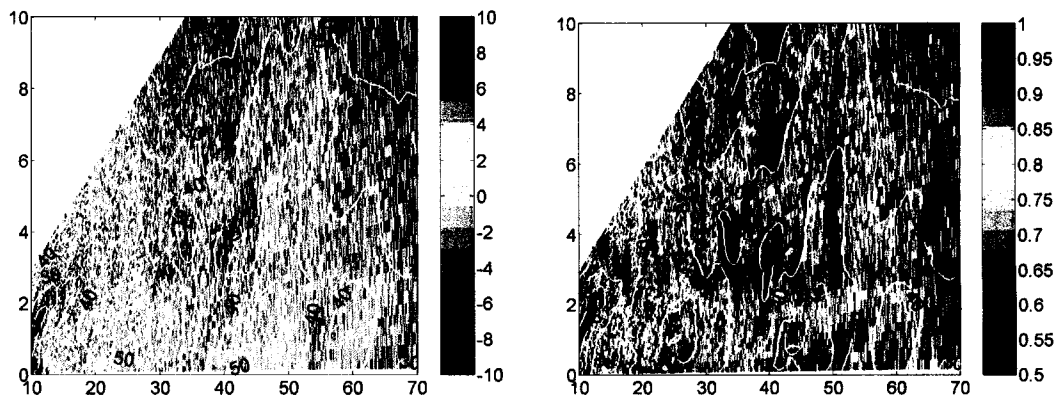

(c) $\beta_0(deg)$ (d) ρ_4

Figure 4.27: Same as Fig.4.26 except with RHI plots of derived radar variables in the circular polarization basis and estimated orientation factors.

more 'pure' and closer to sphere in shape. It is also interesting to note that at the top of the storm core (7-8 km AGL) above the ground range of 61 km, where Z_h is between 30 and 40 dBZ, the co-to-cross correlation coefficient ρ_{xh} increases up to 0.6, which is possible when the mean canting angle is not zero. It indicates that this region probably is composed of oriented ice crystals.

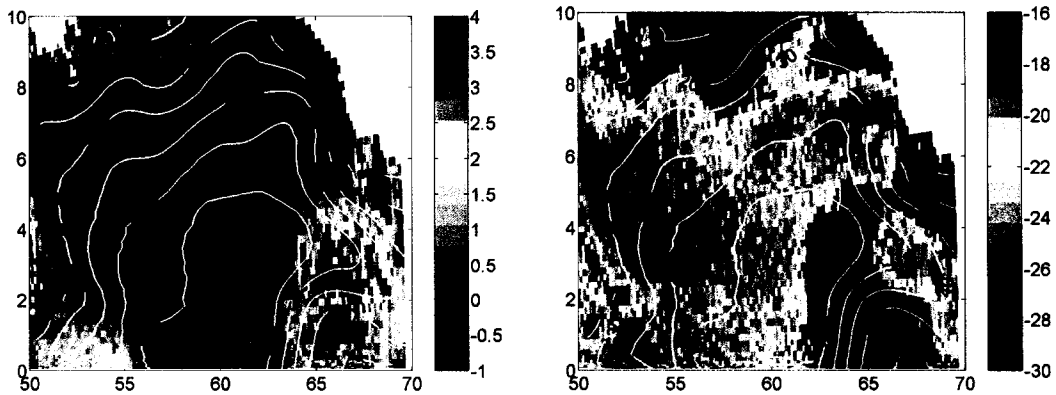

(a) Z_{DR} (dB)

(b) LDR (dB)

(c) ρ_{co}

(d) ρ_{xh}

Figure 4.28: Same as Fig.4.26 except depicting for a severe hail storm on June 04, 2001 21:12 UTC.

Such explanation can be enhanced by the derived radar variables as shown in Fig.4.29 where the RHI scan of circular radar variables and estimated orientation factors are plotted. At the range of 62 km, large circular depolarization (CDR

value as high as -8 dB) shows that the shape of particles is very irregular (compared to sphere). At the same time ρ_4 is low which means the particles may be tumbling or may not possess well-defined symmetric axes. Besides, the estimated β_0 distributes over a large range, within $\pm 10^o$. Moving to the observation closer to radar, the derived CDR falls to -17 dB. Meanwhile, the estimated ρ_4 increases to about 0.6. Therefore, the hail stones in this region seem to be more spherical and the orientation becomes much more steady. Note that the co-to-cross correlation coefficients are very low in both regions. At the top of storm core (7-8 km AGL near 61 km range), the mean canting angle is discernably off zero by more than 10 degree at some locations, which gives a quantitative description of orientation distribution for the hypothesized aligned ice crystals. Again, $ORTT$ combines the effect of oblateness, orientation dispersion, and shape variation. For this hail storm, it is generally low and provides little discrimination over different hail types as abstracted from other signatures.

The descriptive analysis above is consistent either based on the conventional linear polarimetric variables or based on the derived radar variables. It shows that the "symmetric" model for hydrometeor particles and the estimation algorithms for orientation distribution actually still work in the ice phase of precipitation. When studying the properties of the hail storm, the derived CDR and estimated ρ_4 can even provide supplemental information to improve our microphysical understanding. In order to obtain a quantitative comparison over these variables, we select the data samples from several vertical columns and compare the variables of interest by scatter plots, as shown in Fig.4.30. The three columns separately correspond to the close-in strong rain cell (presented on above) and the weak rain cell at range of 60 km from the 21 July 2000 case, and the hail shaft ($\sim$ 60-62 in range) from the 4 June 2001 case. Different markers are used to label different columns while the gray level is used to represent the altitude (AGL).

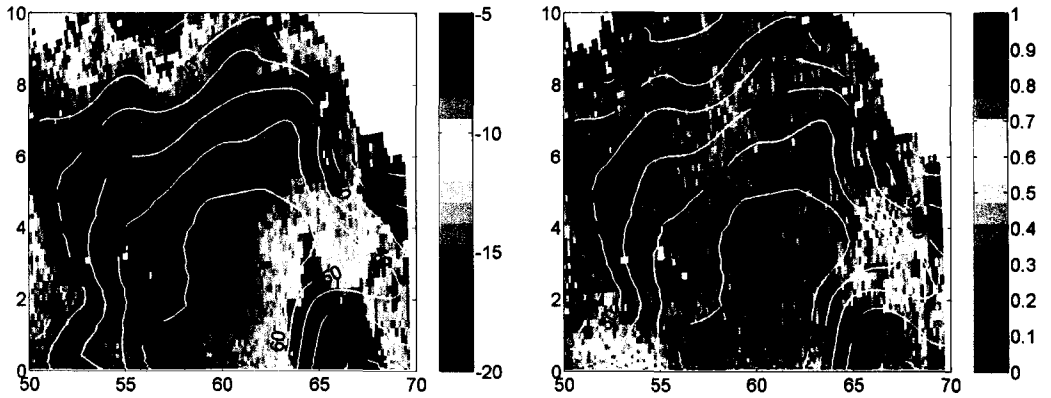

(a) CDR (dB) (b) $ORTT$

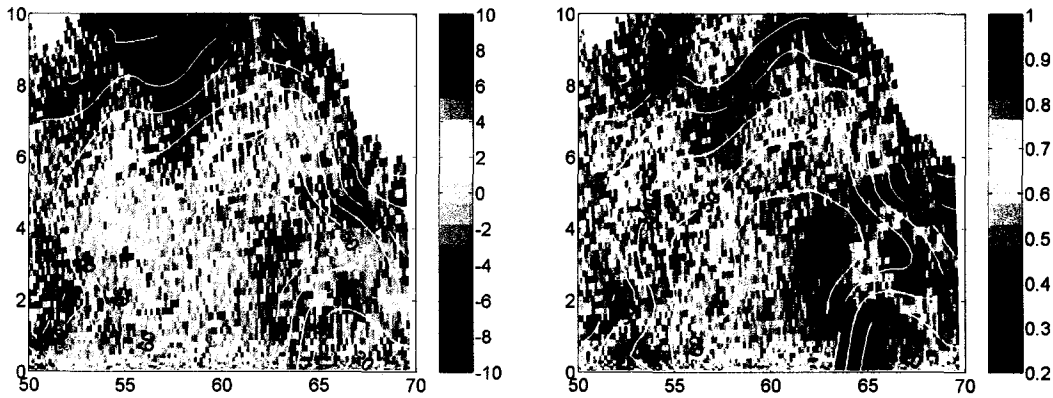

(c) $\beta_0(^o)$ (d) ρ_4

Figure 4.29: Same as Fig.4.28 except with RHI plots of derived radar variables in the circular polarization basis and estimated orientation factors.

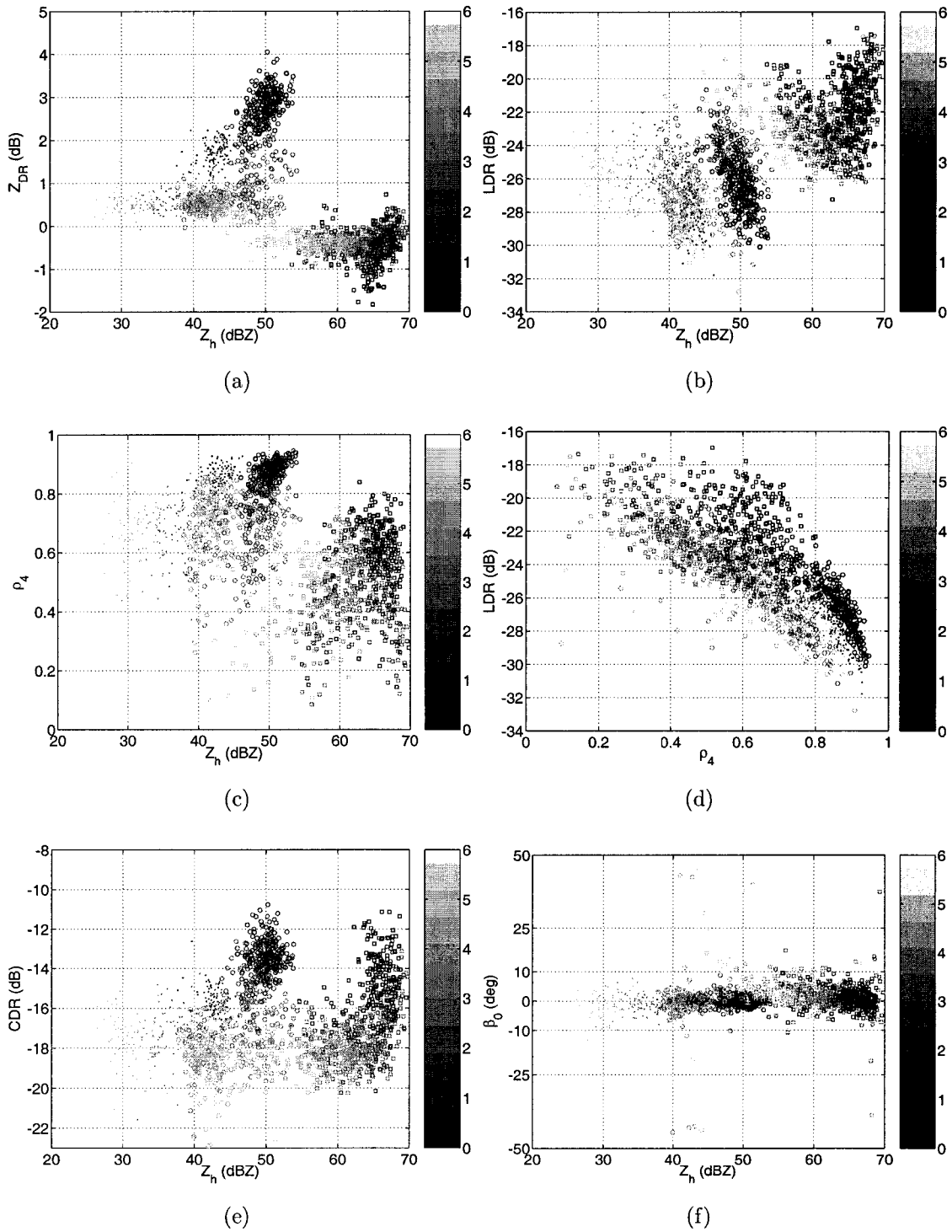

Figure 4.30: The scatter plots among the conventional linear polarimetric variables and the derived polarimetric variables. The altitude is represented by the gray scale; the precipitation samples for heavy rain, medium rain and hail are labelled by marks 'circle', 'dot', and 'square', respectively.

Shown in panel (a) is the scatter plot between Z_h and Z_{DR} for the there precipitation types. The dark shaded markers stand for the resolution volumes at low altitudes. Again, for rain, Z_{DR} is proportionally related to Z_h. The lighter markers illustrate that Z_{DR} for the rain-generating ice particles, independent of Z_h, stays at near constant level. In the melting layer, Z_{DR} varies over a large range as indicated by gray shaded samples. For hail, Z_{DR} does not show strong relation with Z_h. Compared to the near constant values at high altitudes, Z_{DR} falls into a broader range at low altitudes, from -1.5 dB to 0.5 dB. The coupling between Z_{DR} and Z_h demonstrate that this pair of polarimetric variables is able to nicely discriminate between ice particles and rain drops. This rule is well established by many previous studies as summarized by Bringi and Chandrasekar in [18].

The scatter plot $LDR \sim Z_h$ is shown in panel (b). For the medium rain, LDR mostly ranges from -30 dB to -26 dB, and increases by 2 dB for the ice phase at high altitudes. As for heavy rain, LDR distributes from -29 dB to -24 dB, while it is even slightly lower for the ice particles aloft, from -30 dB to -25 dB. Similarly, such change can be observed for the hail. At low altitude, LDR for hail varies from -24 dB up to -18 dB but stays at a lower range aloft (-25 dB $\sim$ -22 dB). Generally, this increase in LDR with decreasing height is attributed to change in dielectric constant. Next go to panel (c) to observe the scatter plot $\rho_4 \sim Z_h$. For medium rain, ρ_4 is estimated larger than 0.8; the estimate of ρ_4 for the corresponding ice particles is well below 0.8. Concerning heavy rain and the particles aloft, ρ_4 is still higher than 0.8 at low altitude while mostly decreasing to 0.6$\sim$0.85 at high altitude. Lower ρ_4 can be read for hail: 0.4 $\sim$ 0.7 at low altitude and 0.3 $\sim$ 0.6 mostly at high altitude. Therefore, basically, the ice particles aloft are distributed more randomly in orientation. The estimated ρ_4 generally presents a better discrimination of particle types. For the rain event, LDR has values from -30 dB to -25 dB, while ρ_4 presents a boundary between ice and water. For the

hail storm, the boundary is not clear partly due to melting, however, still most of LDR ranges from -24 dB to -19 dB but ρ_4 is smaller for the samples at higher altitude (light markers always located on the left for same LDR). Of course, given ρ_4, LDR varies according to oblateness and shape variation (as well as ϵ_r). We believe that the estimated ρ_4 more closely represents the information on orientation distribution.

The scatter plot $CDR \sim Z_h$ in panel (e) looks similar to that of $Z_{DR} \sim Z_h$ for rain drops. Attention should be placed on the cluster of hail. The hail aloft has a much lower reading for CDR than hail near the ground. This could be attributed to melting and the increase in ϵ_r due to wet hail. For the rain case, the ice particles above the heavy rain have smaller CDR compared to those above the medium rain. Also, the corresponding ρ_4 is up to 0.85 indicating that the ice particles are closer to sphere and they are better aligned in orientation (e.g., conical graupel). On the other hand, the ice particles above the medium rain have higher CDR (by several dB), and lower ρ_4 indicating more irregularly shaped ice particles. It seems that CDR could provide better interpretation over particle shapes combining other polarimetric signatures, but it is not sufficient by itself. One disadvantage of CDR is that CDR cannot distinguish between prolate-like or oblate-like particles. Since $ORTT$ is known to be related to other factors, it is not presented. Generally it is below 0.4 for all the ice particles.

The scatter plot $\beta_0 \sim Z_h$ is presented in panel (f). For most samples, β_0 is estimated within $\pm 10^o$ with a nearly zero mean. It clusters more tightly around zero for rain drops. This finding to some extent defends the hybrid mode polarimetric operation [53].

In summary, the estimated ρ_4 and derived CDR provides more insight for interpreting the polarimetric measurement obtained in the linear H/V basis. Especially, the estimated ρ_4 can be used as a substitute for LDR to better represent

the orientation. Certainly all polarimetric signatures need to be jointly considered in precipitation type classification, which suggests no improvement of classification performance. However, by solving the mutual correlation among polarimetric signatures, the classification algorithm could be get more simplified and hence improved. Moreover, CDR might be better than Z_{DR} in representation of shape distribution, but its proper application requires the support from other signatures, say ρ_4 and ρ_{co}. Note that ρ_{co} as an important dimension is well known to give information on particle mixtures. While hydrometeor classification is an important application, its development will not be covered in this dissertation.

4.6 Summary

Calibration over both power and phase of the radar measurement is required to construct the polarimetric covariance matrix. It is particularly important to remove the differential phase offsets between two polarization channels for the sake of orientation factor estimation. A robust phase filtering scheme was presented based on directional statistics to help determine the phase offsets in the radar system.

Two rain events were studied to examine the estimation algorithm for antenna polarization errors. Apparent change of the co-to-cross correlation coefficients was observed for both cases with large accumulated Φ_{dp}. Assuming the mean canting angle for rain is close to zero, the trends of the coefficients could be attributed to antenna polarization errors. The estimation algorithm was then applied to selected set of samples for which the mean canting angle is most likely to be zero and Φ_{dp} is small to suppress the possible propagation effect. The obtained error matrix was used to correct the covariance matrix for the whole volume. After the correction, "flat" profiles on co-to-cross correlation coefficients were examined compared to their original profiles.

The orientation factors were retrieved using three estimation approaches. The results show that the optimization approach leads to estimate of β_0 with smaller variation and robust estimation of ρ_4. The estimated β_0 has small bias off zero before adjustment for antenna polarization errors. After such correction, its mean is closer to 0. Furthermore, the results by different approaches agree well with each other after the correction but not before the correction. These observations further validate the estimation method for antenna polarization errors and the assumption of zero mean canting angle at least for these two cases.

The basic assumption is that hydrometeors can be described by independent size, shape and orientation distribution. For different polarimetric variables, the impact of shape factors and orientation factors was described and compared. It was found that Z_h and ρ_{co} are relatively less affected by the orientation factors for precipitation observation, but Z_{DR} and LDR can be significantly biased by orientation factors. Especially, LDR is almost equally related to both shape and orientation factors, which implies there exists much ambiguity in microphysical interpretation using LDR. Compared to Z_{DR}, CDR and $ORTT/\rho_2$ are well known to be independent of orientation factors, however both of them have strong dependency on the co-polar correlations which seems to limit their advantage.

Application of the derived circular polarimetric variables and estimated orientation factors are sought through case studies. The quantitative rainfall estimation can benefit from the estimation of orientation factors. The isolation of orientation factors means the availability of intrinsic shape variables, which will result in fine tuned estimation of rainfall rate. These derived radar variables show consistent explanation compared to the standard linear variables even for the ice phase precipitation. On some occasion, they may also help us to understand the microphysical features of precipitation since all the linear polarimetric variables Z_h, Z_{DR}, ρ_{co} and LDR depend on both shape factors and orientation factors in a complicated

manner. In particular, compared to LDR, the estimated ρ_4 has the potential to improve the hydrometeor classification.

Chapter 5

REVIEW AND FUTURE WORK

5.1 Review

In this dissertation, the dual-polarization radar measurement was studied following the radar equation and covariance transformation under different polarization basis. The system issues that affect the polarimetric measurement were studied under different precipitation types and scenarios. The modelling developed here is fundamental to polarimetric radar meteorology.

As in all radar applications, the antenna performance is critical in precipitation observation. The polarimetric signatures can be significantly contaminated with spatial distortion induced by antenna patterns, especially due to the sidelobes of the co-polar patterns, when sharp gradients of radar reflectivity exist. A 2-D convolution on the spherical surface was used to simulate the radar observation. Cross-polar coupling makes this convolution model very complicated. To simplify the model, the cross-polar patterns are assumed to be much lower than the co-polar patterns even though they could be as high as the co-polar patterns in a few isolated spots. This assumption would be generally valid and higher-order terms in the cross-polar patterns can be neglected.

Exact reconstruction of the intrinsic polarimetric signatures is possible only through deconvolution, which, however, is infeasible with the scanning scheme of meteorological radar. Instead, we detect the error-prone locations by implementing

the forward convolution where the measured reflectivities are regarded as its intrinsic value. The forward convolution means double convolution. Considering the narrow, Gaussian shaped co-polar beam patterns within the mainlobe, the double convolution seems only to introduce little extra error. However, the error detection does suffer some bias when the differential terms or ratio is utilized, which will decrease the detection rate and at the same time increase false alarm. Based on both simulations and real case analysis, the detection methodology works in a predictable manner. It does provide a facility to help sort out abnormal data. Also note that the gradient alone is not sufficient for such decision. However, it have to be mentioned that these unknown factors, such as double convolution and lack of knowledge of full antenna patterns, limits the usage of this detection methodology to post-processing.

In the mainlobe, excellent cross-polar isolation and pattern matching can be achieved with a well-designed antenna while not guaranteed in sidelobe regions. Plus the sidelobes by themselves could cause substantial errors when large gradients exist across the beam. Therefore, to improve the measurement, it is essential to obtain excellent sidelobe performance. This point was emphasized in the process of antenna upgrade for the CSU-CHILL radar. For accurate cross-polar measurement, it is preferable to offset the peaks of cross-polar patterns from boresight, but is not absolutely necessary in the context of distributed targets as long as the related system limits can be maintained at a reasonable level. It is showed that for the current antenna of CSU-CHILL, 20 dB cross-beam gradient will result in apparent artifacts in the polarimetric signatures where the peak sidelobe level is around -28 dB. With the new antenna, about 10 dB improvement could be expected on both the peak sidelobe level and the integrated sidelobe level. As a result, the cross-beam gradient limit would be doubled. Higher confidence level would be

acquired on the radar measurement with the new antenna which may allow 40 dB cross-beam gradients.

Without consideration of the gradient problem, the simple matrix form of the radar equation, which is defined on two-dimensional complex vector space, precisely describes the system. Also, antenna-induced errors can be calibrated using its integrated error matrix. Particle canting is equivalent to real rotation on the vector space; the propagation without attenuation is equivalent to arbitrary unitary transformation on the vector space; while the antenna errors are equivalent to non-orthogonal basis transformation.

Assuming the scattering medium is governed by independent size, shape and orientation distributions and exhibits "mirror" reflection symmetry, it is easy to separate shape and orientation information from the circular covariance matrix. It is shown that the retrieval can also be accomplished efficiently from the linear covariance matrix. Actually, the direct solution using the linear covariance matrix can solve for the intrinsic shape factors ($\langle|S_{11}|^2\rangle/\langle|S_{22}|^2\rangle$ and $\langle S_{11}S_{22}^*\rangle$) as well as the orientation factors (β_0 and ρ_4). If only unitary basis transformation is involved, it is apparent that the characterization of the underlying scattering process can be easily recovered from the measurements. An optimization approach was developed based on the cross-polar power: the minimal cross-polar power corresponds to zero mean canting angle and zero ellipticity angle. However, because arbitrary phase offsets could be applied to the unitary transformation, which changes its polarization state (χ) with same cross-polar power, ambiguities exist and it is impossible to recover the exact χ of the transformation. This leads to two implications: if $\chi \in \mathbb{C}$, the mean canting angle is not directly related to χ and it is not retrievable with any of the three methods (circular basis, linear H/V basis or optimization). Otherwise, β_0 can be determined from all the three methods. Optimization method gives best retrieval of ρ_4 and β_0.

The propagation matrix could be diagonal or non-diagonal in the linear H/V polarization basis. The effect of diagonal propagation is easily corrected. Since the propagation may introduce phase shifts, it is imperative to correct the propagation effect prior to estimating the orientation factors (of the particles in the scattering volume). Concerning non-diagonal propagation, there is no way to correct its effect basically because the canting over backscattering and canting over propagation cannot be separated. However, if attenuation can be neglected, the incurred transformation is still unitary and thus the optimization approach can be used to obtain accurate estimation of ρ_4. It is very intriguing to estimate β_0 in such a case. The estimation is only possible if the particles are identically distributed. Otherwise, as shown on circular basis, the estimated angle might be either the canting angle on backscattering or the net canting angle along propagation or neither. Again, this reduces the "apparent" advantage of circular basis concerning orientation estimation. In practice, it is reasonable to assume the net mean canting angle as zero for rain which means diagonal propagation. For other hydrometeor types, propagation effect is insignificant, i.e. Φ_{dp} is small, such that the net mean canting angle does not matter too much. For example, reasonable estimates of β_0 can still be obtained for the aligned crystals.

Antenna polarization errors are usually non-orthogonal. A novel estimation algorithm derived in this work is based on the fact that the cross-polar power in the principal plane is still minimal over the whole transformation space. For a well-designed antenna, the polarization errors are small. Statistical fluctuations in measurement might bury such small errors, therefore, a large number of samples are required to properly estimate the antenna polarization errors. The samples used also need to be carefully selected to ensure that the mean canting angle of the precipitation is close to zero. The new developed method relaxes a couple of assumptions used in other approaches, e.g. the particle is not necessarily spherical

and Φ_{dp} need not to be large. Besides, fast algorithm exists for the new method and the estimation can be computed gate-by-gate.

Assuming the precipitation volume can be described independently by its intrinsic shape factors ($\langle|S_{11}|^2\rangle$, $\langle|S_{22}|^2\rangle$ and $\langle S_{11}S_{22}^*\rangle$) and its orientation factors (β_0 and ρ_4), all the polarimetric variables in the linear H/V basis relate to both the shape factors and orientation factors jointly, while those in the circular basis can separate between shape factors and orientation factors. Specifically, Z_h and ρ_{co} can represent the intrinsic shape factors without affecting the interpretation, and Z_{DR} can present credible value for the ratio of $\langle|S_{11}|^2\rangle$ and $\langle|S_{22}|^2\rangle$. LDR is caused by orientation distribution but it also strongly related to the shape factors. Therefore, the estimated ρ_4 is potentially better than LDR in classification application. However, the assumption to obtain ρ_4 is already based on two important assumptions for the scattering medium. If the "mirror" reflection symmetry is not valid, ρ_4 will not be able to provide isolated information on orientation compared to LDR. This could be a limitation of using ρ_4 to improve classification. Circular radar variables CDR and $ORTT/\rho_2$ are independent of orientation factors, but they cannot isolate the mean power $\langle|S_{11}|^2\rangle$ and $\langle|S_{22}|^2\rangle$ from the correlation alone. In addition, according to the analysis over several real cases, the mean canting angle is usually zero, which further diminishes the advantage of CDR over Z_{DR}. Such limitation is discussed for application to hydrometeor classification, but the estimated orientation factors and derived circular radar variables are helpful to better understand the physical properties of meteorological targets.

5.2 Future Work

Since the radar measurements involve convolution of the antenna beam pattern with the scattering medium, an exact inversion involves a deconvolution. Deconvolution is regarded as impossible due to: difficulty in obtaining the full antenna

patterns (amplitude and phase); rapid changes in the medium; or the sparse angular sampling. If phased array antenna is used, flexible scanning scheme and fast angular sampling might be attainable. The system model given in section 2.1 already described the convolution/deconvolution process for the dual-polarization covariance measurement. Inverse algorithm can be developed for incorporating the polarimetric inverse processing into phase array processing.

An independent approach should be sought to examine the properties of orientation and probably also of shape on practical data (e.g., in-situ airborne imaging probes). Then, the estimation performance of the developed algorithms for orientation factors can be checked and validated. Even though simulation is used to validate the algorithm in this work, such validation is not enough when the algorithms are applied to a variety of precipitation types for the purpose of classification. Practical measurements from real cases were analyzed in this work, but that evaluation is based on self-consistency. If airborne data is available for different precipitation types, it is possible to design the classification boundaries and explore the potential improvement by estimated orientation factors and derived circular radar variables.

Bibliography

[1] D. Atlas, C. Ulbrich, and R. Meneghini, "The multiparameter remote measurement of rainfall," *Radio Sci.*, vol. 19, pp. 3–22, 1984.

[2] D. Atlas, "Radar in meteorology." American Meteorological Society, 1990.

[3] V. Bringi and A. Hendry, "Technology of polarization diversity radars for meteorology," in *Radar in Meteorology.* Boston, MA: Amer. Meteor. Soc., 1990, pp. 153–190.

[4] G. McCormick and A. Hendry, "Principles for the radar determinitation of the polarization properties of precipitation," *Radio Sci.*, vol. 10, pp. 421–434, 1975.

[5] T. Seliga and V. Bringi, "Potential use of radar differential reflectivity measurements at orthogonal polarizations for measuring precipitation," *J. Appl. Meteor.*, vol. 15, pp. 69–76, 1976.

[6] A. Hendry, Y. Antar, and G. McCormick, "On the relationship between the degree of preferred orientation in precipitation and dual polarization radar echo characteristics," *Radio Sci.*, vol. 22, pp. 37–50, 1987.

[7] K. Tragl, "Polarimetric radar backscattering from reciprocal random targets," *IEEE Trans. Geosci. Remote Sensing*, vol. 28, no. 5, pp. 856–864, 1990.

[8] G. McCormick, "On the completeness of polarization diversity measurements," *Radio Sci.*, vol. 24, pp. 511–518, 1989.

[9] K. Beard and C. Chuang, "A new model for the equilibrium shape of raindrops," *J. Atmos. Sci.*, vol. 44, pp. 1509–1524, 1987.

[10] S. Nghiem, S. Yueh, R. Kwok, and F. Li, "Symmetry properties in polarimetric remote sensing," *Radio Sci.*, vol. 27, pp. 693–711, 1992.

[11] K. Beard and R. Kubesh, "Laboratory measurements of small raindrop distortion. part 2: Oscillation frequencies and modes," *J. Atmos. Sci.*, vol. 48, pp. 2245–2264, 1991.

[12] K. Beard and A. Jameson, "Raindrop canting," *J. Atmos. Sci.*, vol. 40, pp. 448–454, 1983.

[13] V. Bringi, V. Chandrasekar, J. Hubbert, E. Gorgucci, W. Randeu, and M. Schoenhuber, "Raindrop size distribution in different climatic regimes from disdrometer and dual-polarized radar analysis," *J. Atmos. Sci.*, vol. 60, pp. 354–365, 2003.

[14] A. Ryzhkov, D. Zrnic, V. Bringi, G. Huang, E. Brandes, and J. Vivekanandan, "Characteristics of hydrometeor orientation obtained from radar polarimetric measurements in a linear polarization basis," in *Proc. IGARSS*, Hamburg, Germany, 1999, pp. 702–704.

[15] A. Ryzhkov, "Interpretation of polarimetric radar covariance matrix for meteorological scatterers: theoretical analysis," *J. Atmos. Oceanic Technol.*, vol. 18, pp. 315–328, 2001.

[16] D. Brunkow, V. Bringi, P. Kennedy, S. Rutledge, V. Chandrasekar, E. Mueller, and R. Bowie, "A description of the csu-chill national radar facility," *J. Atmos. Oceanic Technol.*, vol. 17, pp. 1596–1608, 2000.

[17] G. Sinclair, "The transmission and reception of elliptically polarized waves," *Proceedings of the I.R.E*, pp. 148–151, 1950.

[18] V. N. Bringi and V. Chandrasekar, *Polarimetric Doppler Weather Radar: Principles and Applications.* Cambridge, 2001.

[19] G. McCormick, "Polarization errors in a two-channel system," *Radio Sci.*, vol. 16, pp. 67–75, 1981.

[20] R. J. Donaldson, "A demonstration of antenna beam errors in radar reflectivity patterns," *J. Appl. Meteor.*, vol. 3, pp. 611–623, 1964.

[21] R. E. Rinehart and J. D. Tuttle, "Antenna beam patterns and dual-wavelength processing," *J. Appl. Meteor.*, vol. 21, pp. 1865–1880, 1982.

[22] A. Ryzhkov and D. Zrnic, "Beamwidth effects on the differential phase measurements of rain," *J. Atmos. Oceanic Technol.*, vol. 15, pp. 624–634, 1998.

[23] R. J. Donaldson, "Resolution of a radar antenna for distributed targets," *J. Appl. Meteor.*, vol. 4, p. 727739, 1965.

[24] P. Herzegh and R. Carbone, "The influence of antenna illumination function characteristics on differential reflectivity measurements;" in *22nd Conf. on Radar Meteorology.* Zurich: Amer. Meteor. Soc., 1984, pp. 281–286.

[25] Y. Pointin, D. Ramond, and J. Fournet-Fayard, "Radar differential reflectivity zdr: A real-case evaluation of errors induced by antenna characteristics," *J. Atmos. Oceanic Technol.*, vol. 5, no. 3, pp. 416–423, 1988.

[26] A. Mudukutore, V. Chandrasekar, and E. Mueller, "The differential phase pattern of the csu chill radar antenna," *J. Atmos. Oceanic Technol.*, vol. 12, no. 5, pp. 1120–1123, 1995.

[27] J. I. Metcalf and J. S. Ussailis, "Radar system errors in polarization diversity measurements," *J. Atmos. Oceanic Technol.*, vol. 1, pp. 105–114, 1984.

[28] W. Stutzman and M. Terada, "Design of offset-parabolic-reflector antennas for low cross-pol and low sidelobes," *IEEE Antennas Propagat. Mag.*, vol. 35, pp. 46–49, 1993.

[29] D. N. Moisseev, C. M. Unal, H. W. Russchenberg, and L. P. L. hart, "Improved polarimetric calibration for atmospheric radars," *J. Atmos. Oceanic Technol.*, vol. 19, pp. 1968–1977, 2002.

[30] H. Mott, *Antennas for Radar and Communications: A Polarimetric Approach.* New York: Wiley, 1992.

[31] J. I. Metcalf, "A new slant on the distribution and measurement of hydrometeor canting angles," *J. Atmos. Oceanic Technol.*, vol. 5, pp. 571–578, 1988.

[32] G. Huang, J. Hubbert, and V. Bringi, "Precipitation canting angle distribution estimates from covariance matrix analysis of csu-chill radar data," in *30th Conf. on Radar Meteorology.* Munich, Germany: Amer. Meteor. Soc., 2001, pp. 651–653.

[33] W. Boerner, M. El-Arini, C.-Y. Chan, and P. Mastoris, "Polarization dependence in electromagnetic inverse problems," *IEEE Trans. Antennas Propagat.*, vol. 29, pp. 262–271, 1981.

[34] A. Kostinski and W. Boerner, "On foundations of radar polarimetry," *IEEE Trans. Antennas Propagat.*, vol. 34, pp. 1395–1404, 1986.

[35] A. Agrawal and W. Boerner, "Redevelopment of kennaugh's targets characteristic polariation state theory using the polarization transformation ratio formalism for the coherent case," *IEEE Trans. Geosci. Remote Sensing*, vol. 27, pp. 2–14, 1989.

[36] J. Hubbert, "A comparison of radar, optic, and specular null polarization theories," *IEEE Trans. Geosci. Remote Sensing*, vol. 32, pp. 658–671, 1994.

[37] G. McCormick and A. Hendry, "Optimal polarizations for partially polarized backscatter," *IEEE Trans. Antennas Propagat.*, vol. 33, pp. 33–40, 1985.

[38] K. Tragl, E. Lueneburg, A. Schroth, and V. Ziegler, "A polarimetric covariance matrix concept for random radar targets," in *Intl. Conf. Antenna and Propagation.* York, U.K.: IEE, 1991, pp. 396–399.

[39] T. Oguchi, "Electromagnetic wave propagation and scattering in rain and other hydrometeors," *IEEE Proc.*, vol. 71, pp. 1029–1078, 1983.

[40] J. Hubbert and V. Bringi, "An iterative filtering technique for the analysis of copolar differential phase and dual-frequency radar measurements," *J. Atmos. Oceanic Technol.*, vol. 12, pp. 643–648, 1995.

[41] V. Bringi, T. Keenan, and V. Chandrasekar, "Correcting c-band radar reflectivity and differential reflectivity data for rain attenuation: A self -consistent method with constraints," *IEEE Trans. Geosci. Remote Sensing*, vol. 39, pp. 1906–1915, 2001.

[42] A. Jameson, "The effect of temperature on attenuation correction schemes in rain using polarization propagation differential phase shift," *J. Appl. Meteor.*, vol. 31, pp. 1106–1118, 1992.

[43] V. Chandrasekar, J. Hubbert, and V. Bringi, "Transformation of dual-polarized radar measurements to arbitary polarization bases," *J. Atmos. Oceanic Technol.*, vol. 10, pp. 937–949, 1994.

[44] A. Jameson and J. Dave, "An interpretation of circular polarization measurements affected by propagation differential phase shift," *J. Atmos. Oceanic Technol.*, vol. 5, pp. 405–415, 1988.

[45] A. Ryzhkov, D. Zrnic, S. Dusan, J. Hubbert, V. Bringi, J. Vivekanandan, and E. Brandes, "Polarimetric radar observations and interpretation of co-cross-polar correlation coefficients," *J. Atmos. Oceanic Technol.*, vol. 19, pp. 340–354, 2002.

[46] J. Hubbert, V. Bringi, and D. Brunkow, "Studies of the polarimetric covariance matrix. part i: Calibration methodology," *J. Atmos. Oceanic Technol.*, vol. 20, no. 5, pp. 666–706, 2003.

[47] V. Santalla and Y. Antar, "A comparison between different polarimetric measurement schemes," *IEEE Trans. Geosci. Remote Sensing*, vol. 40, no. 5, pp. 1007–1017, 2002.

[48] L. Liu, V. Bringi, and V. Chandrasekar, "Analysis of the copolar correlation coefficient between horizontal and vertical polarizations," *J. Atmos. Oceanic Technol.*, vol. 11, pp. 950–963, 1994.

[49] K. V. Mardia and P. E. Jupp, *Directional statistics.* New York: Wiley, 2000.

[50] J. Hubbert and V. Bringi, "Studies of the polarimetric covariance matrix. part ii: Modeling and polarization errors," *J. Atmos. Oceanic Technol.*, vol. 20, no. 7, pp. 1011–1022, 2003.

[51] A. Jameson and E. Mueller, "Estimation of propagation-differential phase shift from sequential orthogonal linear polarization radar measurements," *J. Atmos. Oceanic Technol.*, vol. 2, pp. 133–137, 1985.

[52] E. Gorgucci, G. Scarchilli, and V. Chandrasekar, "A robust estimator of rainfall rate using differential reflectivity," *J. Atmos. Oceanic Technol.*, vol. 11, pp. 586–592, 1994.

[53] R. Doviak, V. Bringi, A. Ryzhkov, A. Zahrai, and D. Zrnic, "Considerations for polarimetric upgrades to operational wsr-88d radars," vol. 17, pp. 257–278, 2000.